

NORTHWESTERN UNIVERSITY

Microstructure Characterization for Analysis and Design of Microstructural Material System

A DISSERTATION

SUBMITTED TO THE GRADUATE SCHOOL  
IN PARTIAL FULFILLMENT OF THE REQUIREMENTS

for the degree

DOCTOR OF PHILOSOPHY

Mechanical Engineering

By

Umar Farooq Ghumman

EVANSTON, ILLINOIS

December 2022

© Copyright by (Umar Farooq Ghumman) 2018

All Rights Reserved

## **ABSTRACT**

Microstructure Characterization for Analysis and Design of Microstructural Material System

Umar Farooq Ghumman

Computational material engineering (CME) has increased the pace of material development many folds in recent years by taking advantage of computational tools such as using simulations as replacement to experiments, and building complicated processing-structure-property relationships using advanced machine learning tools. The importance of CME is underscored by new computation-based design frameworks such as material sensitive design and integrated computational material engineering. In these material design frameworks, the goal is to optimize a specific property, and since a material's microstructure heavily affects its properties, there is an immense gain to study and analyze the microstructure accurately and efficiently. This leads to microstructure characterization which involves the reduction of the high-dimensional structural information of a material to a reduced form which effectively captures the most salient and relevant features of the structure at the appropriate length scale. To this end, the central theme of this dissertation is to supplant the current microstructure characterization techniques for the analysis and design of microstructural material systems. The overall contributions of this work are

achieved in three major research tasks carried out on three different material systems and are briefly discussed below.

Spectral Density Function (SDF) is a Fourier transform-based tool that can sufficiently characterize certain quasi-random microstructure material systems by decomposing the dominant microstructural features in the physical frequency space. SDF has also been used in the design of heterogeneous materials. Until recently, the use of SDF for characterization was limited to isotropic microstructures. Even after its successful utilization, there are still some gaps in understanding the shape of SDF. My first task revolves on deconvolving the complexities of SDF function by finding its relationship with physical descriptors. This work also extends the use of SDF for reconstruction of three-phase material systems. By utilizing the knowledge of SDF gained, this thesis presents an SDF-based framework for the design of quasi-random material systems which centers upon design representation using SDF parameters. The framework is further modified to deal with special case scenarios where low fidelity and high fidelity simulations can be utilized to efficiently find the optimal processing conditions of a quasi-random material system. This multi-fidelity optimization scheme is only enabled by SDF frequency enhancement tool developed in this thesis.

Quite different from the quasi-random microstructure, another interesting microstructural material system is that of granular materials. It consists of grains of different sizes, orientation, and phase angles. It encapsulates a much higher dimension information than quasi-random material systems previously mentioned, and thus cannot be characterized by SDF or similar techniques. Furthermore, these granular microstructures come with their own challenges such as differentiating between two microstructures quantitatively in model validation. This is a critical challenge in calibration of additive manufacturing simulations of alloys where the microstructure

difference between ground truth and simulations needs to be quantified. To address this challenge, we present a novel difference metric to quantitatively differentiate between granular microstructures based on the combination of chord length distribution and earth mover's distance. Building on this metric, this thesis extends its use to solve the main research problem of accurately calibrating simulations with respect to experiments. This is done by developing a framework which relies on the novel dissimilarity metric along with Bayesian optimization to calibrate simulation parameters efficiently and accurately for additive manufacturing simulations.

Some microstructures do not fall in any general category and can be classified as complex microstructures. For such microstructures, it is almost impossible to numerically characterize them using the traditional tools. One possibility is that of using advanced machine learning tools such as neural networks. But the cost of such tools is that they require a huge amount of data. The more complex the microstructure, the more data it would require. Unfortunately, a big constraint of material design is that the scientists have generally very limited data to work with. An alternative to training such expensive models is to use an already trained model. This is known as Transfer Learning (TL). TL involves using pretrained model for a completely different purpose than for which they were trained, thus they need to be modified for their successful implementation. The last research task explores the possibility of modifying and using transfer learning from a pre-trained VGG-19 deep neural network model to characterize the microstructure and build process-structure-property relationships for complex microstructures.

## ACKNOWLEDGMENTS

I would like to express my sincere gratitude to my advisor, Professor Wei Chen. She has always provided me with guidance, support and inspiration in my academic research as well as in my personal life throughout the tenure of my Ph.D. at Northwestern University. Dr. Chen gave me many diverse opportunities to explore my research potential. I must admit, I am truly in awe of her time and resource management skills for she is truly a role model to follow in academia. In addition, I sincerely thank my committee members Professor Gregory Wagner and Professor Daniel Appley. For my research, Dr. Wagner provided critical and detailed feedback in the work pertaining to additive manufacturing. Whereas with his exceptional experience, Dr. Appley helped me draw insights for the silicone rubber dataset. Both their contributions have helped improve the quality of my research immensely as well as my approach to it.

Furthermore, throughout my PhD journey, I have been very fortunate to work with the amazingly talented and diverse set of people from Integrated Design Automation Lab (IDEAL). Special thanks to Dr. Anton Van Beek and Dr. Akshay Iyer for helping me improve my writing skills. Dr. Yichi Zhang, Dr. Ramin Bostanabad, Dr. Tianyu Huang, and Dr. Xiaolin Li were extremely supportive during my formative years. Henry Zhang and Yigitcan Comlek were always there to double-check my work or to provide their perspective on material science projects. I would also like to thank my colleagues-cum-friends from IDEAL, including Yaxin Cui, Dr. Yu-Chin Chan, Dr. Wei Chen (Wayne) and Dr. Daicong Da.

I would like to express my special thanks to the other NU members who provided me with sincere guidance and support throughout my PhD including Dr. Hammad Faizi, Abu Bakar, and Dr. Saad Ahmed. I would also like to express my gratitude for the friends in Chicago who went

out of their way to help me and my family in our ups and downs. Among them Mr. Wajid Siddiqui and Abdul Sami Khan have become my role models and have instilled in me a sense of selflessness to help anyone in need. I would also like to especially mention their families for taking care of my family and I. They made our stay in Chicago very special by being our home away from home.

Next, I would like to thank my family; my parents, Khalid Rifat Rasul Ghumman and Fouzia Khalid, for their prayers and for providing me the best possible environment to become a scholar, my elder sister, Maria Komil Ghumman, for her selfless love and prayers, and my brother, Hamza Khalid Ghumman, without whom I would never have even gotten accepted at Northwestern University. From the application process, the admission all the way until this final thesis, Hamza has always been there for me to provide critical feedback and counseling to keep me on track.

Lastly, I would like to thank my amazing and supportive wife, Momal Khalid, who sacrificed all her ambitions for my career. She brought two beautiful daughters, Ayesha and Maryam, into our life and she solely took care of them and nurtured them like no other so that I could focus on my studies. Her emotional support, love and understanding throughout these challenging years made it possible for me to complete my PhD. For me, Momal, Ayesha and Maryam are the primary source of motivation for my work. Lastly, I hope that my research can be of little help in shaping a better world for our daughters' future.

*To my parents, to whom I am eternally indebted,  
& to my ever-supportive wife.*

## Contents

Chapter 1 Introduction and Research Objective .....	17
1.1 Introduction.....	17
1.2 Research Objectives and Tasks.....	21
1.3 Dissertation Organization .....	25
Chapter 2 Technical Background .....	27
2.1 Microstructure characterization and reconstruction.....	27
2.2 Transfer Learning.....	33
2.3 Bayesian Optimization.....	35
2.4 Summary .....	40
Chapter 3 SDF-based Analysis for Polymer Material System.....	41
3.1 Introduction.....	41
3.2 Understanding SDF.....	42
3.2.1 Introduction to SDF .....	43
3.2.2 Studying the relationship between descriptors and SDF.....	45
3.3 SDF based design framework .....	55
3.4 SDF frequency resolution enhancement .....	58
3.5 Multi-fidelity optimization for OPVC .....	61
3.5.1 CGMD Simulations.....	66
3.5.2.4 Validation of results .....	74
3.5.3 Optimization-study conclusion .....	76
3.6 Summary.....	77
Chapter 4 Characterization and Design of Granular Microstructures in Additive Manufacturing Systems .....	79
4.1 Introduction.....	79
4.2 Granular Microstructure Characterization and Dissimilarity Score.....	80
4.3 Building P-S-P modeling using Machine Learning .....	90
4.3.1 Creating the dataset.....	91
4.3.2 Parameterizing the temperature history .....	93
4.3.3 Principal Component Analysis.....	95
4.3.4 Process-Structure relationship.....	96
4.4 Application in Cellular Automaton (CA) model Calibration.....	100

	10
4.4.1 CA simulations.....	103
4.4.2 Model Calibration Framework.....	106
4.4.3 Results and discussion .....	108
4.5 Summary.....	117
Chapter 5 Transfer Learning for Complex Multi-Scale Microstructures with Limited Data .....	119
5.1 Introduction.....	119
5.2 Methods.....	125
5.2.1 Experiment Setup.....	125
5.2.2 Post processing of images .....	127
5.2.3 Transfer Learning methodology.....	129
5.3 Result and Analysis.....	135
5.3.1 Artificial Dataset.....	135
5.3.2 Experiment Dataset – Silicone Rubber .....	139
5.3.2.1 Experimental Data Interpretation.....	139
5.3.2.2 Structure-Property Correlation Analysis.....	141
5.3.2.3 Predictive Model.....	143
5.4 Summary.....	145
Chapter 6 Conclusions and Future Work .....	147
Appendix .....	152
A.1 Nanomine Repository .....	152
A.2 Three-phase characterization and reconstruction.....	156
References .....	162

## List of Figures

<i>Figure 1-1: Layout of the three major objectives. Left side focuses on contiguous microstructures by leveraging insights obtained from in-depth SDF study and using those for PSP design. Middle column centers on granular microstructures which are characterized by CLD, and then the use of CLD is extended to facilitate design. Right side concentrates on extracting multi-scale information from complex microstructures using a combination of SDF and Transfer Learning to facilitate Structure-Property mapping.....</i>	<i>25</i>
<i>Figure 2-1: An artificial material system consisting of two distinct phases. The dotted line represents two points separated by a fixed distance in the microstructure. Two-point correlation function determines the probability of finding both the points belonging to the same phase. ....</i>	<i>30</i>
<i>Figure 2-2: Sample microstructure which are suitable for characterization using physical descriptors. (A) is matrix-filler system. (B) is a granular microstructure. The red-dotted line intersects the grain-boundaries to locate the intersections.....</i>	<i>31</i>
<i>Figure 2-3: Single neuron Neural Network.....</i>	<i>33</i>
<i>Figure 2-4: Examples of VGG 19 model customizations. The names of the layers are written inside the sub-blocks. (A) the weights of the first 16 layers are frozen, while the last three layers are trainable. (B) The first layers are used as in (A) but the last three layers are replaced with custom two layers. ....</i>	<i>35</i>
<i>Figure 2-5: Surrogate model for an unknown function (<math>f(x)</math>). Red dots represent initial samples. The grey shaded region represents uncertainty (95% Confidence Interval). The green dotted line represents the maximum of surrogate function, whereas the red solid line represents the point with maximum uncertainty. ....</i>	<i>38</i>
<i>Figure 3-1: SDF of a quasi-random microstructure from Yu et al. [12]. Blue is the original curve and red is approximation.....</i>	<i>43</i>
<i>Figure 3-2: SDF of an OPVC material from Ghumman et al. [14]. Blue is the original curve and red is the approximation.....</i>	<i>43</i>
<i>Figure 3-3: Two sample microstructures (a &amp; b) along with their Fourier spectrum in the insets; (c &amp; d) are the final 1-D SDFs of each image. Red dashed line represents the approximated SDF.....</i>	<i>45</i>
<i>Figure 3-4: a-c are images with circles of radius 4 are spread out at distances of approximately 20, 40 and 60 respectively. d-f are their respective Fourier transforms. ....</i>	<i>47</i>
<i>Figure 3-5: SDF plotted for the three cases showed in Figure 3-4. Note that x-axis are arbitrary units. ....</i>	<i>47</i>
<i>Figure 3-6: a-c are images with circles of radius 4, 8 and 12 respectively. d-f are their respective Fourier transforms.....</i>	<i>48</i>
<i>Figure 3-7: SDF plotted for the three cases showed in Figure 3-6. ....</i>	<i>48</i>

<i>Figure 3-8: a-c are images with circles of radius 4, and window sizes of 200, 400, and 600 respectively. d-f are their respective Fourier transforms. ....</i>	<i>50</i>
<i>Figure 3-9: SDF plotted for the three cases showed in Figure 3-8. ....</i>	<i>50</i>
<i>Figure 3-10: a-c are images with circles of radius 4, and numbers of circles as 570, 800 and 1100 respectively. d-f are their respective Fourier transforms. ....</i>	<i>51</i>
<i>Figure 3-11: SDF plotted for the three cases showed in Figure 3-10. ....</i>	<i>52</i>
<i>Figure 3-12: a-c are images with 200 intrusions in the shape of circles, squares, diamonds, and octagons respectively. d-f are their respective Fourier transforms. ....</i>	<i>53</i>
<i>Figure 3-13: SDF plotted for the three cases showed in Figure 3-12. ....</i>	<i>54</i>
<i>Figure 3-14: (a) and (b) are images created with nearest neighbor distance of 20. (c) and (d) are images created with nearest neighbor of 25. The number of dots/clusters is fixed to 40. (e) represents the SDF of the (a-d) images. ....</i>	<i>55</i>
<i>Figure 3-15: SDF-based design framework to find optimal processing conditions of any quasi-random material. ....</i>	<i>56</i>
<i>Figure 3-16: Comparison of the SDF at different length scales of the same material. The SDF of the full microstructure (Figure 2A) is represented by the blue function (Figure 2B), and the SDF for the red inlay (Figure 2A) is represented by the red function (Figure 2B). ....</i>	<i>58</i>
<i>Figure 3-17: SDF frequency resolution enhancement. (A) Duplicating values in each bin of SDF to increase the number of frequency bins by two. (B) Comparing the SDF of the original full image of microstructure with the enhanced SDF of the cropped image of microstructure. Note that x-axis here is only the index of frequency bin and not the frequency itself. ....</i>	<i>59</i>
<i>Figure 3-18: Top: Starting from a small 20 x 20 x 20 nm CGMD simulated microstructure, a large 80 x 80 x 80 nm is reconstructed using SDF frequency resolution enhancement. From the large reconstruction a smaller 20 x 20 x 20 nm sample is cropped for comparison. Bottom: SDF comparison of the original microstructure with cropped microstructure. ....</i>	<i>61</i>
<i>Figure 3-19: Three-step multi-fidelity optimization framework. The initialization of the optimization problem is to use the low-fidelity model to infer the range of intermediate structure parameters. Subsequently, in the next step, we find the optimal performance by maximizing the IPCE with respect to the volume fraction <math>VF^*</math> and the intermediate modeling parameters <math>P, D</math>. Finally, the optimal annealing temperature <math>T^*</math> is found by maximizing the entire PSP link using the high-fidelity model. ....</i>	<i>62</i>
<i>Figure 3-20: Parametrization of the SDF of low-fidelity CGMD microstructures. The SDF of the nine microstructures obtained from low fidelity CGMD simulations (Figure 8A) shows a remarkable consistency among the microstructures. Subsequently, this similarity can be captured through a parametric function that can be used to approximate the original SDFs (Figure 8B). ....</i>	<i>70</i>
<i>Figure 3-21: Gaussian process model prediction for the IPCE as a function of temperature. The high-fidelity CGMD simulations used the optimal volume fraction <math>VF^* = 0.40</math> as identified in Step 1 of the introduced design framework. ....</i>	<i>73</i>

<i>Figure 4-1: The microstructure on top (a) is simulated using CA model. The bottom four curves (b-e) are the CLDs at the four representative angles. The x-axis is the length of chord and y-axis is the probability.....</i>	<i>82</i>
<i>Figure 4-2: Quantifying difference between two set of distributions using EMD and MD. (A) Difference between distribution x and y. (B) Difference between distribution x and z. ....</i>	<i>84</i>
<i>Figure 4-3: The microstructure on top (A) is simulated using CA model. The bottom four curves (B-E) are the CLDs at the four representative angles. The x-axis is the length of chord and y-axis is the probability.....</i>	<i>87</i>
<i>Figure 4-4: Artificial microstructure generated by Dream 3D. (A): Pair of statistically similar microstructures created from same set of input parameters. (B): Pair of statistically different microstructures created from two different sets of input parameters. ....</i>	<i>89</i>
<i>Figure 4-5: Multiple slices of two cases that were simulated using the CA code. Instead of the 3D volume, slices are shown to represent how the ARCLD is computed i.e. plane by plane.....</i>	<i>90</i>
<i>Figure 4-6: Framework for P-S-P modeling of AM .....</i>	<i>90</i>
<i>Figure 4-7: Sampling scheme for RVEs. In each layer 12 samples are taken with 4 varying x-axis locations and 3 varying y-axis locations. ....</i>	<i>92</i>
<i>Figure 4-8: Visual explanation of the thermal history parameters. ....</i>	<i>93</i>
<i>Figure 4-9: Highest and lowest temperature scatter plot of all the data points. The x-axis sample number represents sample number of each case/wall. ....</i>	<i>94</i>
<i>Figure 4-10: Scatter plot for number of peaks observed in temperature history. Nine clear clusters along y-axis are observed which are related with the layer number.....</i>	<i>95</i>
<i>Figure 4-11: Scatter plot for number of mean heat gap observed in temperature history. Two distinct levels are observed corresponding to the two different scan speeds.....</i>	<i>95</i>
<i>Figure 4-12: Process-Structure mapping using neural networks.....</i>	<i>97</i>
<i>Figure 4-13: Process-Structure mapping using neural networks with larger RVEs. (A) using 23 PCAs. (B) using 56 CLD parameters. ....</i>	<i>98</i>
<i>Figure 4-14: Structure-Property mapping using neural networks. (A) Yield Strength prediction. (B) Young's Modulus prediction.....</i>	<i>98</i>
<i>Figure 4-15: Process-Property mapping using neural networks. (A) Yield Strength. (B) Young's Modulus. ....</i>	<i>99</i>
<i>Figure 4-16: Young's Modulus of the dataset against sample number.....</i>	<i>99</i>
<i>Figure 4-17: Framework for model calibration of Additive Manufacturing microstructure simulation using Dissimilarity Score. ....</i>	<i>107</i>
<i>Figure 4-18: Initial design space of parameters for substrate grains calibrations. ....</i>	<i>110</i>

<i>Figure 4-19: Four initial simulation vs experimental substrate microstructures. (A) Select cross-sections of simulated substrate microstructures; (B) Experimental substrate microstructures for Case A, B, and C.</i>	111
<i>Figure 4-20: History of Dissimilarity Score computed for CA parameters calibration.</i>	112
<i>Figure 4-21: Calibration space of Bayesian optimization process. The surface plot represents the GP model of DS, and the blue spheres represents the samples.</i>	112
<i>Figure 4-22: Initial design space of parameters for laser scan microstructure calibrations.</i>	114
<i>Figure 4-23: Maximum Expected Improvement Score for each iteration of Bayesian Optimization.</i>	115
<i>Figure 4-24: Dissimilarity Score of each iteration for calibration of the entire laser scan microstructure.</i>	115
<i>Figure 4-25: Calibrated microstructure for case B and C compared with experimental images.</i>	116
<i>Figure 4-26: Calibrated microstructure for case A compared with experimental images as the testing case.</i>	117
<i>Figure 5-1: Extracting multi-scale features of a fractured surface of filled silicone rubber. A: Grey scale height image of a silica rubber sample. The red line is a line scan that provides 1D height information(C). B: Meso-scale features which capture the step-like patterns. C: Local roughness computed by scanning the red line over the original image in (A).</i>	123
<i>Figure 5-2: The experimental setup. (A) Model I fatigue test in pure shear geometry. The middle white area is the test area. An initial pre-crack 'a' was introduced before the fatigue test. (B) Schematic of the fatigue crack surface observation process using a 3D microscope.</i>	127
<i>Figure 5-3: Sample sets of one intensity image and one height image from a 3D scan.</i>	127
<i>Figure 5-4: Visualization of post-processing steps for height images.</i>	129
<i>Figure 5-5: Examples of VGG 19 model customizations. The names of the layers are written inside the sub-blocks. (A) the weights of the first 16 layers are frozen, while the last three layers are trainable. (B) The first layers are used as in (A), but the last three layers are replaced with custom two layers.</i>	131
<i>Figure 5-6: Features extracted from different layers in a pre-trained VGG 19 model with a sample input.</i>	133
<i>Figure 5-7: Framework for extracting microstructure features using pruned Transfer Learning models.</i>	135
<i>Figure 5-8: Shape of SDF used to reconstruct artificial microstructures.</i>	136
<i>Figure 5-9: Unique artificial microstructures created from different SDFs which are controlled by two tuning parameters <math>W</math> and <math>P</math>.</i>	137
<i>Figure 6-1: (a) is the original image. (b) is the reconstructed image. (c, d, and e) are the two-point correlation functions <math>P_{23}</math>, <math>P_{13}</math>, and <math>P_{12}</math> respectively.</i>	160



## List of Tables

<i>Table 1-1: Some common physical descriptors along with their type. ....</i>	32
<i>Table 3-1: Computational cost for individual CGMD simulations using low and high-fidelity approaches. ....</i>	63
<i>Table 3-2: Design of experiments used to explore the potential microstructures using the low-fidelity CGMD simulation model.....</i>	71
<i>Table 4-1: DS calculated between similar microstructures (Case 3 and Case 4) and different microstructures (Case 1 and Case 2). ....</i>	89
<i>Table 4-2: Experimental details of the four builds. ....</i>	92
<i>Table 4-3: Initial calibration parameters and dissimilarity scores for substrate grains calibration. ....</i>	110
<i>Table 4-4: Initial calibration parameters and dissimilarity scores for laser scan microstructure calibration. ....</i>	114
<i>Table 5-1: Test R-squared results for different pruning locations. The results are color coded with green being good and red being worse. ....</i>	138
<i>Table 5-2: Test r-squared values of predictive models with varying total number of images. The results are color coded with green being good and red being worse. ....</i>	139
<i>Table 5-3: Model accuracy results using the Transfer Learning framework with Height Image, SDF, and both combined as inputs. The results are color coded with green being good and red being worse. Some results are omitted because the results were too bad and skewed the color scheme. ....</i>	142
<i>Table 5-4: Model Accuracy results for the different predictive models having different inputs. ....</i>	144

# Chapter 1 Introduction and Research Objective

## 1.1 Introduction

Material development is becoming a considerably faster process with the introduction of ever more sophisticated design techniques. A driver behind these developments is the Materials Genome Initiative [1] which has switched the focus of scientists from physical experiments to the use of computational tools to expedite the design process. The rationale here is that scientists can supplant time consuming experimental synthesis, characterization, and validation processes with simulations to accelerate the development of new knowledge [2]. Another reason is that progress in theory occurs at a much faster pace than experimental synthesis, characterization, and validation, as mentioned in Pablo et.al. [2] Thus, shifting the focus away from experiments towards computation can increase the speed of material development by many folds. One example where computational tools have played a substantial role in the design of new material systems is the coupling of processing conditions of a material to its property or performance [3]. Despite this being an intuitively straightforward link, its implementation is often marred by a lack of data or computational resources.

A potent workaround to the data limitation is the consideration of a material's structure and its implementation as an intermediate link between the processes and performance [4,5]. The motivation behind this is that a material's structure greatly affects its properties [6–8], and thus provides insights into its underlying physics [9]. These three links combined are generally referred to as the process-structure-property (PSP) link. The PSP link has provided the material science community with a powerful insight that enables the *inverse design* of new materials with superior

performance. The microstructure sensitive design (MSD) [8] framework is an example of an inverse design framework which gives central role to microstructure. The microstructure of a given material consists of all the physical features that are observable at very small length scales, from micrometers to nanometers. If we want to grasp all the minute details of a microstructure, it can be inhibitive to even store such large information, let alone use it for design. Therefore, there exists a need to dissect the microstructure information and extract the representative and relevant information only. This process is referred to as material characterization [8,10]. Apart from characterization, digital reconstruction of a microstructure is also important to simulate material properties and extract other features which will help create the process-structure-property links. Microstructure reconstruction is a very material-specific procedure, i.e., there are different methodologies for different materials types [11]. Characterization and reconstruction are jointly referred to as microstructure characterization and reconstruction (MCR).

MCR techniques can be broadly divided into four categories as mentioned in Bostanabad et. al.[10]: Statistical methods, descriptors, machine learning, Fourier spectrum (spectral density function) .From the many MCR techniques available, selecting the one which is relevant to the corresponding target properties is a key part of material sensitive design [8]. Taking the example of Organic Photovoltaic Cells (OPVCs), it has been shown that the Spectral Density Function (SDF) representation of microstructure has a direct association with OPVCs' ability of light trapping [12]. That is why the SDF has been successfully used to represent photovoltaics in past studies [13–15]. An example of a different microstructural system is that alloy parts manufactured through metal additive manufacturing (AM). For alloys, grain size and orientation are the key microstructural features which directly impact mechanical and physical properties [6,7]. Thus, a

different MCR technique is required to extract these details. Chord Length Distribution [16] is one such technique which has proven efficient to represent the grain structures of alloys in literature. Furthermore, in some cases, the microstructure can be too complex to be characterized by any single feature, e.g., in the case of rough rubber surfaces. In such cases, we can use a combination of two different MCR techniques e.g. Machine Learning and Fourier spectrum.

One major focus of this dissertation is to gain a better physical interpretation of the SDF. The Fourier transform (FT) is the core part of SDF and has been used in many diverse fields including spectroscopy [17], numerical methods [18], and image processing [19] etc. In essence, FT decomposes a waveform into a sum of sinusoids of different frequencies [20]. For MCR, such decomposition would represent the dominant microstructural features in the physical frequency space. Literature suggests that SDF can sufficiently characterize some complex microstructures [21]. SDF has also been used to represent quasi-random microstructures manufactured by bottom-up processes [22,23]. The use of SDF is not limited to representation only, in fact it has also been used in design to bridge the gap between process-structure [13] and structure-property [14] links. Traditionally, SDF has been used for isotropic materials but recently Iyer et.al [15] have extended its use to incorporate anisotropic materials as well. However, the most attractive feature of SDF for design of materials is its parametric functions that can be represented by only a few parameters [12,14].

The experimental equivalent of SDF is the small angle x-ray scattering (SAXS). SAXS has been analyzed in literature to reveal different aspects of the underlying microstructure. For example, it has been used to identify the type of crystal and its preferred orientation [24]. In OPVCs, the slope of SAXS has also been used to identify the relative length scales of the donor

clusters and acceptor crystallites [25]. But such analysis has not been used to interpret the digital twin of SAXS i.e. SDF. Thus, there exists a gap in understanding the interpretation of the SDF curve. A methodological approach to study and link the SDF curve features with underlying microstructural physical features (descriptors) will open new doors for the use of SDF. Another gap in SDF is its limitation to characterize only 2-phase material systems. However, the possibility of extending the SDF approach to facilitate design of multi-phase material system can be explored.

While SDF works effectively for particle-based systems, it is not suitable for complex grain structures formed through AM. For AM, a few established characterization descriptors include average grain size [26,27], equivalent spherical diameter [28], and grain orientation [29]. Another relatively new promising characterization for alloys is called Chord Length Distribution (CLD) [16]. To encapsulate the orientation information, a slightly modified version is used which is called angularly resolved chord length distribution [30]. Though CLD covers rich granular information of AM microstructures, it significantly increases the dimensionality of the characterization, hence inhibiting its use in a design process. To bridge the P-S-P gap for design of parts manufactured by AM, it is imperative that a low dimensional microstructure representation is developed.

Microstructure characterization is not the only obstacle in bridging the P-S-P chain for AM. Other factors include the stochastic nature of the AM microstructure, high gradient of temperature profiles [31], non-stationarity/location dependence, and expensive simulations. Separately, there are established software that have linked process to structure (P-S) [32–34] and structure to property (S-P) [35]. One set-back of such an approach is that they are computationally intensive and limited in length and time scales [34,36,37]. Another gap in this field is that there is either a complete lack of validation with real materials, or only a qualitative validation. For example, the

validation of simulated microstructures from P-S models with actual image is done visually by human eyes [38]. Thus, a validated and efficient P-S-P modeling capability that can predict the key properties for a given material and process can unravel new AM capabilities. *This research will investigate the use of CLD for solving some of the challenges associated with metal AM mentioned earlier.*

Some material systems, however, are not sufficiently characterized by a single MCR method and they require a combination of methods. For example, to characterize the fractured surface topology of filled silicone rubber, it is hard to put a finger on one MCR technique. The reason is that there are features of interest at different scales: (A) step-like patterns which can be observed visually, and (B) change in local roughness in proximity. A possible solution perhaps is to use a combination of MCR methods. Since the structure in (A) is not too simple to be fully characterized by using either SDF, descriptors, or statistical methods, the only option left is Machine Learning (ML). However, one constraint with traditional ML like Neural Networks is that it requires a big volume of datapoints. Unfortunately, in material design we rarely have a big dataset. To overcome this constraint of ML, Transfer Learning can be used for a limited dataset [39]. For (B), we can use a 2D version of SDF to capture the frequency of change in local roughness in proximity. *This dissertation will explore the possibility of combining two different MCR techniques in a combination to overcome the challenge of microstructure complexity and limited data.*

## 1.2 Research Objectives and Tasks

The overarching goal of this dissertation is to develop microstructure analysis techniques that facilitate the creation of P-S-P relations as well as the design of complex microstructural

material systems. This overarching goal is divided into three specific objectives: (1) to expand the understanding of SDF-based characterization, and then employ it on OPVC material system, (2) explore the use of CLD for characterization of AM parts and to create a reduced order P-S-P model for a representative AM material system, and (3) explore the possibility of combining transfer learning with SDF to build S-P model for complex microstructures with limited data. Figure 1-2 shows the layout of the two specific objectives. Left side represents (1), middle represents (2), and right represents (3). To achieve these, following tasks are planned:

1) SDF based analysis for polymer materials systems (OPVC) – Chapter 3

a) New understanding of SDF

Though SDF has been successfully used for microstructural design, its features still need to be further understood to extract its maximum benefit and to determine its limitations. Thus, as a first step, the relationship of SDF and physical descriptors are explored in this study. Next, we aim to study SDF parameterization to enable even more lower dimensional representation, and efficient design exploration.

b) SDF frequency resolution enhancement

Statistical microstructure characterization offers a unique opportunity to extract microstructural information from a much smaller sample, and yet be able to recreate a larger microstructural sample. But the traditional statistical tools are time consuming, so in this study, we explore the opportunity to use SDF for efficient reproduction of larger samples from smaller samples by enhancing the frequency resolution of SDF.

c) P-S-P for OPVC design

Lastly, the use of SDF is extended to design an optimal microstructure of OPVC. For which the main advantage leveraged is the ease of SDF parameterization in setting-up a design space coupled with fast microstructure reconstructions using SDF. The original design problem is divided into three steps to save computational time. In the initial step, lower fidelity simulations are used to approximate the optimal volume fraction, whereas in the final step high fidelity simulations are used to find the optimal temperature.

## 2) Characterization and Design of granular microstructures in AM systems – Chapter 4

### a) CLD and Dissimilarity Score (DS)

To characterize the granular microstructure, a variant of CLD is developed which is not only cheaper to calculate but also considerably lower in dimension. CLD application is further extended with the help of Earth Mover's Distance to, for the first time, quantitatively differentiate the granular microstructures by giving out a single number. This metric has been named Dissimilarity Score (DS).

### b) Process-Structure model calibration

CA is basically a process-structure simulation model. The calibration process of CA simulation is based on trial and error. We employ DS to facilitate this process. This is achieved by minimizing the DS score between experimental images with the simulated ones. To minimize the expensive CA runs, Bayesian Optimization will be employed.

### c) P-S-P mapping using Machine Learning (ML)

Finally, machine learning will be used to bridge the Process-Structure-Property (P-S-P) link which can replace the high-fidelity expensive P-S and S-P models. Depending on the

data, dimension reduction will be employed to reduce the number of mapping parameters of process and property. To overcome the large data requirement, the build part will be divided into smaller representative volume elements (RVEs).

3) Transfer Learning and SDF combinations for complex multi-scale microstructure with limited data – Chapter 5

a) Pruning a pre-trained model

To characterize the meso-scale features we explore the possibility of using Transfer Learning (TL) because TL provides the benefits of deep neural networks without the associated big data requirement. To further maximize the benefits of TL, we prune a pre-trained model at various locations to find the best possible final architecture.

b) Kernel selection for 2-D SDFs

Since the dataset is limited, adding more equal features may be detrimental to the over-all accuracy of the model. In that case, we look towards using only a subset of the output space. We do this by trying to find the kernels that explain the property best and that are not correlated with the meso-scale feature map.

c) Apply pruning and kernel selection on artificial and real data

To understand how the volume of data effects the above techniques, we build an artificial dataset consisting of microstructure images and corresponding physical property. The effect of selectively decreasing the dataset is studied. After a framework is in place, we apply the same methodology on fracture surface of filled silicone rubber to build an S-P model.

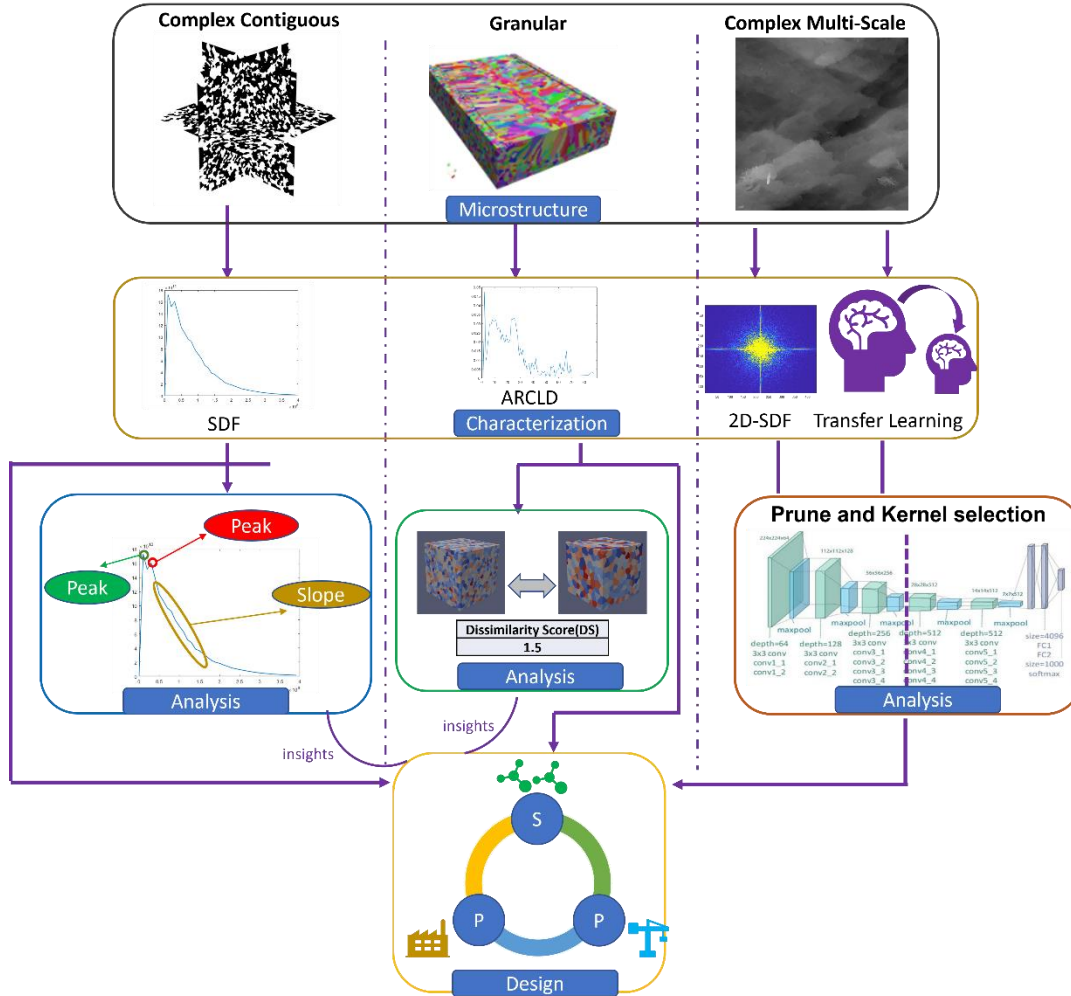


Figure 1-1: Layout of the three major objectives. Left side focuses on contiguous microstructures by leveraging insights obtained from in-depth SDF study and using those for PSP design. Middle column centers on granular microstructures which are characterized by CLD, and then the use of CLD is extended to facilitate design. Right side concentrates on extracting multi-scale information from complex microstructures using a combination of SDF and Transfer Learning to facilitate Structure-Property mapping.

### 1.3 Dissertation Organization

The outline of this dissertation and the interconnected nature of research tasks are shown in Figure 1-2. After laying out the challenges and research objectives in Chapter 1, Chapter 2 will provide technical background on essential concepts and methodologies utilized in the following

chapters. Then, each research task, as mentioned in 1.2, is discussed separately in Chapters 3 through 5. A concise description of MCR webtools developed for NanoMine as well as a three-phase microstructure characterization and reconstruction tool are provided in Appendix. The dissertation concludes in Chapter 6, first with a list of contributions (6.1) and then some future research themes identified by the author (6.2).

## Chapter 2 Technical Background

### 2.1 Microstructure characterization and reconstruction

As per the Microstructure Sensitive Design paradigm, the microstructure of any material system plays a key role in building the PSP linkage. The reason is based on the fact that a material's morphology significantly influences its properties [40], thus it is critical to analyze microstructure. There are three main goals of performing such analysis: (1) facilitate PSP linkages by reducing the high-dimensional microstructure features, (2) understand the effects of various processing conditions on the microstructure, and (3) understand the effect of microstructure on the resulting properties of the material system. The analysis and use of microstructure is referred to as Microstructure characterization and reconstruction (MCR). Before we delve into the details of MCR, let us establish some basic definitions of key components of MCR.

#### 2.1.1 Microstructure

The structure of a material whose scale is large enough to contain sufficient local morphological details, but much smaller than the characteristic length scale of the sample. The term 'micro' in microstructure should not be confused with  $10^{-6}$  meters. It is only indicative of the small-scale of the morphology of the material system. In practice, its meaning can vary widely based on the material system e.g., for solar cells it could be in the order of nanometers, while for some rubber fracture surface it would be in micrometers. Unless otherwise stated, the microstructure in this study consists of only two phases i.e., binary material system. In practice however, there could be multiple phases/elements forming a microstructure.

### 2.1.2 Microstructure Characterization

Reducing the high-dimensional complex morphology of a material system into low dimensional quantities by analyzing different aspects of the microstructure's salient features is called microstructure characterization. This can be achieved by several ways which will be explained in 2.1.2.

### 2.1.3 Microstructure Reconstruction

Microstructure reconstruction involves creating a microstructure statistically equivalent to the original microstructure. It does not have to look identical but the properties under study as well as the microstructure features should be statistically equivalent. These statistical reconstructions are either derived from an actual material image or are pre-defined by the user.

MCR provides powerful tools to researchers to advance material design. In literature, the use of MCR extends to building predictive models [41], design of materials with targeted properties [15,42–44], transformation of 2D experimental data to 3D for computer simulation [45], and microstructure induced uncertainty quantification and propagation [41,46] etc. Broadly, MCR techniques can be put into four categories [10]: Statistical functions, physical descriptors, spectral density function (SDF), and machine learning. In an effort to support material design, we have built tools on an online platform called Nanomine, which enables a novice user to characterize any microstructure using all these techniques except for machine learning. The specifics of these tools are described in Appendix A.1. As SDF will be explained in greater detail in the ensuing chapters, a brief detail on the rest of the characterization methods follows:

## I. Statistical Functions

These functions aim to capture the degree of spatial correlation among different locations in a probabilistic sense. The most basic statistical function is a two-point correlation function,  $S_2(r)$  (Figure 2-1), which basically calculates the probability of finding two points corresponding to the same selected phase, separated by a fixed distance  $r$ . An extension of this approach is three-point correlation functions. Such functions and their higher orders are also referred to as  $n$ -point correlation functions. Other more complicated statistical functions includes cluster correlation functions and lineal-path correlation function. Generally, the more complicated the functions are, the more expensive their computation is.

The reconstruction using such methods can be achieved by casting the reconstruction process as an optimization problem with, microstructure as input  $X$ , and the difference between required microstructure statistics and actual microstructure statistics as the cost function. This optimization usually involves calculating the statistics at every step, and because these tools are expensive to compute, it makes the overall process expensive. Since gradient-based methods are not suited for such optimization, we are left with techniques such as thermal-annealing which make the process even more intractable.

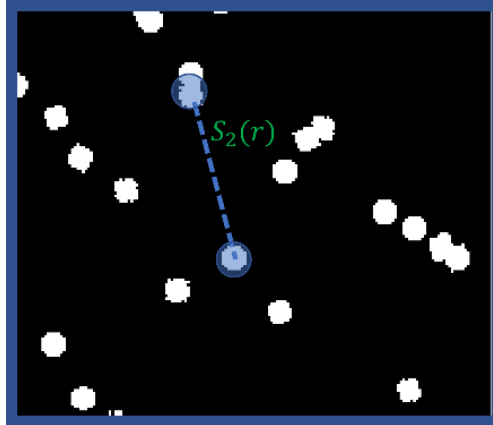


*Figure 2-1: An artificial material system consisting of two distinct phases. The dotted line represents two points separated by a fixed distance in the microstructure. Two-point correlation function determines the probability of finding both the points belonging to the same phase.*

## II. Physical Descriptors

Most of the physical descriptors can be classified as statistical e.g., areas of the matrix-filler system, or grain-size distribution of granular microstructure system. There are only a handful of descriptors which could be classified as deterministic such as volume fraction, or the number of clusters/particles inside a matrix-filler system. Unlike the statistical functions, which can give some basic information about almost any type of microstructure, physical descriptors as more specific as they have implicit underlying assumptions about the material system.

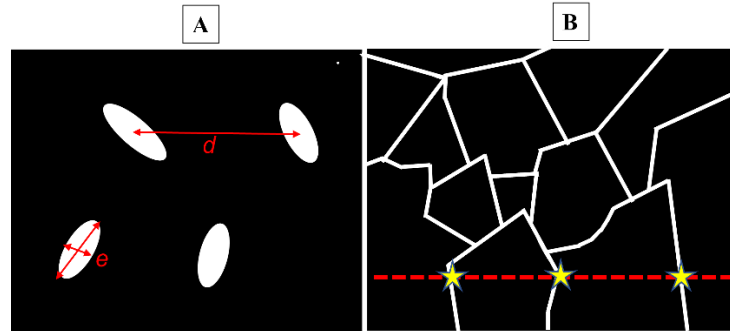


Figure 2-2: Sample microstructure which are suitable for characterization using physical descriptors. (A) is matrix-filler system. (B) is a granular microstructure. The red-dotted line intersects the grain-boundaries to locate the intersections.

For example, in Figure 2-2 A, physical descriptors try to approximate the shape of the fillers as ellipsoids and thus try to calculate the elongation ratio  $e$ . The center-to-center distance,  $d$ , is also calculated by approximating the center of the fillers. On the other hand, in Figure 2-2 B the granular boundaries are identified to extract a different set of statistics about the microstructure. If the two techniques are interchanged, i.e., ellipsoid ratio is calculated for Figure 2-2 B, then the result would be misleading as the grains have no semblance to an ellipsoid.

Depending on the material system, there is a wide variety of physical descriptors that can be extracted. Hongyi Xu et al [47], extracted 56 descriptors for polymer nanocomposites. Some common generic descriptors are listed in the table below:

*Table 2-1: Some common physical descriptors along with their type.*

<b>Serial</b>	<b>Descriptor</b>	<b>Type</b>
1	Volume Fraction	Deterministic
2	Surface area of filler phase	Deterministic
3	Center-to-center distance	Statistical
4	Pore size (inscribed circle's radius)	Statistical
5	Eccentricity	Statistical
6	Principal axis orientation angle	Statistical

### III. Machine Learning

The main advantage of Machine Learning (ML) techniques is that they are applicable to a wider variety of material systems unlike the methods introduced previously which are largely material specific. Potentially even the most complex shapes could be handled by ML techniques. As most of the characterization happens in latent space, therefore, they do not provide an interpretable microstructure characterization. The use of ML in MCR is thus restricted to reconstruction which can involve design without meaningful interpretation of characterization. Reconstruction approaches include supervised learning [48,49] and texture synthesis [50]. On the other hand, design has been achieved by variational autoencoders [51] and generative adversarial [52] networks. These methods are an attractive proposition for microstructure design tasks since they can be used to generate previously unobserved microstructure and thus explore the design space. However, the biggest bottleneck in ML tools is the need of a large dataset to reliably train these ML models, which inherently implies training thousands or millions of parameters. One ML

approach which requires relatively less data is known as Transfer Learning (TL). The details of TL are presented in the next section.

## 2.2 Transfer Learning

Neural networks were developed to mimic the human nervous system for machine learning tasks by treating the learning model's computational units in a manner similar to human neurons. A very basic single layer neural network has the following components (Figure 2-3): (i) input nodes ( $x_1$  to  $x_n$ ), associated weights ( $w_1$  to  $w_n$ ), an activation function, and a response  $y$ . It is called single layer because only one arithmetic operation is performed on the summed values of  $w * x$ . To accurately predict the response  $y$ , the model uses a strategy called back-propagation [53] to calibrate the weights  $w_1$  to  $w_n$ . By adding more neurons in the middle layer (hidden layer), we can predict highly non-linear functions. This is the brilliance of neural networks that potentially, they can predict almost any function no matter the shape by adding more neurons and layers.

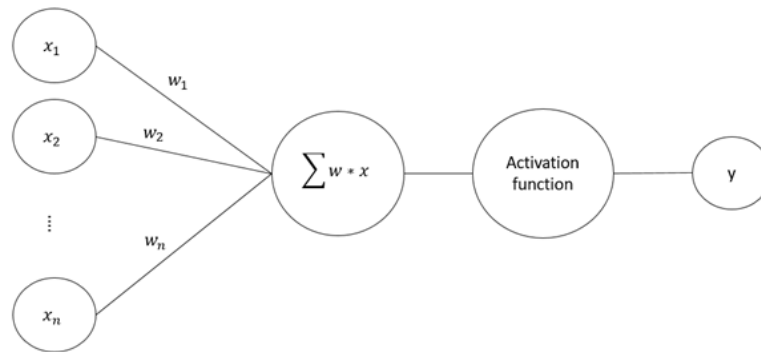


*Figure 2-3: Single neuron Neural Network*

As the number of layers increase, the number of weights to train also increases. The trainable parameters scale very fast with the size of the neural network. The term deep neural

network generally refers to the neural networks having more than 5 hidden layers. The deeper the network (i.e., the greater number of hidden layers it has), the more parameters there are to train. And the more parameter to train, the more data is required. In some deep neural networks, the trainable parameters can reach up to a million and, therefore, result in a massive data requirement. This is especially true for using neural networks for image classification as images are high-dimensional inputs.

For cases where we have limited data, we can utilize the concept of transfer learning [54] to avoid training the weight parameters. In transfer learning, a pre-trained model (i.e., a model whose weights are calibrated) is used to carry out a task which it was not originally trained to do. For example, a model that was trained on classifying items like pencil, cars, etc., is used to classify skin lesions [55].

However, the original model should be trained on a dataset that is broad enough so that it can be useful for the transfer learning task. One well-known dataset for images, known as “ImageNet” was created by Deng et al. in 2009 [56]. This dataset consists of tens of millions of cleanly sorted and accurately labeled images. Based on the ImageNet dataset, there is a ImageNet Large Scale Visual Recognition Challenge (ILSVRC) [57] which is a benchmark in object category classification and detection. The challenge is held annually since 2010 and has produced a lot of efficient deep learning models. Some of the famous deep learning models include: VGG16 and VGG19 [58], Inception [59], Xception [60], etc.

Let us take example of one of the above-mentioned models and show how it can be modified for TL. The network configuration of VGG 19 is shown in Figure 2-4 A. As the name suggests the model consists of 19 layers along with Max-pooling to reduce the dimension in first

five blocks. A block is visualized as the connected layers without having any space in between them, as depicted in Figure 2-4. As the total trainable parameters of VGG 19 are over a 100 million, it will be impossible to train them on a small dataset. To transfer the knowledge of the pre-trained network, we can use the weights of the first sixteen layers and only train the last three layers (Figure 2-3 A). Using pre-trained weights of certain layers is commonly referred to as “freezing the layers”. Another approach of using VGG19 could be that the only the first sixteen layers are used, but the last three layers are replaced by a totally different set of layers as seen in Figure 2-3 B. The customizations of pre-trained networks are limitless and require some expertise in the field of deep learning as well as in its application. More on this will be follow in Chapter 5.

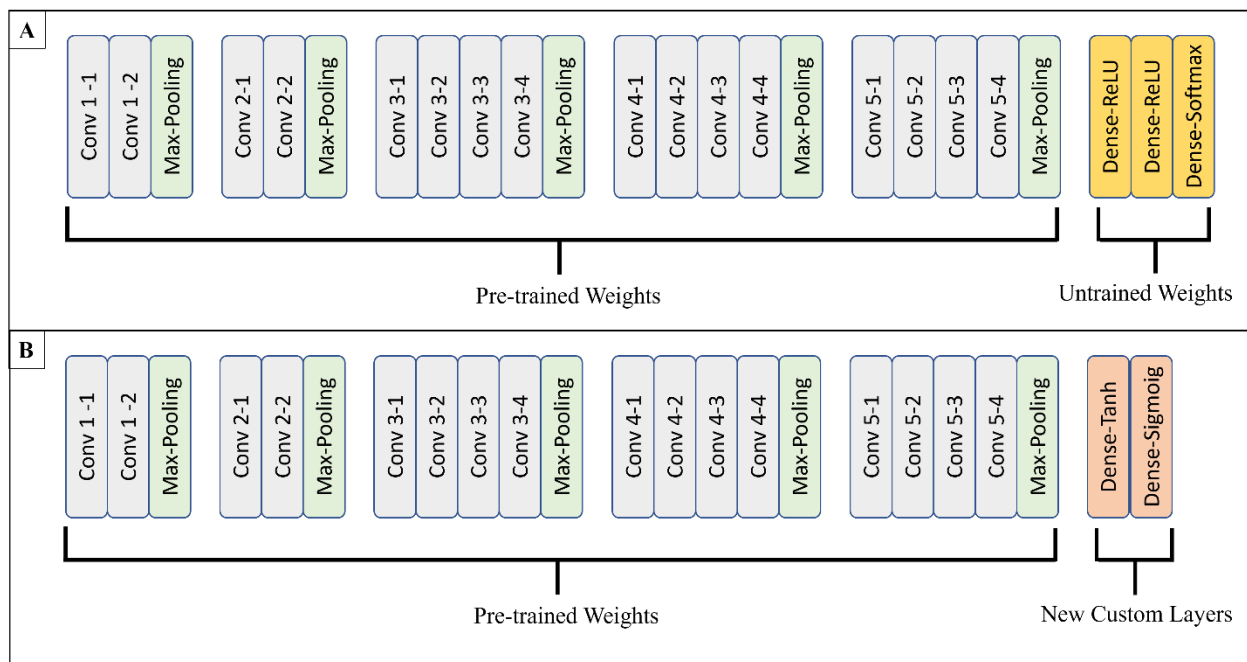


Figure 2-4: Examples of VGG 19 model customizations. The names of the layers are written inside the sub-blocks. (A) the weights of the first 16 layers are frozen, while the last three layers are trainable. (B) The first layers are used as in (A) but the last three layers are replaced with custom two layers.

## 2.3 Bayesian Optimization

Almost all of the material design problems can be formulated as an optimization problem with a design space and bounds based on the domain knowledge. Thus, it is critical to find the most suited algorithm for the specific optimization problem. Among the many optimization algorithms, Bayesian Optimization (BO) stands out because of three specific advantages: (i) it ensures a low number of function evaluations, (ii) it does not use the derivative, and (iii) it is well suited to find the global optima. Consequently, it is mostly suited for highly non-linear unknown functions whose derivative information is not available. However, one major set-back of using BO is that its cost scales very quickly with dimensionality, and dimensions of greater than a dozen become prohibitive.

The objective of BO is to find the optimal combination of design variables,  $x^*$ , out of all possible combinations contained in the design space,  $\Psi$ , such that the predefined function  $f$  is optimized. The optimization could either be cast as minimizing or maximizing. In literature, BO is generally described as a minimizing objective function:

$$x^* = \min_{x \in X} f(x), \quad (2-1)$$

The BO algorithm consists of the following three main steps that are performed iteratively:

**Step 1-** Build a surrogate model on the available dataset and provide uncertainty quantification over the design space. This surrogate model is the updated *posterior*.

**Step 2-** Using an acquisition function to suggest the next likely point  $x_{next}$  by balancing between exploitation and exploration.

**Step 3-** Compute the function  $f$  on the new suggested locations  $x_{next}$ .

These three steps are repeated until the termination criteria is met. Two common types of termination criteria include (i) number of iterations, and (ii) insignificant change in the acquisition function.

There are two major components of BO: (i) a surrogate model that provides predictions along with the associated uncertainties, and (ii) an acquisition function that finds the next point to sample. Gaussian process (GP) is the most common surrogate model used for BO because of its flexibility to capture complex relationships and its convenience for uncertainty quantification. A key element of GP is selecting the applicable kernel for the underlying function. Some common kernels include radial basis function, and WhiteKernel etc. To build an accurate surrogate model, these kernels need to be optimized in order to reduce the maximum likelihood using algorithms such as the one used in the sci-kit learn library of python [37]. The bounds and type of kernel are selected based on experience with solving the well-known complex three-humped camel function efficiently.

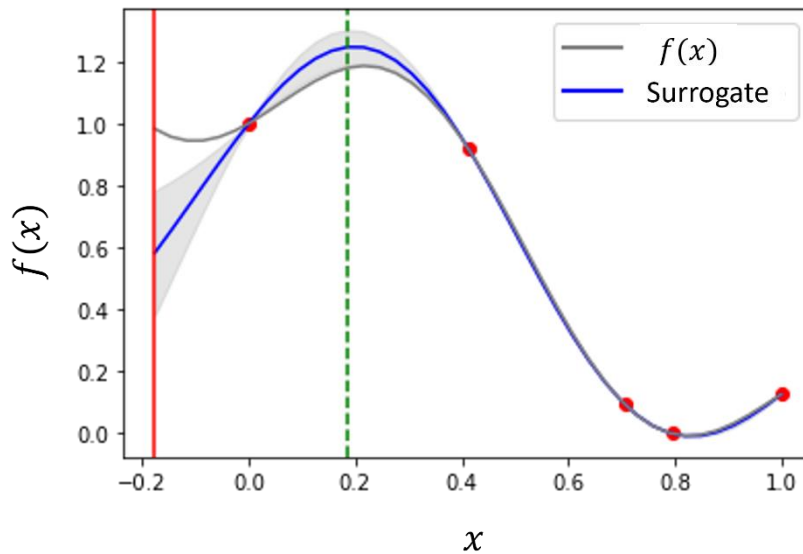


Figure 2-5: Surrogate model for an unknown function ( $f(x)$ ). Red dots represent initial samples. The grey shaded region represents uncertainty (95% Confidence Interval). The green dotted line represents the maximum of surrogate function, whereas the red solid line represents the point with maximum uncertainty.

For illustration, a GP surrogate model is built for an unknown function,  $f(x)$ , using an initial set of five data points in Figure 2-5. Not only did the surrogate match the shape of the unknown function well, but it also computes the uncertainty which is shown as the grey region. To update the posterior, BO uses exploration-exploitation trade-off. In the context of the given example in Figure 2-5, exploration refers to looking at the points with highest uncertainty i.e., the points which the model is most unsure about. The point with the highest uncertainty is plotted as a red vertical line. Exploitation, on the other hand refers to maximizing the current surrogate model i.e., the point where the model predicts will give the maximum value. To help with this decision of exploration-exploitation trade-off, BO uses an acquisition function.

An acquisition function that encourages too much exploitation and limited exploration may end up in a local maximum. Whereas an acquisition function that encourages too much

exploration, may end up taking a lot more function calls. Thus, selecting the appropriate acquisition function is critical in the BO process. Some common acquisition functions include probability of improvement, upper confidence bound and Expected Improvement (EI) [61]. Because of its popularity over others and an added advantage over PI i.e., it accounts for the size of improvement, it is preferred over PI. EI can be defined as:

$$EI(\mathbf{x}) = \mathbb{E}[\max(0, f(x) - f_{max}) | \mathcal{X}, y], \quad 2-2$$

where  $f_{max}$  is the best value found so far in the observed points  $\mathcal{X}$  that have outputs  $y$ . The above equation could further be elaborated by replacing generic terms with their statistical equivalents:

$$EI(\mathbf{x}) = (f(x) - f_{max}) \Phi \left( \frac{m(\mathbf{x}) - f_{max}}{s(\mathbf{x})} \right) + s(\mathbf{x}) \phi \left( \frac{m(\mathbf{x}) - f_{max}}{s(\mathbf{x})} \right), \quad 2-3$$

where  $m(\mathbf{x})$  and  $s(\mathbf{x})$  are the mean and standard deviation of the posterior GP.  $\Phi(\cdot)$  and  $\phi(\cdot)$  are the cumulative distribution function and probability density function of the standard normal variable. Now it is easier to notice that the left side of the equation 16 is pertaining to exploitation, whereas the right side is pertaining to exploration.

Once the acquisition function is selected, we compute it over the entire domain to find the next sampling point,  $x_{next}$ , with the maximum acquisition score. This new point is then used to find the corresponding value of  $y_{next}$ . Both  $x_{next}$  and  $y_{next}$  are then added to the original sample space of  $\mathcal{X}$  and  $y$  respectively. Next the GP model is updated based on these new points, and again the acquisition function is calculated to find the next best point. These steps are iterated until we reach our termination criteria as explained earlier using the three main steps of BO.

## 2.4 Summary

This chapter reviewed some technical fundamentals that we will need for the development of work in later chapters. As the majority of this work revolves around microstructure analysis, thus MCR techniques reviewed in Section 2.1 will be used throughout the remaining chapters. Transfer Learning discussed in Section 2.2 will be used and further elaborated based on use in Chapter 5. Lastly, BO introduced in Section 2.3 will be used in Chapter 4.

After providing some technical background of some of the concepts, we can now move towards building and enhancing current characterization and analysis tools for material design. The first material type that we will focus on is polymer material system.

## Chapter 3 SDF-based Analysis for Polymer Material System

### 3.1 Introduction

Polymer material system can be considered a quasi-random microstructure material system. Quasi-random microstructure material system are those in which the microstructure is random rather than regular, i.e., does not consist of cells or repeating lattices. But this randomness is still governed by some underlying relationship. In such irregular material systems, characterization of the microstructure is very challenging. Among the many MCR techniques introduced in Section 2.1, n-point correlation functions could be used to characterize such materials. But these correlation functions do not have a physical meaning and neither possess one-to-one mapping to nanomanufacturing process conditions [12]. Additionally, the shape of such functions is hard to parameterize which is critical to reconstruct such microstructures for design purposes. And since physical descriptors (Section 2.1) are suited for characterizing more regular material system, they cannot be used in this case as well.

SDF, which has Fourier Transform (FT) in its core, is a more suitable candidate as FT has been found to be sufficient to represent quasi-random microstructures from bottom-up processes [62], as well as any other heterogeneous microstructures [21]. Lastly, SDF has also been shown to have relationship with physical phenomenon such as light trapping [12].

Because of all the advantages of SDF listed above, it becomes an effective candidate for characterization of polymer material systems. Even though SDF is quite popular for microstructure analysis, a lot of gaps exist in its understanding. Thus, in Section 3.2 we start with gaining insights into SDF. Next, in Section 3.3, we present a SDF centered design framework for the design of

quasi-random microstructures. In Section 3.4, we extend the use of SDF to use it to reconstruct larger samples from smaller samples using a new method named “SDF frequency resolution-enhancement”. Lastly in Section 3.5, we apply this new utility of SDF to do multi-fidelity optimization of organic solar cells. The chapter concludes with a summary of the findings and contributions.

### 3.2 Understanding SDF

SDF is an analytical approach to characterize the structural information of a given material. Using Fourier transform (FT), SDF can extract information regarding the real space structural features. SDF has demonstrated its ability to characterize intricate heterogeneous microstructures as well as generate statistically equivalent reconstructions [10]. For isotropic materials, the shape of radially averaged SDF curve generally takes a simple parametric form which significantly reduces the design complexity of an otherwise high dimensional material structure. But the parameters of the SDF curve so far have not been systematically investigated, and thus lack physics-based intuition. One challenge in understanding the parameters is that SDF can take many different forms for different material systems. Two examples from literature are shown here: one SDF resembles the shape of a truncated gaussian (Figure 3-1), and another SDF has the most prominent feature of a peak and decay (Figure 3-2). This requires material specific parameterization techniques. Additionally, the parameterization in the past studies has been selective; it focused on only the low frequency portion of the curve [12,14]. Not to mention that the parameterization does not entirely capture the intricacies of the curve (notice the difference in the blue and red curves in Figure 3-1 and Figure 3-2). All this means is that there may be some important information missing in the parameters. That is why there is a need to understand the

curve and discover the most important features so they can be focused upon for interpreting a material or designing a property.

In this section, first a brief technical background of SDF is presented which is followed by an empirical study aimed at discovering links between physical phenomenon (descriptors) and SDF features to forward the understanding of SDF.

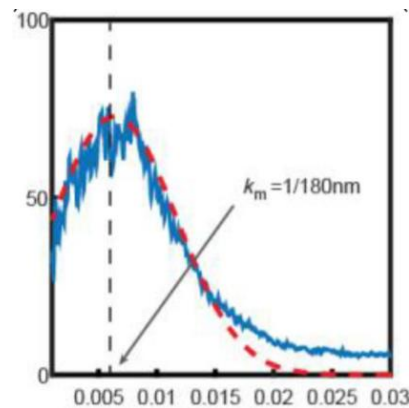


Figure 3-1: SDF of a quasi-random microstructure from Yu et al. [12]. Blue is the original curve and red is approximation.

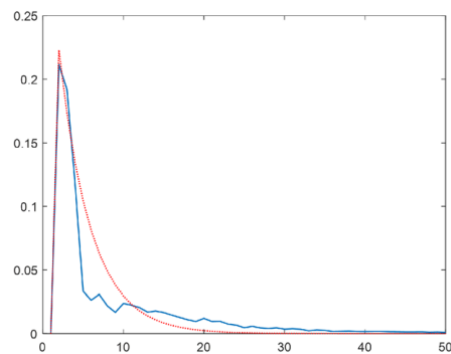


Figure 3-2: SDF of an OPVC material from Ghumman et al. [14]. Blue is the original curve and red is the approximation.

### 3.2.1 Introduction to SDF

To characterize a microstructure using SDF, a two-phase image,  $X$ , is required. The image must contain high resolution details at the microstructural level. The Fourier transform of the image is calculated as:

$$F(\mathbf{k}) = F[X] = A_{\mathbf{k}} e^{i\phi_{\mathbf{k}}} . \quad (3-1)$$

Here,  $F[.]$  represents the FT operator,  $k$  is a vector which represents frequency,  $i = \sqrt{-1}$ , and  $A_{\mathbf{k}}$  and  $\phi_{\mathbf{k}}$  represent the magnitude and phase angle of the FT, respectively. For isotropic materials, the vector  $\mathbf{k}$  can be reduced to a scalar by radially averaging in the spatial frequency domain. Thus, the SDF of the microstructure, is then calculated by radial averaging of the squared magnitude of FT.

$$\rho(k) = \frac{\int_0^{2\pi} |F(k)|^2 d\theta}{2\pi} = \frac{\int_0^{2\pi} A_k^2 d\theta}{2\pi} . \quad (3-2)$$

This gives a 1-D  $\rho(k)$  function.

The resulting SDF plots can take various forms. Two examples of microstructures and their corresponding 1-D SDF plots are shown in Figure 3-3. The widely used 2-Point Correlation Function (CRF) is equivalent to inverse FT of SDF, but compared with 2-point CRF, SDF is more convenient in differentiating spatial correlation features as evidenced in Figure 3-3. Figure 3-3 (a) and (b) represent two nanostructures with different structural properties. Figure 3-3 (b) is an image of an ordered structure and has one distinctly strong correlation at a specific band of spatial frequency (Figure 3-3 (d)). This feature is also visible in the insets of Figure 3-3 (b) by a distinct circle in the Fourier spectrum. In contrast, Figure 3-3 (a) is less ordered and hence its SDF is more dispersed over the entire frequency spectrum (Figure 3-3 (c) ). These differences in SDF which are based on structural changes confirm the efficacy of SDF in capturing the structural detail.

Furthermore, the SDFs observed in Figure 3-3 (c) and (d) both assume a simple shape that can be easily parametrized. The parametrized SDFs are represented as red dashed lines in Figure 3-3 (c) and (d). For Figure 3-3 (c), the SDF curve resembles a truncated Gaussian function, while for Figure 3-3 (d) it looks closer to a step function. Note that all the SDFs presented in this study are normalized for ease of comparison and consistency unless otherwise mentioned. In this chapter SDF has been exclusively used to characterize and reconstruct two-phase microstructure, but we have extended the use of SDF to characterize and reconstruct three-phase microstructures (Appendix A.2).

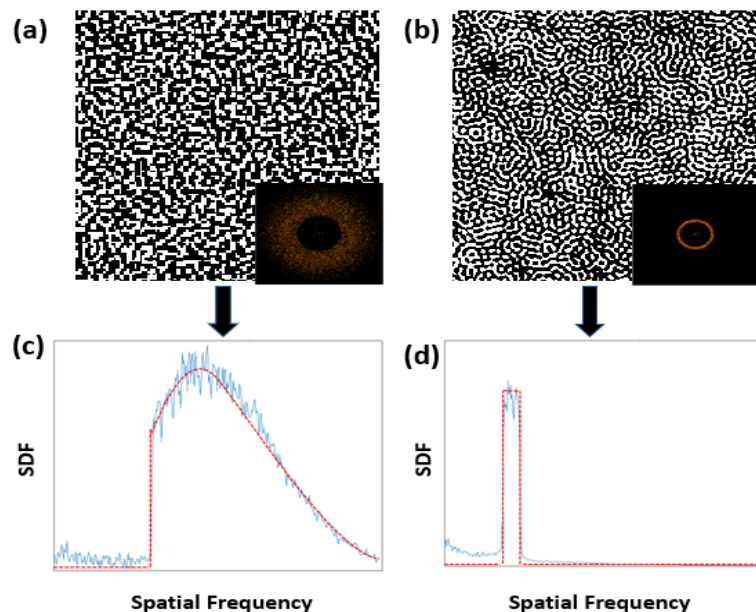


*Figure 3-3: Two sample microstructures (a & b) along with their Fourier spectrum in the insets; (c & d) are the final 1-D SDFs of each image. Red dashed line represents the approximated SDF.*

### 3.2.2 Studying the relationship between descriptors and SDF

In this sub-section, the shape of the SDF curve is explored to understand its critical features, which will consequently help us understand the targeted microstructures in greater detail. The main

idea is to generate images with specific characteristics/descriptors and then characterize them using SDF to delineate the relationship between SDF and descriptors.

Instead of using complex contiguous microstructural images which are harder to control and reconstruct, simple particle-based images are used. The key factors which were varied include particle size ( $S$ ), particle shape, average nearest neighbor particle distance ( $d_{nn}$ ), number of circles ( $N$ ), and the window size ( $W$ ). By changing these factors one at a time, changes in SDF curves were observed to deduce a possible correlation. Note that all units of distance are in pixels unless otherwise stated. The following results and conclusion were obtained based on the empirical study.

#### *3.2.2.1 Effect of nearest neighbor distance*

Three binary images were created by varying the nearest neighbor distance ( $d_{nn}$ ) to 20, 40 and 60.  $N$  depended on  $d_{nn}$  to fill the entire space. Rest of the factors were set as Shape= Circle,  $W = 200$ , and  $S = 4$ . As can be seen in Figure 3-4., the particles are more dispersed in (c) than (b), and more spread out in (b) than (a). Figure 3-5 reveals that the major difference between the three microstructures is their periodicity. The greater the distance, the more oscillations of the SDF can be observed.

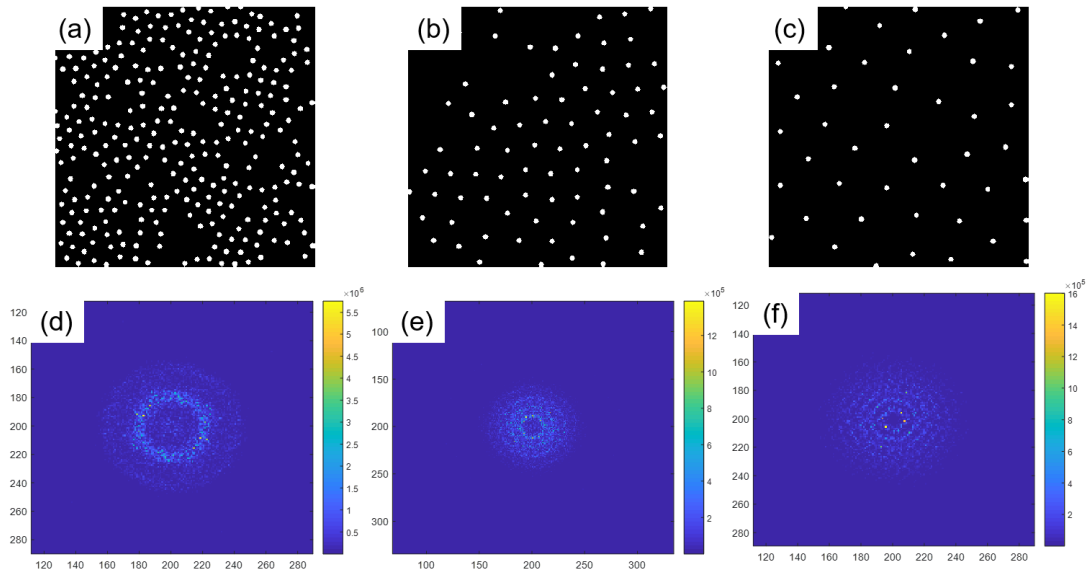


Figure 3-4: a-c are images with circles of radius 4 are spread out at distances of approximately 20, 40 and 60 respectively. d-f are their respective Fourier transforms.

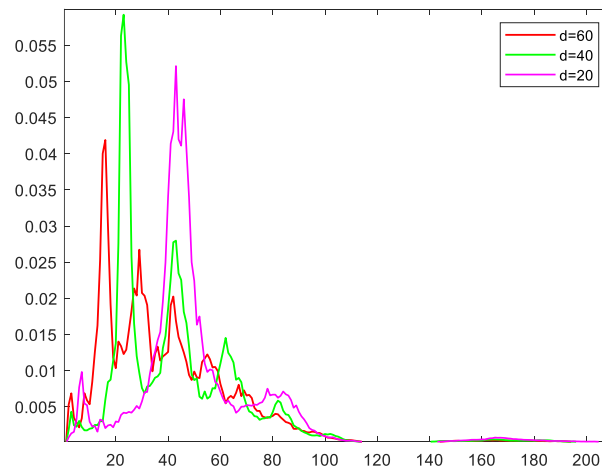


Figure 3-5: SDF plotted for the three cases showed in Figure 3-4. Note that x-axis are arbitrary units.

### 3.2.2.2 Effect of particle size

Here the size of particles,  $S$ , was varied to take on the values of 4, 8 and 12. All other factors remained constant: Shape= Circle,  $N= 40$ ,  $W= 200$ , and  $d_{nn}= 20$ . Figure 3-6 and Figure 3-7 indicate that the SDF decayed much faster when the size of the circle was increased.

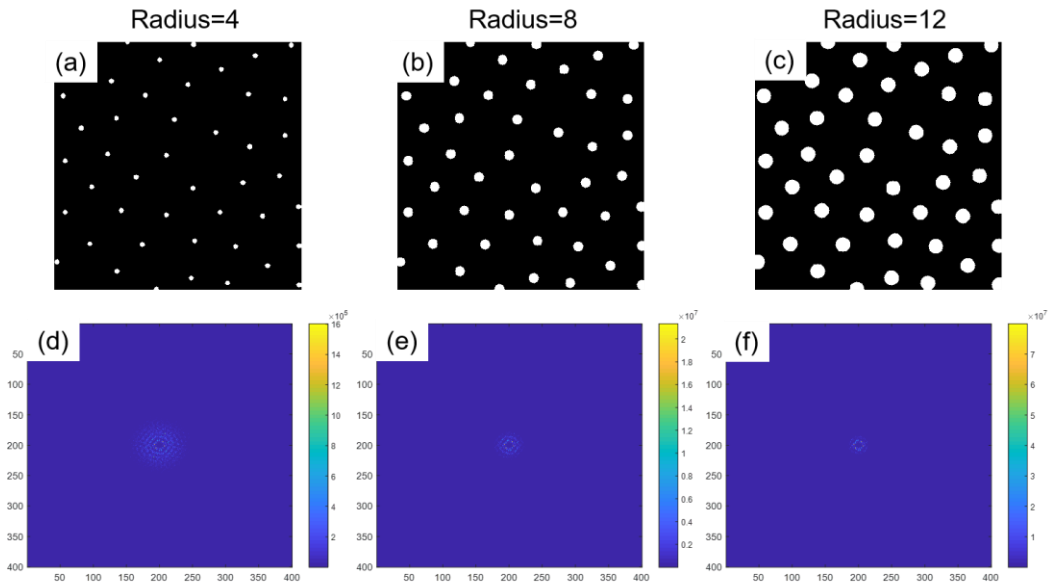


Figure 3-6: *a-c* are images with circles of radius 4, 8 and 12 respectively. *d-f* are their respective Fourier transforms.

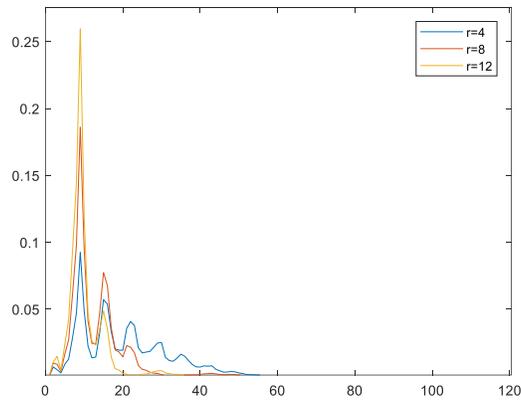


Figure 3-7: SDF plotted for the three cases showed in Figure 3-6.

### 3.2.2.3 Effect of image size

In this study the window size,  $W$ , was changed by cropping a larger image of 600 pixels into two smaller images of size 400 pixels and 200 pixels. Consequently  $N$  changed, but cropping was performed as to keep the volume fraction consistent. All other factors remained constant: Shape= Circle,  $S=4$ , and  $d_{nn}=20$ .

By observing the respective Fourier transform of three images in Figure 3-8, it is noted that there is a decrease in the intensity/brightness of the spectrum. The reason for this remains inconclusive. To further understand the features, SDF is plotted in Figure 3-9. It is observed that there is a peak-type feature from  $0.22 \text{ pixel}^{-1}$ . This frequency corresponds to the physical sizes of 4.5 pixels. And the radius in our case is 4 pixels. Another noticeable peak occurs around  $0.1 \text{ pixel}^{-1}$  which corresponds to 10 pixels. And 10 pixels is the fixed distance between the circles. After explaining the two prominent peaks, the initial peak feature from 0 up till  $0.05 \text{ pixel}^{-1}$  is still not understood very well and requires further investigation. The final observation from these plots is that the noise (or the random up and down features of the curve) increases with the decrease of the window size. A possible reason deduced is that the controlled correlations (the fixed nearest neighbor distance) in the larger images dominate the random unintended correlations. Whereas for the smaller images, the occurrence of controlled and intended correlations does not hugely outweigh the occurrence of random unintended correlations.

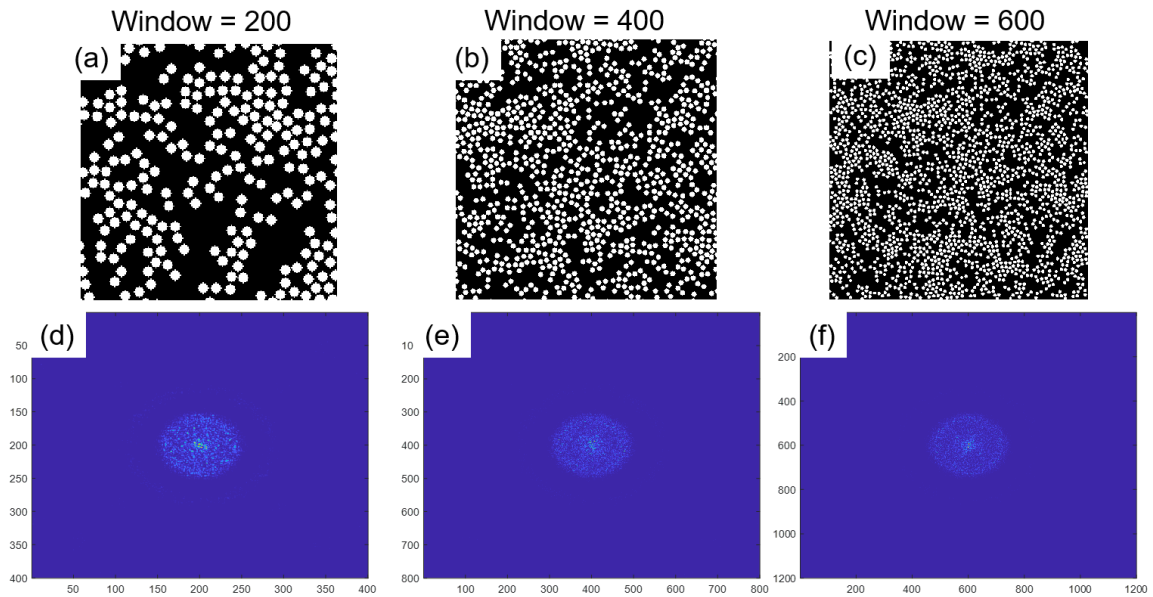


Figure 3-8: *a-c* are images with circles of radius 4, and window sizes of 200, 400, and 600 respectively. *d-f* are their respective Fourier transforms.

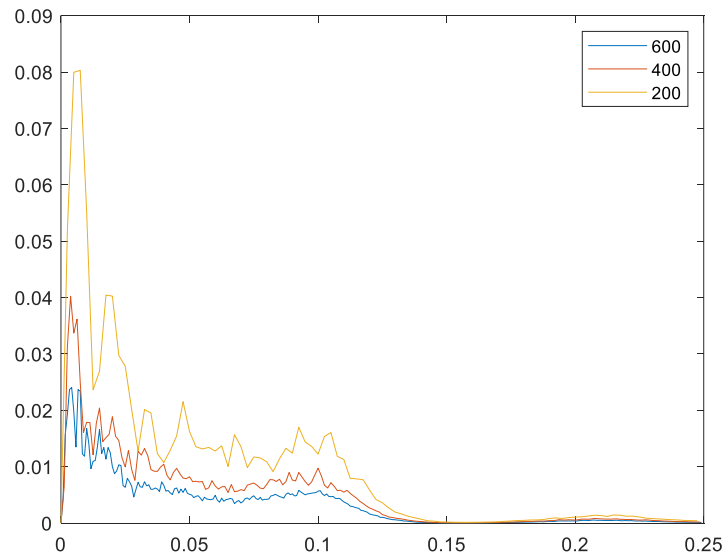


Figure 3-9: SDF plotted for the three cases showed in Figure 3-8.

### 3.2.2.4 Effect of increasing the number of circles

In this study  $N$  was varied while rest of the factors remained constant: Shape= Circle,  $S=4$ ,  $W=400$ , and  $d_{nn}=10$ . Looking at the SDF of three cases in Figure 3-11, there is no major difference between the three. One subtle difference is that as the number of circles increased, the peak at  $0.1 \text{ pixel}^{-1}$  (corresponding to the physical size of 10 units which is the nearest neighbor distance) became more prominent. This directly suggests that if the frequency of the correlation incidents is higher, i.e. the number of times two particles are found at a fixed distance would be larger, it will result in a greater magnitude of SDF peak. Again, like previous study, the peak to the left of  $0.5 \text{ pixel}^{-1}$  is still left unexplained.

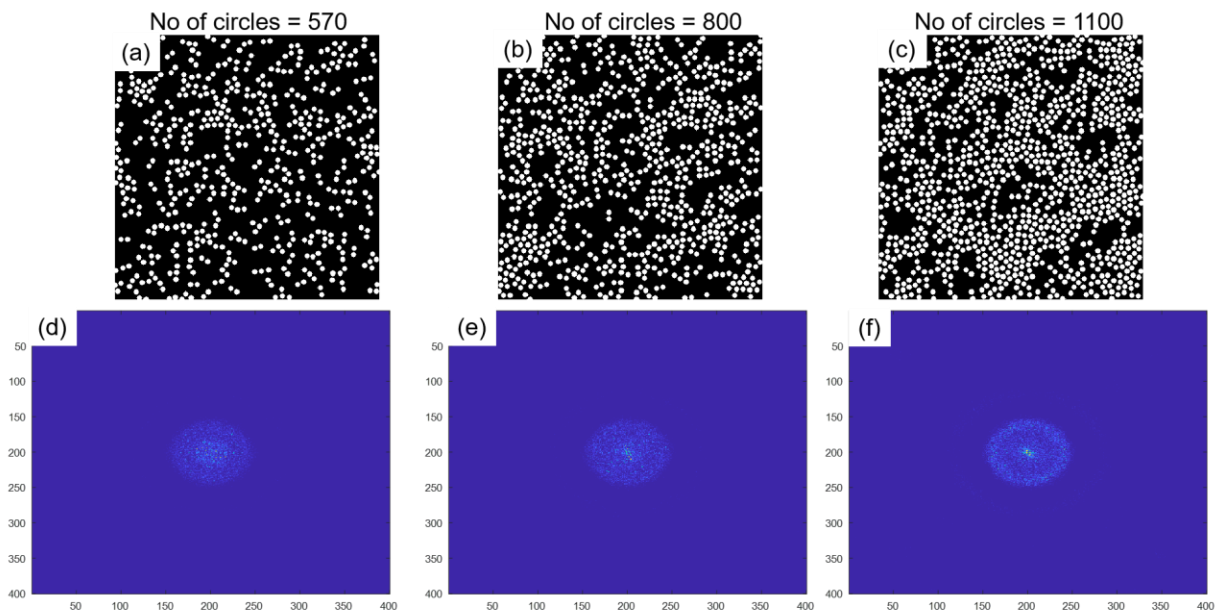


Figure 3-10: *a-c* are images with circles of radius 4, and numbers of circles as 570, 800 and 1100 respectively. *d-f* are their respective Fourier transforms.

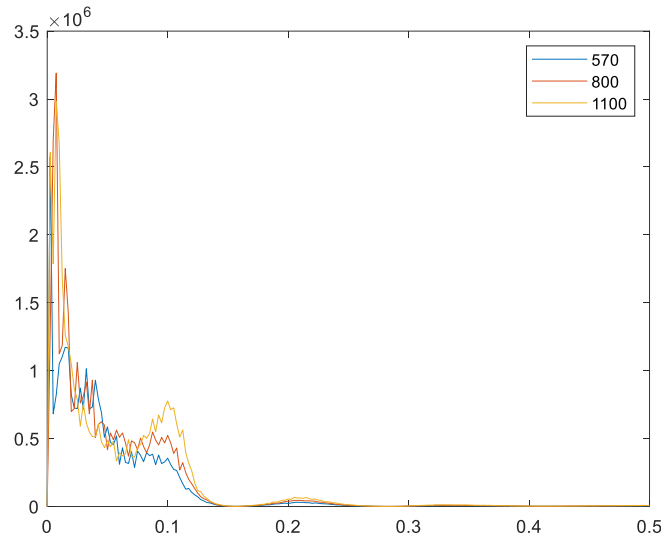


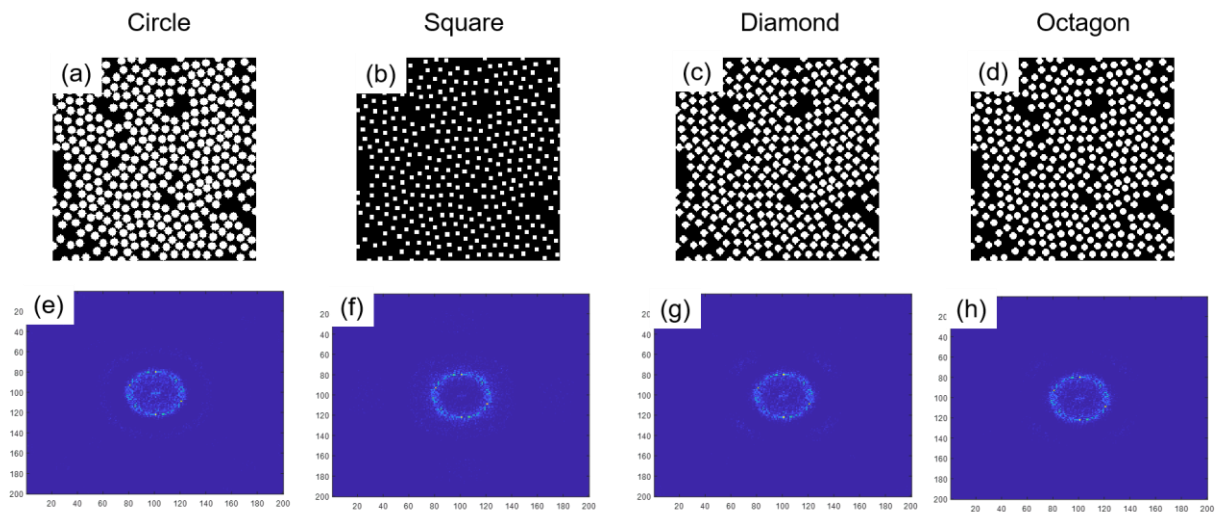
Figure 3-11: SDF plotted for the three cases showed in Figure 3-10.

### 3.2.2.5 Effect of changing the local geometry

In this study the shape, or local geometry, was varied while rest of the factors remained constant:  $N = 200$ ,  $S = 4$ ,  $W = 400$ , and  $d_{nn} = 10$ . Four shapes were selected: Octagon, circle, diamond and square. Their Fourier transforms are shown in Figure 3-12, and the SDFs are plotted in Figure 3-13. Octagon, diamond, and circle result in a very similar SDF. A small difference occurs near the third peak around  $0.26 \text{ pixel}^{-1}$  region where the circle deviates from the other two. This third peak was previously believed to be related to the size of the circle, so this difference is understandable as diamond and octagon are a bit different in size. Square on the other hand does not have a third peak around the same region because its smaller size (side=4). Its third peak is located at roughly  $0.38 \text{ pixel}^{-1}$  (which is equal to 2.6 units – almost equal to half the diagonal of the square). Additionally, also because of the smaller size, the third peak is not very prominent. Another important observation here is that the SDF of the square image has a relatively smaller first peak, while the circles create the biggest first peak. This leads to the deduction that the very

first peak corresponds to the connectedness of the particles; the more connected the particles, the higher the first peak. The last finding here suggests that the distance of the correlation also has a significant contribution. If the correlation is the same at lengths 5 pixels and 10 pixels, the peak corresponding to 10 pixels would be much larger. The next study confirms this hypothesis.

*Figure 3-12: a-c are images with 200 intrusions in the shape of circles, squares, diamonds, and octagons respectively. d-f are their respective Fourier transforms.*



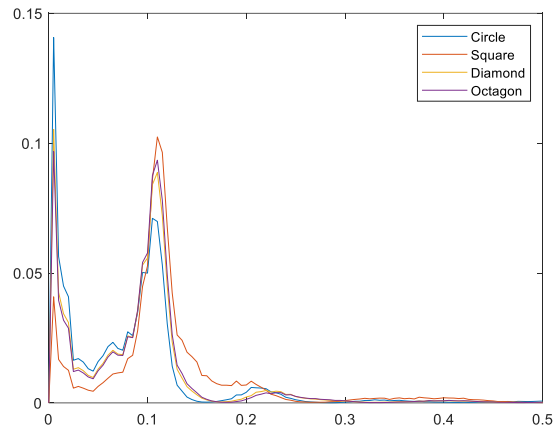


Figure 3-13: SDF plotted for the three cases showed in Figure 3-12.

### 3.2.2.6 Effect of changing only the nearest neighbor distance

To verify the hypothesis in previous study, images with only dots were created with two different nearest neighbor distances:  $d_{nn}=20$  and 25. Rest of the factors remain unchanged:  $= 40$ ,  $S= 1$ ,  $W= 200$ . Instead of using only one image for each nearest neighbor distance, two statistically equivalent images were used. The resulting images along with their SDFs are shown in Figure 3-14.

Because the number of particles ( $N$ ) are the same, the occurrences of controlled correlations are same. If there is no other factor involved, then the peaks formed should have the same magnitude even though the locations would be different. But looking at Fig. 12(e), this is not what is observed. The peaks of  $= 25$  have a higher magnitude confirming the hypothesis stated in earlier study i.e. distance of correlation has an impact on magnitude of the curve; the larger the distance, the greater the magnitude.

Though this study confirms the explanation of magnitude, but it raises another question about the peaks that precede and follow the main peak. The peaks to right of this main peak should

be indicative of correlations at even a smaller length scale. But there does not exist any feature at a length scale shorter than the nearest neighbor distance. This requires a more detailed investigation and continuation of the SDF study.

One last observation is that the main peak for  $d_{nn}=20$  occurs around 0.05 (which corresponds to 20 pixels), and for  $d_{nn}=25$  occurs at 0.04 (which corresponds to 25 pixels). This further validates the understanding of the most dominant peak.

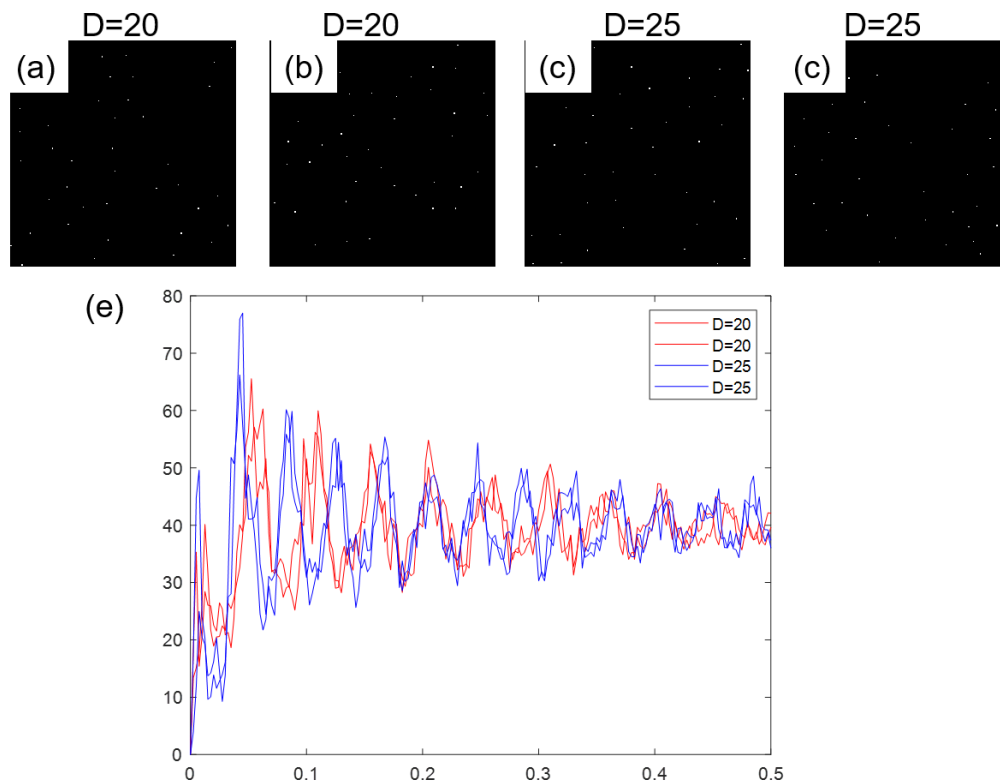


Figure 3-14: (a) and (b) are images created with nearest neighbor distance of 20. (c) and (d) are images created with nearest neighbor of 25. The number of dots/clusters is fixed to 40. (e) represents the SDF of the (a-d) images.

### 3.3 SDF based design framework

Under the framework of MSD [8], materials are viewed as a complex structural systems that can be optimized for achieving improved performance. In this section, we present an SDF based microstructure design framework (Figure 2) that can be employed for the design of quasi-random microstructural systems considering its PSP relation. For the framework discussion that follows, we select OPVC as our material of interest.

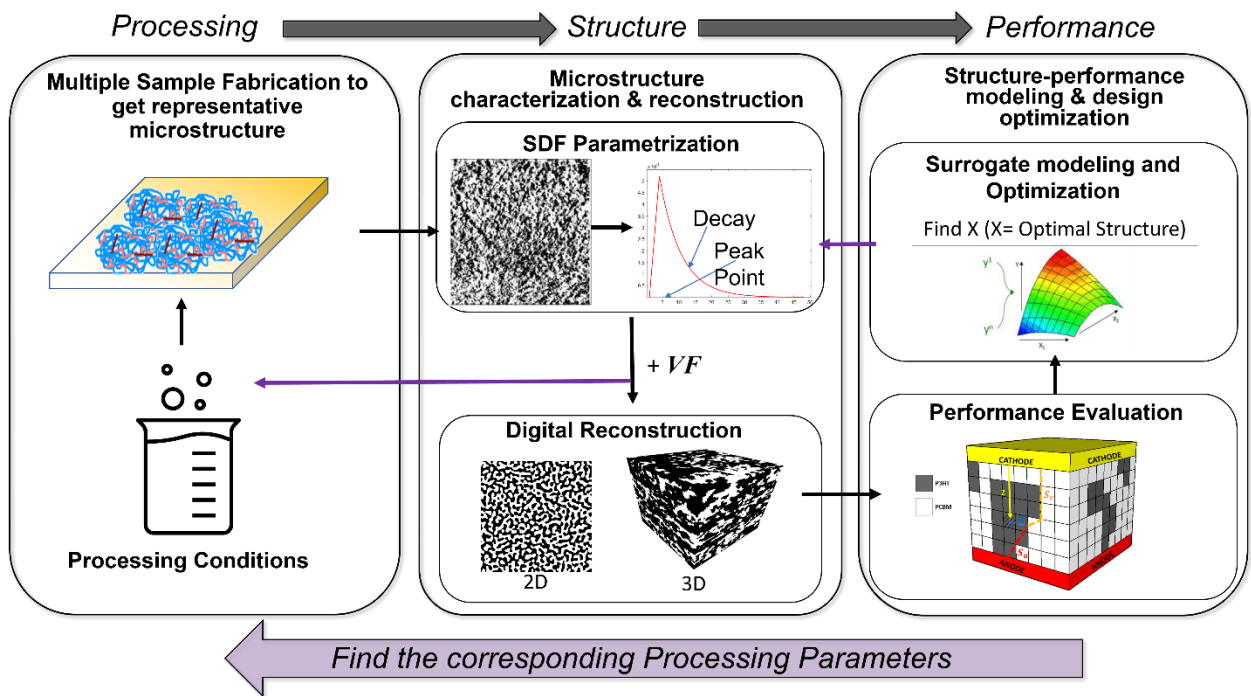


Figure 3-15: SDF-based design framework to find optimal processing conditions of any quasi-random material.

The key idea of the framework (Figure 3-15) is to use SDF to reduce the dimensionality of the OPVC microstructures and enable inverse design through forward PSP prediction. The framework begins by fabricating a set of samples by changing the processing conditions such that the produced samples are representative. Next, microstructure details are captured by imaging techniques which enables the microstructure to be characterized by SDF. A crucial role of SDF is

that it generally allows to be parameterized by a handful of parameters (2 to 4 for certain materials). This allows us to link the microstructure to processing conditions i.e., Process-Structure (PS) mapping. Another benefit of SDF is that it enables us to reconstruct a statistically equivalent microstructure (2D or 3D) very efficiently which can be a representative volume element (RVE). To evaluate the performance of an RVE, a model is developed that accounts for structural features in addition to device physics and material properties. For OPVCs, the core performance indicator is IPCE. This can be achieved by using an IPCE computation tool that predicts the IPCE value for a given microstructure  $\mathbf{X}$  [14]. This tool computes the influence of microstructure on known physical phenomenon of light conversion which can be used to establish the Structure-Property (SP) relationship that forms the basis for performance optimization. Depending on the size of the RVE and its resolution, the computational cost of the performance model could be considerable. For example, an RVE having 1000 pixels in each of the 3 dimensions can take up to 1 hour to compute. To mitigate this cost, a surrogate model can be built and used for design optimization. Design optimization is performed with the pre-determined design variables: volume fraction and parameterized SDF variables. The output from the design optimization are the optimal microstructure parameters corresponding to the best IPCE value. As the optimal microstructure parameters are the SDF parameters, they can be mapped back to the processing parameters using the already established PS model.

In the presented SDF based material design framework, the role of SDF is to leverage its characterization, parameterization, and reconstruction ability to enable PS and SP mapping. This in turn facilitates the design of materials with quasi-random microstructures. A key assumption of this framework is that the material microstructure can be sufficiently characterized by SDF.

### 3.4 SDF frequency resolution enhancement

One major benefit of using statistical methods including Fourier-based methods for material characterization is that theoretically the significant features of a microstructure can be captured by a much smaller sample from a large image of a microstructure given enough details are present inside the smaller sample. As shown in Figure 2, the SDF of a large microstructure and the sub sample both have the same approximated shape i.e., a step function, with the same width. Only the magnitudes differ which is mostly irrelevant for the purpose of characterization using SDF. Consequently, we observe how a smaller microstructure can be used for characterization.

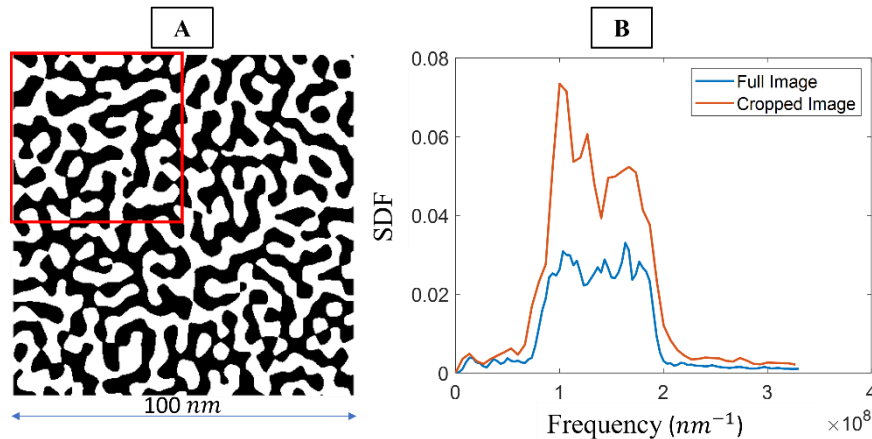


*Figure 3-16: Comparison of the SDF at different length scales of the same material. The SDF of the full microstructure (Figure 2A) is represented by the blue function (Figure 2B), and the SDF for the red inlay (Figure 2A) is represented by the red function (Figure 2B).*

But material design most often does not stop at characterization and very often a reconstruction is required either to enhance the dataset or to evaluate properties from the digital image. To reconstruct the statistically equivalent microstructure, SDF is constrained by the sampling frequency. The sampling frequency depends upon the number of samples, and that in turn depends upon the number of pixels of an image. Taking examples from Figure 3-16, the

original image of the microstructure has 200 pixels in each direction, and the smaller one has only half of that i.e., 100. As a result, SDF has 100 frequency bins from original image, and 50 frequency bins from cropped image. As per the Nyquist frequency limit, the maximum frequency for both is:  $f_{max} = \frac{1}{2\Delta}$ , where  $\Delta$  is the physical distance represented by one pixel in the microstructure image. Since  $\Delta$  is same for both images,  $f_{max}$  is will also be the same. However, because the number of bins is different, each of these bins has a size of  $3.33 \times 10^{-6} \text{ nm}^{-1}$  and  $6.67 \times 10^{-6} \text{ nm}^{-1}$ , for original and cropped image respectively. Because of this difference in the two SDFs, if we were to reconstruct an image using the SDF from a small sample, we would only be able to reconstruct a microstructure of similar size i.e., 50 nm.

To overcome this limitation, we propose an SDF frequency enhancing technique which will help us reconstruct a larger microstructure from the original sample. Since the final size of the microstructure depends on the frequency-resolution of the SDF function, we propose a new technique to enhance it. This can be achieved by duplicating the elements in each frequency bin

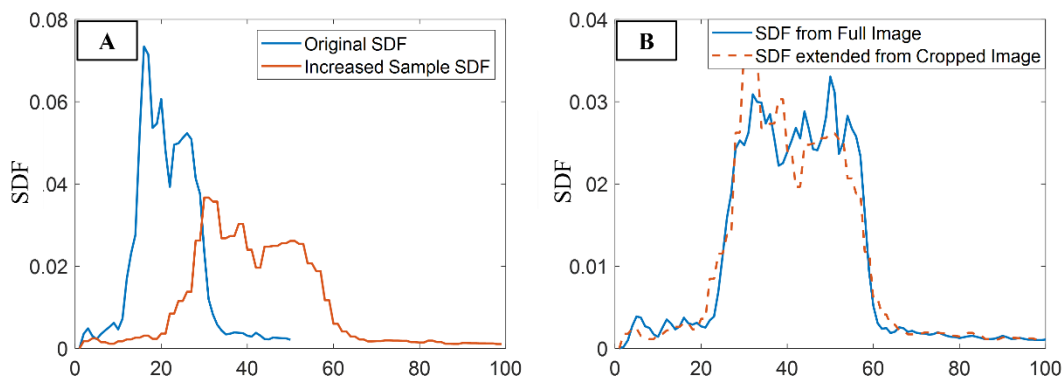


Figure 3-17: SDF frequency resolution enhancement. (A) Duplicating values in each bin of SDF to increase the number of frequency bins by two. (B) Comparing the SDF of the original full image of microstructure with the enhanced SDF of the cropped image of microstructure. Note that x-axis here is only the index of frequency bin and not the frequency itself.

multiple times to add the missing information. As seen in Figure 3-17 A, we repeat each element in a bin two times to extend the SDF to double its size. For the given example it means that we have divided the increment of  $6.67e-6 \text{ nm}^{-1}$  into two bins of  $3.33e-6 \text{ nm}^{-1}$ , and thus doubled the number of total bins to 100. If we compare this new extended SDF with the original SDF of the entire image from Figure 2A, we see that they match very accurately in Figure 3B.

To demonstrate the efficacy of this approach, we present another example in Figure 3-18 of an actual OPVC microstructure. We start by a 20 nm CGMD simulation and characterize its microstructure using SDF. Then we extend the SDF by a factor of four and use that for reconstruction. The resultant microstructure is thus  $20 \times 4 = 80 \text{ nm}$ . If we crop a 20 nm sample from the large microstructure and compare its SDF, we can observe that it looks identical to the original SDF of the 20 nm simulation. Hence in this section we conclude the evidence of the efficacy of using frequency enhancement to reconstruct larger samples from a small sample using SDF.

A caveat with this approach is that we are extending the SDF curve by trying to add artificial information for the small frequency indices so there is some approximation of the SDF curve of the larger sample. Thus, these reconstructions cannot entirely replace the larger simulations. Another approach to extend the SDF could be to interpolate between the missing frequencies to get a smoother curve, but the result would only be slightly different.

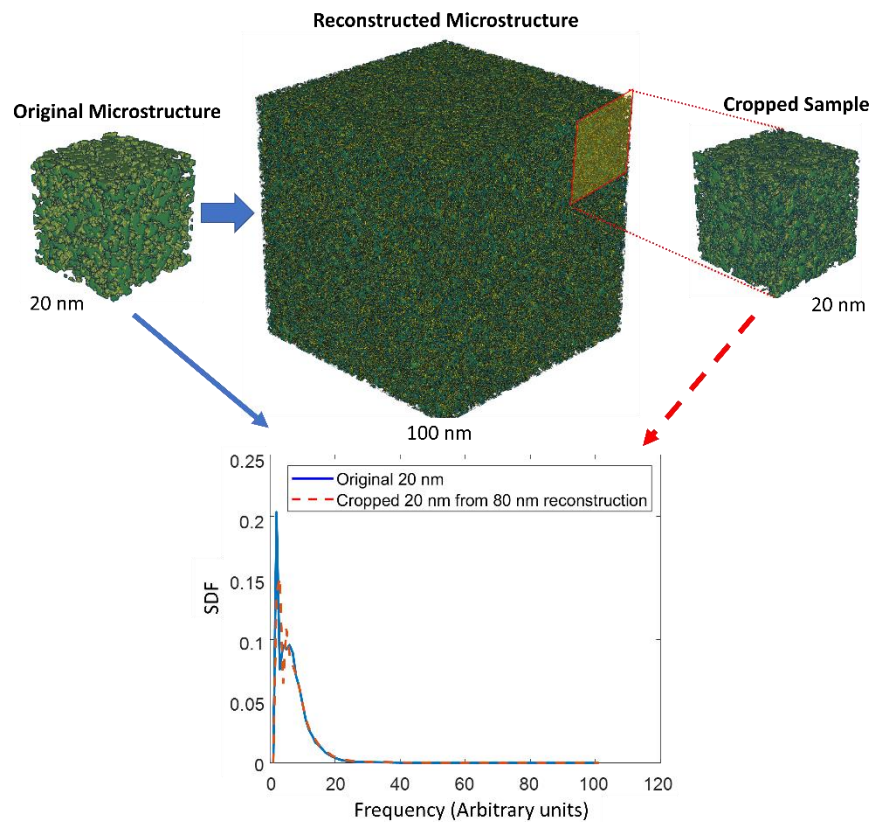


Figure 3-18: Top: Starting from a small 20 x 20 x 20 nm CGMD simulated microstructure, a large 80 x 80 x 80 nm is reconstructed using SDF frequency resolution enhancement. From the large reconstruction a smaller 20 x 20 x 20 nm sample is cropped for comparison. Bottom: SDF comparison of the original microstructure with cropped microstructure.

### 3.5 Multi-fidelity optimization for OPVC

Based on the SDF-based design framework (Section 3.3), we attempted to find the optimal processing conditions of a solar cell in the previous study [63]. However, using the high-fidelity simulations (i.e., 100 nm structures) directly, would be too computationally exhaustive. In this section, we address this challenge by introducing a three-stage multi-fidelity design scheme that includes the use of low-fidelity simulations (i.e., 20 nm structures) to improve tractability as well as high-fidelity simulations to improve computational accuracy.

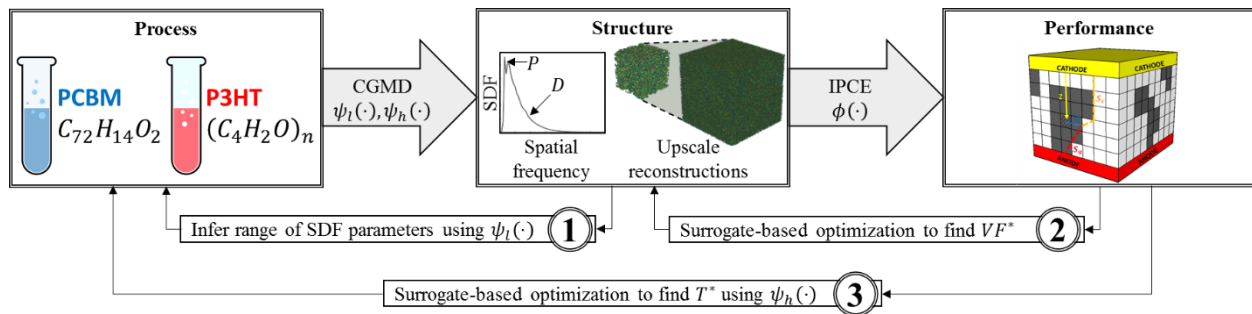


Figure 3-19: Three-step multi-fidelity optimization framework. The initialization of the optimization problem is to use the low-fidelity model to infer the range of intermediate structure parameters. Subsequently, in the next step, we find the optimal performance by maximizing the IPCE with respect to the volume fraction  $VF^*$  and the intermediate modeling parameters  $\{P, D\}$ . Finally, the optimal annealing temperature  $T^*$  is found by maximizing the entire PSP link using the high-fidelity model.

The PSP linkage as presented in **Figure 3-19** is an acyclic multimodal design problem [64] that contains three models: (1) low-fidelity process to structure model  $\{P, R, D\}^T = \psi_l(T, VF)$  where  $P, R$  and  $D$  are respectively the SDF peak point, relative high difference of the first two peaks, and decay parameters (Section 3.5.2.1), (2) high-fidelity process to structure model  $\{P, R, D\}^T = \psi_h(T, VF)$ , and (iii) structure to property model  $IPCE = \phi(P, D, VF)$ . Subsequently, by solving the optimization problem

$$\max_{T, VF \in \Omega} \phi(\psi_h(T, VF), VF), \quad (3-3)$$

for the domain  $\{T, VF\} \in [50, 170] \times [0.25, 0.75] = \Omega$ , a designer can identify the optimal processing settings. We infer this range by from literature;  $T$  usually varies between 50 °C and 170 °C in experiments. However, the range of  $VF$  in experiments is a bit narrow in the authors opinion, so a wider range is selected from 0.25 to 0.75 to search the unfamiliar design space. However, optimizing Equation 3-14 using evolutionary (e.g., genetic algorithm, simulated annealing, and particle swarm) or gradient-based methods (e.g., gradients descent, Newton’s methods, and sequential quadratic programming) is unpractical as they would require too many costly function evaluations. A computationally more efficient class of methods is Bayesian optimization, but for problems of this dimension even Bayesian optimization requires dozens of function evaluations in the case of homoscedastic noise [65] and hundreds in the case of heteroscedastic noise [43]. In our problem, we need to consider noise as the process to structure model (i.e., the CGMD simulation model) that has randomized initial conditions that are evaluated over a finite length and timescale.

*Table 3-1: Computational cost for individual CGMD simulations using low and high-fidelity approaches.*

	<b>Total wall time (hrs.)</b>	<b>Number of CPUs (cores)</b>	<b>Total core-hours</b>
Low fidelity (20 nm)	120	560	67,200
High fidelity (100 nm)	300	2800	840,000

To reduce the computational complexity, we make two observations: (i) the computational cost (core-hours) of the high-fidelity process to structure model is more than 12 (Table 3-1) times larger than the low-fidelity model and the structure to property model, and (ii) all simulations

modes share the composition input  $VF$ . Leveraging this insight, we propose the following three-step multi-fidelity inverse design scheme:

- 1) Identify the domain  $\omega$  of intermediate model variables  $P, R, D \in \omega$  (i.e., the range of the SDF peak parameter  $P$  and decay parameter  $D$ ) through a small set of samples obtained from the low-fidelity structure to property model  $\psi_l(\cdot)$ .
- 2) Identify the optimal composition  $VF^*$  by optimizing the structure to property model  $\phi(\cdot)$  using the domain of intermediate model variables  $\omega$ , as identified in Step 1.
- 3) Identify the optimal annealing temperature  $T^*$  by optimizing the high-fidelity linked process to structure to property model  $\phi(\psi_h(\cdot), \cdot)$  over a reduced dimensional design space.

Concerning the initial Step 1, we start by creating a design of experiments for the low-fidelity CGMD process to structure simulation  $\psi_l(T, VF)$ . Specifically, using an optimal Latin hypercube design [66] containing nine samples we uniformly cover the domain of processing settings  $\Omega$ . By evaluating these samples using the low-fidelity CGMD process to structure simulation we can identify the range of the intermediate modeling variables as  $P, R, D \in \omega \subset \mathbb{N} \times \mathbb{R}^2$ . Assuming that this range is representative for the intermediate modeling variables, we can identify the optimal composition  $VF^*$  and structure  $\{P^*, R^*, D^*\}^T$  (Step 1) as

$$VF^*, P^*, R^*, D^* = \underset{\substack{VF \in [0.3, 0.8] \\ P, R, D \in \omega}}{\operatorname{argmax}} \phi(P, R, D, VF). \quad (3-4)$$

With the optimal composition  $VF^*$  known we need to identify the optimal annealing temperature  $T^*$ . Originally, this would have been a costly procedure as it required the evaluation of the high-fidelity CGMD process to structure simulation at different levels of composition  $VF$

and annealing temperature  $T$  in the domain  $\Omega$ . However, by identifying the optimal composition using Equation 3-4, we can simplify the problem into a one-dimensional optimization (Step 2) as

$$T^* = \operatorname{argmax}_{T \in [50, 170]} \phi(\psi_h(T, VF^*), VF^*). \quad (3-5)$$

Optimizing Equation 3-5 will require fewer function evaluations than Equation 3-3 for two reasons: (i) the search space has been reduced from two to one dimension without changing the roughness of the objective function, and (ii) we only need to create one structure as an input to the high-fidelity CGMD structure to property simulation that we can evaluate at different temperatures  $T$ . Although we have significantly reduced the complexity of the optimization problem, the computational cost for evaluating  $\psi_h(\cdot)$  is still nontrivial, and so we use a set of nine high-fidelity processes to structure to property simulations, obtained from an optimal Latin hypercube design for  $T \in [50, 170]$ , to train a Gaussian process model  $\hat{f}(\cdot)$ . Consequently, by substitution of  $\hat{f}(\cdot)$  into Equation 3-5 we can find the optimal annealing temperature as

$$T^* = \operatorname{argmax}_{T \in [50, 170]} \hat{f}(T). \quad (3-6)$$

The validity of the three-step multi fidelity inverse design scheme introduced in this section depends on two implicit assumptions. First, by identifying the optimal structure (Step 1), we assume that all structures described by  $P, R, D \in \omega$  can be synthesized through processing settings in the domain  $\Omega$ . This decentralized approach greatly limits the computational cost but selecting a domain that is too small risks converging to a suboptimal design. In contrast, selecting a domain of intermediate modeling variables that is too large risks converging to a structure that cannot be synthesized from the admissible processing settings. Second, it is assumed that the domain of intermediate modeling parameters  $\omega$  is independent of composition  $VF$ . Specifically, when solving Equation 3-4, we assume that for any value of the composition  $VF$  there exists a structure

with any SDF parameters  $P, R, D$  in the domain  $\omega$ . Despite these limitations, the introduced three-step multi-fidelity inverse design scheme can identify the processing settings associated with strong properties through a manageable number of function evaluations.

### 3.5.1 CGMD Simulations

Due to the reduced number of total particles (coarse-grained interaction sites) relative to all-atom molecular dynamics, CGMD allows us to simulate larger systems ( $\sim 10$ - $1000$  nm each side) containing millions of beads (also known as superatom) for longer time scales ( $\sim 1$ - $10$   $\mu$ s) spanning millions of timesteps. Hence the investigation of morphological features based on different processing conditions such as the annealing temperature and volume fraction (weight ratio) is achievable using chemically informed CGMD simulations [67,68]. One can also investigate the trend in morphological evolution during the typical solvent evaporation and thermal annealing process to construct correlations between processing, structure, and performance. In this work, all the CGMD simulations are carried out using Gromacs molecular dynamics package [69], visualized using VMD [70], and post-processed in MATLAB.

#### 3.5.1.1 Multi-Fidelity Simulations

Low-fidelity CGMD simulations are employed to simulate the blend morphology formation and evolution within a smaller length scale ( $\sim 20$  nm each side). Organic semiconducting polymer Poly(3-hexyl-thiophene) (P3HT) in combination with phenyl-C61-butyric acid methyl ester (PCBM) are initially solvated in Chlorobenzene (CB) solution. Finer-than-traditional CG beads and the corresponding interatomic interactions, as described by Martini force fields [71], are considered to model P3HT, PCBM, and CB molecules. While larger domains simulated for a longer time scale (high-fidelity) can describe the morphology comparable to experiments,

performing these high-fidelity simulations would be arduous given the enormous amount of computational time that they require. Additionally, we believe that our low-fidelity simulations, as described in earlier efforts by Munshi et. al. [72,73], can unravel the fundamental physical trends in the microstructure evolution driven by the intermolecular interactions at finite temperature. That is why we believe they are sufficient for finding the representative microstructure features to extract the underlying SDF shape.

### 3.5.1.2 Large-Scale High-Fidelity Simulations

While the low-fidelity CGMD simulations are an excellent choice to extract microstructural features and provide fundamental insights into the trends in overall exciton diffusion to charge transport process, these are seldom comparable to the experimental characterization. To address this challenge, high-fidelity CGMD simulations are employed to mimic the physical experiments of OPVC design. Akin to the low-fidelity approach, P3HT and PCBM are initially solvated in organic CB solution. Following energy minimization and equilibration at constant temperature and pressure conditions (also referred to as the number of particles, pressure, and temperature (NPT) equilibration), CB molecules are evaporated gradually from the system to simulate a typical solvent evaporation process. Finally, the 100 *nm* thick solvent-free P3HT: PCBM bulk heterojunction nanomorphology is heated up to a specific temperature,  $T$  (thermal annealing) and gradually cooled down to room temperature ( $T = 25^{\circ}\text{C}$ ). For all these simulations, the  $x$  and  $y$ -dimension are kept constant at 100 *nm* while the  $z$ -direction (thickness) is initialized at  $\sim 800$  *nm* for the solvated ternary mixture. The final solvent-free and thermally annealed structure, in absence of the CB solvent molecules, reduce to the thickness of  $\sim 100$  *nm* leading to simulation box volume of  $\sim 100$   $\text{nm}^3$ . In contrast to the low-fidelity CGMD

simulations, large-scale simulations consider large number of interaction site thus making the high-fidelity simulations highly sensitive to the interaction parameters between the CG beads. To stabilize the large-scale systems and accurately capture the dynamics during evaporation and annealing process, we varied the Martini bead radius for the P3HT and PCBM molecules along with a subtle variation in the Lennard-Jones (LJ) cutoff distance implemented using Verlet scheme. While in our previous efforts for low-fidelity CGMD simulations [71], we found a LJ cutoff distance of 1.1 *nm* to achieve P3HT: PCBM system density in agreement with experiments, for the high-fidelity CGMD simulations a cutoff distance  $\sim 1.4$  nm was found to be optimum. The increase in the total number of interaction sites and the cutoff distance account for the large difference between the overall computational cost between the two variants of CGMD simulations. Finally, these large-scale high-fidelity simulations, in this work, are directly compared with experimental observations such as cross-sectional scanning tunneling microscope (X/STM) images to investigate microstructure evolution through solution processing techniques, such as spin coating, typically employed in experiments of OPVC design.

### 3.5.2 Results and Discussion

In this sub-section, we discuss the result obtained when we apply the design framework introduced in Section 2.2 to design an OPVC with optimal IPCE performance. First, we need to identify the range of SDF parameters estimated from a small number of low-fidelity CGMD simulations (Section 3.7.2.1). Next, we identify the optimal microstructure morphology by optimizing the structure to property model with respect to the SDF parameters and volume fraction (Section 3.7.2.2). Subsequently, we optimize the property with respect to the processing conditions using the high-fidelity CGMD model (Section 3.7.2.3). Lastly in Section 3.7.2.4 we conclude this

study by comparing the optimal processing conditions with experimental results reported in the literature.

### 3.5.2.1 Step 1: Inferring the range of SDF parameters

In beginning of Section 3.7 it was assumed that the SDF functions could be characterized by a two-dimensional parametric function. This approximate SDF function was established by observing the similarity between the SDF of the microstructures obtained from the nine low-fidelity CGMD simulations, as documented in

Table 3-2. Specifically, in **Figure 3-20A** we have plotted all nine normalized SDF functions (i.e., the area under the plots has been normalized to equal on). Note that we can normalize the SDF function as the reconstruction depends on the relative frequency of material features and not the absolute frequency. We extracted the salient features of the nine curves to match them with the properties (IPCE values), using the following approximation

$$\hat{\rho}(\kappa, D, R, P) = \begin{cases} 0, & \kappa = 0 \\ 1 - \frac{\kappa - 1}{3}, & 0 < \kappa < P \\ Re^{(-D(\kappa - P))}, & P \leq \kappa \end{cases} \quad (3-7)$$

where  $D$  is the frequency of the second peak,  $R$  is the ratio between the first and second peak, and  $D$  is a variable to governs the decay of the SDF at higher frequencies. Note that the lower frequencies contain the largest degree of inconsistency when compared with the target structure in Figure 5A. However, we believe that this noise influences the IPCE of the reconstructed microstructures only marginally. The reason that the low frequency has limited influence on the IPCE is that they are associated with features that have a long length scale and less samples, and hence are more prone to noise and are less consequential to the microstructure morphology. It is for this reason that the exponential decay term of the parametrized SDF  $\rho(\cdot)$  captures the most

important features. In Figure 3-20B we have plotted the SDF of one low-fidelity CGMD structure (blue function) and shown that we can get a good fit with the approximate SDF (red dashed function). Note that in this plot we have normalized the plot to show its consistency with the experimental structure. Moreover, minimizing the mean squared error for each of the nine low-fidelity CGMD structures we can find the  $P$ ,  $R$  and  $D$  parameters as shown in fourth, fifth and sixth column of

Table 3-2. Using these intermediate modeling parameters, we reconstructed the initial nine low-fidelity structures and simulated their IPCE property. Subsequently, we calculated the relative error with respect to the IPCE values of the target microstructure responses as shown in the ninth column of Table 2. The maximum observed relative error is  $<3\%$  and as such we can conclude that the parametrized SDF provides an accurate approximation of the microstructures.

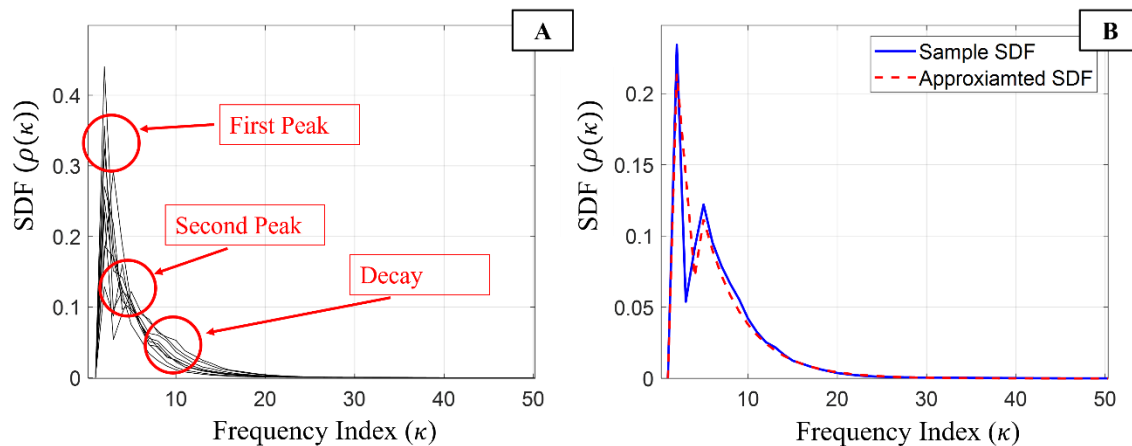


Figure 3-20: Parametrization of the SDF of low-fidelity CGMD microstructures. The SDF of the nine microstructures obtained from low fidelity CGMD simulations (Figure 8A) shows a remarkable consistency among the microstructures. Subsequently, this similarity can be captured through a parametric function that can be used to approximate the original SDFs (Figure 8B).

Table 3-2: Design of experiments used to explore the potential microstructures using the low-fidelity CGMD simulation model.

#	Process		Structure			Property		Relative error (%)
	$VF$	$T$ (°C)	$P$	$R$	$D$	$\phi(\psi_l(T, VF), VF)$	$\phi(P, R, D, VF)$	
1	0.375	50	5	0.522	0.217	0.3558	0.3649	2.56
2	0.5625	65	4	0.337	0.244	0.3333	0.3379	1.38
3	0.625	170	5	0.385	0.295	0.3133	0.3216	2.65
4	0.25	140	4	1.245	0.224	0.3403	0.3481	2.29
5	0.6875	125	3	1.332	0.321	0.2863	0.2909	1.61
6	0.4375	155	4	0.675	0.213	0.3531	0.3584	1.50
7	0.3125	95	4	0.344	0.259	0.3512	0.3563	1.45
8	0.5	110	4	0.564	0.276	0.3446	0.3494	1.39
9	0.75	80	4	0.271	0.402	0.2543	0.2591	1.89

### 3.5.2.2 Step 2: Structure-Property Optimization

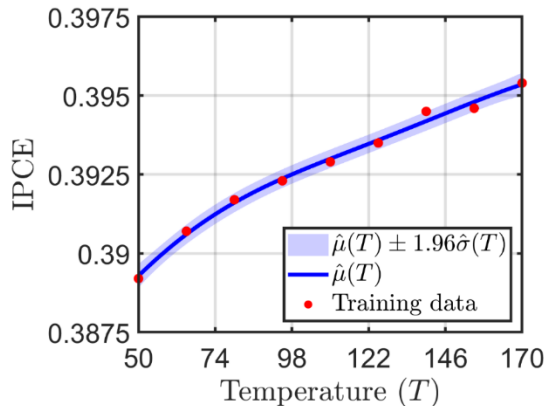
To find the optimal microstructure using Equation 3, we need to identify the range of intermediate modeling parameters  $\omega$ . From the fourth, fifth and sixth column in Table 2 we can infer the range for the intermediate modeling parameters by expanding the design space from the original samples as  $P, R, D \in [3, 5] \times [0.271, 1.332] \times [0.213, 0.402] = \omega$ . Specifically, the second index of peak frequency variable in the SDF is a natural number in the range  $P \in [3, 5]$ , the exponential decay variable in the SDF is a real number in the range  $D \in [0.213, 0.402]$ , and the ratio between the first and second peak is a real number in the range  $R \in [0.271, 1.332]$ . Using the range of the intermediate modeling parameters  $\omega$  we can optimize Equation 3, to find the optimal microstructure. Before optimization, we first need to increase the sample size to make it

comparable to experiments. The typical thickness of spin coated OPVC is of 200 nm, so we use the SDF frequency enhancement (Section 3.6) to increase the size of the smaller samples 10<sup>3</sup>-fold.

While the SDF improves the efficiency of the microstructure reconstruction, the computational cost for evaluating the IPCE is still not trivial. Consequently, we use a surrogate-based optimization framework by training a Gaussian process model on a set of 30 IPCE function evaluations assigned through an optimal Latin hypercube design. Subsequently, using a multi-start sequential quadratic programming optimization approach we find the optimal microstructure as  $\{VF^*, P^*, R^*, D^*\} = \{0.4, 5, 1.33, 0.213\}^T$ , for which the Gaussian process model predicts an optimal IPCE value of 0.195. To validate these results, we reconstructed a new microstructure using the optimal microstructure parameters and find an optimal IPCE value of 0.189. Compared with the Gaussian process model prediction, we have a relative error of <0.4%, and thus we can conclude that the Gaussian process is sufficiently accurate to approximate the globally optimal microstructure.

### 3.5.2.3 Step 3: Process-Structure-Property Optimization

Using the optimal volume fraction  $VF^*$ , we can identify the remaining optimal processing condition by optimizing the high-fidelity CGMD simulations with respect to a reduced



dimensional design space. Specifically, we can use a surrogate model-based optimization approach by training a Gaussian process model on nine equally spaced annealing temperatures and the predicted IPCE values. It should be noted that this means we train a surrogate model to directly predict the IPCE value as a function of the processing conditions. In addition, to run the low-fidelity CGMD simulations we set the volume fraction at  $VF^* = 0.4$  as identified in Step 1. The resulting Gaussian process model predictions are shown in **Figure 3-21**. The motivation for using a Gaussian process model is that it enables us to account for the prediction uncertainty in the CGMD simulations. Specifically, this can be observed in **Figure 3-21** from the nonzero prediction uncertainty (blue shaded regions) at the observed training samples. The advantage of Gaussian process over other deep learning methods is its Bayesian assumption on the space of potential functions that provides a statistically rigorous approach to avoid over fitting or underfitting the data.

*Figure 3-21: Gaussian process model prediction for the IPCE as a function of temperature. The high-fidelity CGMD simulations used the optimal volume fraction  $VF^* = 0.40$  as identified in Step 1 of the introduced design framework.*

From the response surface approximation shown in Figure 9, we can observe that the globally optimal IPCE value is found at an annealing temperature of  $T^* = 170^\circ\text{C}$ . In addition, the optimal IPCE value for the identified optimal processing conditions is  $IPCE^* = 0.3953$ . It should be noted that the optimal IPCE value is higher than what was predicted with the low-fidelity model. This is likely a result of the difference in the size of the simulated structures (100 nm, and 200 nm), as thinner structures are expected to trap the light more effectively. Since we are interested in the trend rather than the exact value of IPCE for optimization, it is less consequential. Nevertheless, the introduced three-step multi-fidelity design framework facilitates microstructure

sensitive design using previously intractable models. Because, because the globally optimal IPCE was found at an already simulated annealing temperature we do not need further validation. Lastly, the SDF parameters ( $P^* = 4, D^* = 0.36, R^* = 0.33$ ) of the optimal CGMD simulation are also well within the design space  $\omega$ . This is evidence of the efficacy of step 1 where smaller CGMD simulations were used to extract the range of SDF parameters.

#### 3.5.2.4 Validation of results

To validate the findings of the introduced three-step multi-fidelity design framework we compare the optimal processing conditions (i.e.,  $T^*$  and  $VF^*$ ) with those reported in the experimental literature. First, we note that the identified optimal volume fraction  $VF^* = 0.4$  is relatively similar to 0.8:1 PCBM:P3HT (0.38) loading as reported in [74]. Concerning the annealing temperature, comparison to literature is more difficult as reported values range from 140 to 160 degrees Celsius [75,76]. While this matches relatively well with the optimal annealing temperature in this study (i.e.,  $T = 170^\circ\text{C}$ ), additional investigation is warranted. From a modeling perspective, this difference could come from three reasons (i) a systematic model bias because of the inherent assumptions in the CGMD model, (ii) the Voronoi tessellation approximation that represents the PCBM and P3HT molecules as irregular polyhedral, or (iii) the inherent assumptions in the IPCE model. In contrast, we can also note from comparing the results presented in the seventh column of Table 2 with the high-fidelity observations plotted in Figure 9, that annealing temperature has only a small influence on the IPCE compared to the volume fraction. This could explain why multiple optimal values for the annealing temperature have been reported in the literature, as observations would become more sensitive to experimental noise. Nevertheless, the

presented CGMD is highly consistent with the experimental observations and as such provides designers with a reliable OPVC design tool.

To validate the efficiency of the three-step multi-fidelity design framework we compared the computational cost. In the presented study we used nine low-fidelity and nine high-fidelity simulations. Evaluating the low-fidelity simulations and the high-fidelity simulations required approximately 120 hours and 300 hours, respectively. Comparing this with two hypothetical scenarios: (A) the same study using only high-fidelity simulations, and (B) using Bayesian optimization for stochastic functions [43] in conjunction with the high-fidelity model.

(A) Doing high-fidelity simulations to identify the range of the intermediate modeling parameters requires function evaluations for different values of  $VF$  and  $T$ . Evaluating the high-fidelity response for the same design of experiments would have taken approximately nine times more core hours as seen in Table 1. While this would have improved the accuracy of the identified intermediate modeling parameters, its influence on the identified range would have been marginal. In addition, it would not have been enough to train an accurate surrogate model and find the optimal processing conditions directly.

(B) Our previous study required 305 simulations at 46 unique volume fractions. Assuming that both length-scales behave similarly resulting in same number of simulation requirements, we can calculate the total time to be greater than 91000 ( $300 \times 305$ ) hours using low-fidelity simulations compared to approximately 3780 ( $120 \times 9 + 300 \times 9$ ) hours for this study.

The substantial difference in cost not only provides practical validation for the efficiency of the introduced approach but also shows how information about a material's microstructure can

be leveraged to expedite the design process. Note that in the above comparison we did not consider the cost of the IPCE model as it only a fraction of the simulation cost and is therefore inconsequential to the stated conclusions.

### 3.5.3 Optimization-study conclusion

In this section, we presented a coarse-grained molecular dynamic (CGMD) based three-step multi-fidelity design framework for the design of an organic photovoltaic cell (OPVC) that has optimal performance with respect to acceptable processing conditions. The contributions of the presented work are: (i) simulating large-scale ( $100 \times 100 \times 100 \text{ nm}^3$ ) high-fidelity simulation whose performance predictions conform with experimental length and time-scales (ii) we introduced a multi-fidelity design framework that enables design of an OPVC with respect to its processing conditions at a predictive fidelity that was previously intractable with CGMD simulations, and (iii) we used an SDF frequency-enhancement technique to reconstruct large samples from smaller ones. The introduced design framework reduces the computational complexity by using low-fidelity CGMD simulations to gain insight into the potential microstructures that can be achieved from admissible processing conditions. Consequently, we leverage this insight to reduce the input dimensionality of the high-fidelity CGMD simulations by finding the optimal microstructure using the relatively faster structure to performance model. Reducing the input dimensionality of the high-fidelity model facilitates the identification of the optimal processing conditions with significantly fewer costly high-fidelity CGMD function evaluations.

The introduced design framework can be employed for other microstructure design applications when the following four assumptions are valid: (i) the process to structure model and the structure to performance model have shared design variables, i.e., volume fraction of the OPVC compositions (ii) the structure to performance model is much faster to evaluate than the process to structure model, (iii) the microstructure features can be accurately characterized through their spectral density function (SDF), and (iv), the range of the SDF parameters used to characterize the microstructures are independent of the design variables shared by the PS and SP models. The authors believe that (iv) is the most limiting assumption which can be accounted for by establishing the underlying relationship between the parameters and design variables by performing more simulations in the next step of this study.

### 3.6 Summary

In this chapter, the SDF curve is studied to improve its understanding so that it can be more effectively applied in design of materials. Next, we introduce an SDF-based design framework which can be used for the design of a quasi-random microstructure system. Using this framework, we aim to optimize an organic photovoltaic cell (OPVC).

But since the experimentation of the solar cell is very computationally expensive, it inhibits the use of this framework. This restriction led to another novel contribution in the use of SDF , i.e., SDF-frequency enhancement which allows us to take SDF from a relatively smaller sample and yet reconstruct much larger samples. Leveraging this capability, we introduce a three-step multi-fidelity design framework that enables a designer to efficiently explore the space of admissible processing conditions, using coarse-grained molecular dynamics (CGMD) simulations, to identify the optimal OPVC design. Using the material characterization and a novel multi-scale

reconstruction capability of spectral density function, the framework enables the sequential optimization of the microstructure using a low-fidelity CGMD simulation with a smaller window size, followed by the optimization of the processing conditions using the high-fidelity simulation. The division in two steps and two fidelities enables the optimization of CGMD simulations at previously intractable lengths and timescales. We validate our results by demonstrating that the CGMD model predictions are consistent with physical experiments reported in the literature and corroborate that the computational complexity is reduced by one order of magnitude.

In this chapter our focus was on quasi-random material systems. Another microstructural material system is that of alloys which could be called granular. The microstructure consists of grains that have varying sizes, orientations, and phases. It encapsulates a much higher dimension information than quasi-random material systems, and thus, SDF is not sufficient to sufficiently characterize it. In the next chapter we discuss a different characterization technique that can help in analyzing and designing such material systems.

## Chapter 4 Characterization and Design of Granular Microstructures in Additive Manufacturing Systems

### 4.1 Introduction

Additive manufacturing (AM) is a break-through technology that has the potential to completely change the landscape of manufacturing science and technology by enabling the production of near-net shape and intricate geometries. However, as an emerging technology, AM of metals and metallic alloys has many barriers to overcome to be fully implemented in large scale manufacturing. One of the main challenges in metal AM is the same as any other manufacturing process which is to establish the process-structure-property (P-S-P) relationship. Building this relationship can help save a lot of time for material exploration compared to the Edisonian approach. A strong stochastic nature of the produced parts with AM is one such bottleneck. This is attributed to the varying microstructure. This variability in microstructure is attributed to complex multi-physics and multiscale nature of the AM process. To make the AM process useful, researchers have been trying to come up with methodologies that can characterize these variabilities in model validation and model prediction to explore the vast design space. Once the material variability is better captured, it can be used to build a more accurate P-S-P model.

Since AM experiments are time-consuming and expensive, numerical models to predict microstructure formation are good alternatives to enhance the study of process-structure correlation. There are several numerical models of microstructure prediction, such as the phase-field method (PFM) [77,78], the cellular automaton (CA) model [79–81], and the kinetic Monte Carlo method (KMC) [37]. Among them, the PFM is a diffuse interface model defined by a system

of partial differential equations, which are applied to predict dendrite structure and grain growth [82]. However, the small length scale of dendrites and grains limits the ability of the PFM to predict microstructure in meso-scale efficiently. The CA model simulates grain nucleation stochastically, which requires less computational expense compared with PFM and achieves good accuracy [80]. Unlike KMC, the CA model includes a physically meaningful time step, which is easier to interpret the predictions and couple with the thermal models [80,83]. All these models require calibration in order for them to be meaningful, and currently the calibration process is not automated.

We dedicate this chapter to explore and enhance microstructure characterization techniques to (i) build predictive P-S-P models, and (ii) to automate the calibration process of CA simulation models.

## 4.2 Granular Microstructure Characterization and Dissimilarity Score

### 4.2.1 Chord Length Distribution (CLD)

For metals, grain sizes and morphology are directly linked to mechanical and physical properties [7][6]. Thus, it is important to be able to characterize the grain features in order to understand their effects on properties. Instead of using equivalent spherical diameter (which approximates the size of the grain) and grain statistics (which include distribution of grain sizes and texture), we select angularly resolved chord length distribution (ARCLD) [16] to statistically characterize the microstructures. ARCLD is an extension of Chord Length Distribution (CLD), which is essentially the probability of finding chords of specified lengths in the microstructure. CLD is calculated by throwing horizontal lines in the microstructure, finding the grain boundaries intersection with the line, and then calculating the distances between two consecutive intersections.

ARCLD builds upon this approach by varying the angles of the lines to be thrown inside the microstructure [16]. Compared to the aforementioned grain descriptors, the main advantages of using ARCLD for characterizing microstructures include (1) generic application regardless of the shape of grains, (2) the measure provides directional information, and (3) ARCLD has established relationship with plastic[84] and transport properties [85] for heterogeneous materials.

In this proposed methodology, instead of calculating ARCLD for 360 degrees as in Latypov *et al* [16], we limit our calculation to four selective angles. This approach resembles that of Talukdar *et al* [86] who uses CLD only at four angles to guide the microstructure reconstruction process. Furthermore, to cater for the local noise, we calculate the CLD for five consecutive angles and average them as:

$$CLD_{\theta} = \frac{1}{5} (cld_{\theta} + cld_{\theta+1} + cld_{\theta+2} + cld_{\theta+3} + cld_{\theta+4}), \quad (4-1)$$

Where  $\mathbf{cld}_{\theta}$  is the chord length distribution at angle  $\theta$ .

Because of symmetry, we calculate  $CLD_{\theta}$  for the following four representative angles, i.e.  $0^{\circ}$ ,  $30^{\circ}$ ,  $60^{\circ}$ , and  $90^{\circ}$ . Thus, for every image, four CLDs are calculated as seen in Figure 4-1 which is presented as an example.

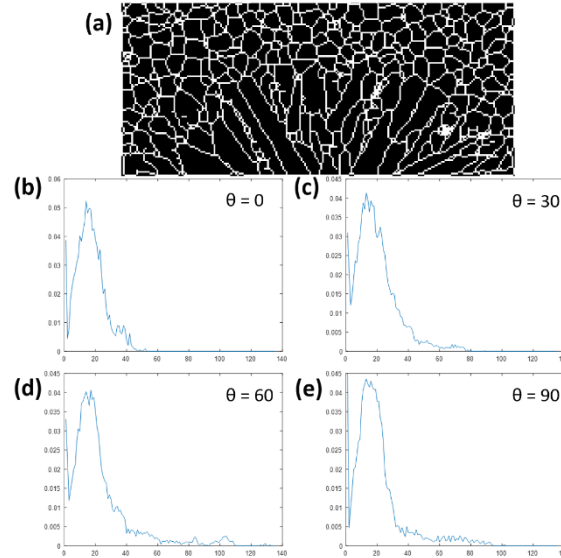


Figure 4-1: The microstructure on top (a) is simulated using CA model. The bottom four curves (b-e) are the CLDs at the four representative angles. The x-axis is the length of chord and y-axis is the probability.

The method presented up until now was only for 2D images. We calculate the ARCLD of a 3D image by averaging the ARCLD of all sliced 2D images for a particular angle:

$$CLD_{\theta}^{avg} = \frac{1}{N} \sum_{i=1}^N CLD_{\theta}^i, \quad (4-2)$$

where  $CLD_{\theta}^i$  is the  $CLD_{\theta}$  for plane  $i$ , and  $N$  is the number of planes.

#### 4.2.2 Microstructure Difference Quantification using Dissimilarity Score (DS)

Many computational frameworks have been proposed [5,87] to model process-structure-property-performance in AM. However, computational methods face the challenge of accurately predicting the microstructures for any giving process parameters. Among the several methods that have been developed to predict grain growth [5,32,87], the Cellular Automaton (CA) method offers a good compromise between computational expense and desired accuracy[34]. However, validation of simulated microstructure against experimental microstructure is a challenging task.

So far, researchers have done this validation qualitatively [38], however, a quantitative metric is more desirable. Specially, the candidate microstructures in question may vary locally while being statistically similar on a larger scale. On the other hand, without a proper numerical measure, it is hard to gauge how accurate the parameters of the model are and how those parameters can be improved so that the model becomes more reliable.

The overarching goal of this section is to propose a validation metric, termed “Dissimilarity Score” (DS), to measure the differences of stochastic features between two microstructures, obtained from either a computer simulation or a physical experiment. In this work, we show that our proposed metric can distinguish between dissimilar (in both statistical and physical sense) microstructures and identify similar ones. We also apply this feature to test how accurate the microstructures generated from computational method (CA) is when compared to actual Electron Backscatter Diffraction (EBSD) data of real AM microstructure. Characterization of grain structures using the Angularly Resolved Chord Length Distribution (ARCLD) and the use of Earth Mover’s Distance (EMD) as the metric of Dissimilarity provide a novel approach for improving the computational modeling of AM.

Once ARCLD is calculated, which can be considered a distribution, the next step is to quantify the difference between different ARCLDs. Three popular methods of differentiating between distributions are Manhattan Distance (MD) [88], Kullback-Leibler divergence (DKL) [89], and Earth Movers Distance (EMD) [90]. MD is defined as:

$$MD(P, Q) = \sum |P(i) - Q(i)|, \quad (4-3)$$

where P and Q are two different distributions. The limitation with MD is that it is not able to do a *cross-bin* comparison. In a *cross-bin* comparison, neighboring bins are also accounted for

while calculating the difference between distributions. We present an example in Figure 4-2 to visualize this limitation. Consider the distributions  $x$ ,  $y$  and  $z$  represent the number of points in a class of 19 students. The average points of these distributions would be 1.95, 2.32, and 3.05 for  $x$ ,  $y$  and  $z$  respectively. Thus, the difference in the scores between  $x$  and  $y$  (Figure 2-1A) is much less than between  $x$  and  $z$  (Figure 2-1B). This subtlety is not captured by MD and that results in:  $MD(x, y) = MD(x, z)$ . On the other hand, since EMD considers cross-bin comparison, it is observed that EMD gives a higher figure between  $x$  and  $z$ . This cross-bin comparison is highly desired in our difference metric because the bins in ARCLD are associated with physical similarities in the microstructure.

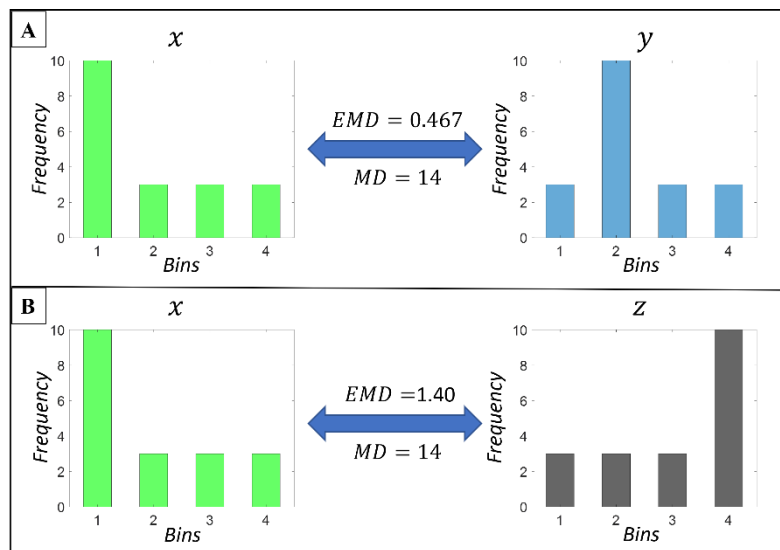


Figure 4-2: Quantifying difference between two set of distributions using EMD and MD. (A) Difference between distribution  $x$  and  $y$ . (B) Difference between distribution  $x$  and  $z$ .

The next metric, DKL is defined as:

$$DKL(P, Q) = \sum_{x \in X} P(x) \log \left( \frac{P(x)}{Q(x)} \right). \quad (4-4)$$

The critical limitation of using DLK is that it is not symmetric i.e.,  $DKL(x, y) \neq DKL(y, x)$ . Whereas, for a difference metric operating on microstructures this cannot be the case because the difference between two microstructures should be the same no matter which one is taken as a standard. EMD however is symmetric and capable of cross-bin comparison as well, and therefore it is the preferred choice in this study. EMD is based on a solution to the well-known *transportation problem* [91]. Suppose that several *trucks*, each with a given amount of earth, are required to fill several *holes*, each with a given limited capacity. For each truck-hole pair, the cost of transporting a single unit of earth is given. The transportation problem is then to find a least-expensive flow of earth from the trucks to the holes that fulfils the demand. EMD [90] can be defined as follows:

$$EMD(P, Q) = \min_{F=\{f_{ij}\}} \frac{\sum_{i,j} f_{ij} d_{ij}}{\sum_{i,j} f_{ij}}. \quad (4-5)$$

Subject to:

$$f_{ij} \geq 0 \quad (4-6)$$

$$\sum_j f_{ij} \leq p_i \quad (4-7)$$

$$\sum_i f_{ij} \leq q_j \quad (4-8)$$

$$\sum_{i,j} f_{ij} = \min \left\{ \sum_i p_i, \sum_j q_j \right\}, \quad (4-9)$$

where  $f_{ij}$  denotes a set of flows. Each flow  $f_{ij}$  represents the amount transported from the  $i$ -th supply to the  $j$ -th demand.  $p_i$  and  $q_j$  are locations of the supply and demand. We call  $d_{ij}$  the ground distance between the locations  $p_i$  and  $q_j$ . Constraint (4-6) ensures that supplies can only be moved from  $P$  to  $Q$ . Constraint (4-7) and (4-8), respectively, limits the amount of supplies that can be sent by  $P$ , and can be received by  $Q$ . Lastly, constraint (4-9) forces to move the maximum amount of supplies possible. We call this amount the total flow. Once the transportation problem is solved, and we have found the optimal flow  $F^*$ , the earth mover's distance is defined as the resulting work normalized by the total flow (Equation 4-5). Since  $f_{ij}$  and  $d_{ij}$  are calculated for all  $i$  and  $j$ , this results in all cross-combinations of the positions, and it thus makes EMD a cross-bin comparison. Interchanging the probabilities does not affect the formulation which makes this metric symmetric.

#### 4.2.2.1 Formula for Dissimilarity Score (DS)

To cut down on the computational cost and complexity we limit the ARCLD calculation to only four representative angles instead of the entire 360 degrees spectrum. But to accommodate for the local noise, for every angle position, the CLD is computed for the nearest five consecutive angles and averaged (Figure 4-3A):

$$CLD_{\theta} = \frac{1}{5}(cld_{\theta} + cld_{\theta+1^{\circ}} + cld_{\theta+2^{\circ}} + cld_{\theta+3^{\circ}} + cld_{\theta+4^{\circ}}), \quad (4-10)$$

where  $cld_{\theta}$  is the chord length distribution at angle  $\theta$ . Thus,  $CLD_{\theta}$  becomes the averaged chord length distribution for the consecutive five angles starting from  $\theta$ .

Because of symmetry, we only calculate  $CLD_{\theta}$  for four representative angles i.e.,  $0^{\circ}$ ,  $30^{\circ}$ ,  $60^{\circ}$ , and  $90^{\circ}$ . Thus, for every image, four CLDs are calculated as seen in Figure 4-3 which is presented as an example.

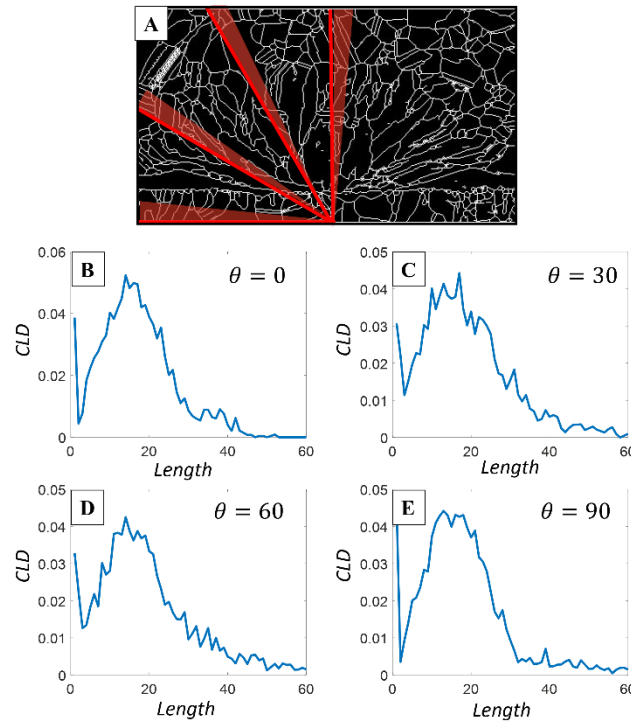


Figure 4-3: The microstructure on top (A) is simulated using CA model. The bottom four curves (B-E) are the CLDs at the four representative angles. The x-axis is the length of chord and y-axis is the probability.

The method presented up till now was only for 2D images. We calculate the ARCLD of a 3D image/simulation by averaging the ARCLD of all sliced 2D images for a particular angle:

$$CLD_{\theta}^{avg} = \frac{1}{N} \sum_{i=1}^N CLD_{\theta}^i, \quad (4-11)$$

where  $CLD_{\theta}^i$  is the  $CLD_{\theta}$  for a cross-section  $i$ , and  $N$  is the number of cross-sections of the 3D simulation. Since experiments are 2D, this does not apply to them.

Applying the EMD approach to our problem, we compute the Dissimilarity Score (DS) of two grain structures (Sample 1 and Sample 2) as:

$$DS(\text{Sample 1}, \text{Sample 2}) = \frac{1}{4} \sum EMD(CL D1_{\theta}^{avg} - CL D2_{\theta}^{avg}), \quad (4-12)$$

where  $\theta = 0^{\circ}, 30^{\circ}, 60^{\circ},$  and  $90^{\circ}$ , and  $CL D1_{\theta}^{avg}$  and  $CL D2_{\theta}^{avg}$  are the average  $CLD_{\theta}$  for two different samples/microstructures at a particular angle  $\theta$ .

#### 4.2.2.2 Comparison of synthetic microstructures created from Dream 3D

To show the effectiveness of the DS, we apply it on a synthetic granular microstructure simulated in Dream 3D. By varying the mean and variance of a grain distribution, we create two different sets of microstructures to test the effectiveness of our proposed metric. The first test composed of two statistically equivalent microstructures simulated using the same grain distribution (Case 1 and Case 2 in **Figure 4-4A**). The second set consisted of two different microstructures simulated using different grain distribution parameters (Case 3 and Case 4 in **Figure 4-4B**). DS is computed between the two sets of microstructures, and the results (see **Table 4-1**) show that the DS between two similar microstructures is two orders of magnitude smaller than the DS between two different microstructures. Hence, we conclude that the metric successfully quantifies the difference between grain microstructures.

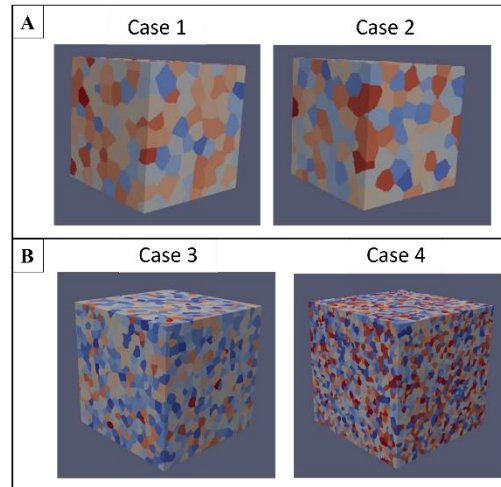


Figure 4-4: Artificial microstructure generated by Dream 3D. (A): Pair of statistically similar microstructures created from same set of input parameters. (B): Pair of statistically different microstructures created from two different sets of input parameters.

Table 4-1: DS calculated between similar microstructures (Case 3 and Case 4) and different microstructures (Case 1 and Case 2).

Dissimilarity Score (DS)	
Different Microstructures	Similar Microstructures
4.74	0.04

#### 4.2.2.3 Comparing Microstructure from different Additive Manufacturing simulation inputs

Next, the methodology was applied to distinguish between the two AM simulations (**Figure 4-5 B**) with different input process parameters. The simulation is the single laser track on Inconel 625 bare substrates. The microstructures were generated by CA solidification model coupled with thermal CFD model. For case A, the laser power is 150w, scan speed is 400 mm/s; for case B, the laser power is 195w, scan speed is 800 mm/s.

The DS score calculated between these two cases is 1.46. This score is relatively high, and thus indicative of the fact that the two microstructures are quite different.

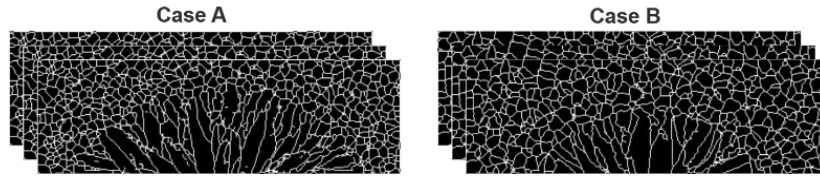


Figure 4-5: Multiple slices of two cases that were simulated using the CA code. Instead of the 3D volume, slices are shown to represent how the ARCLD is computed i.e. plane by plane.

### 4.3 Building P-S-P modeling using Machine Learning

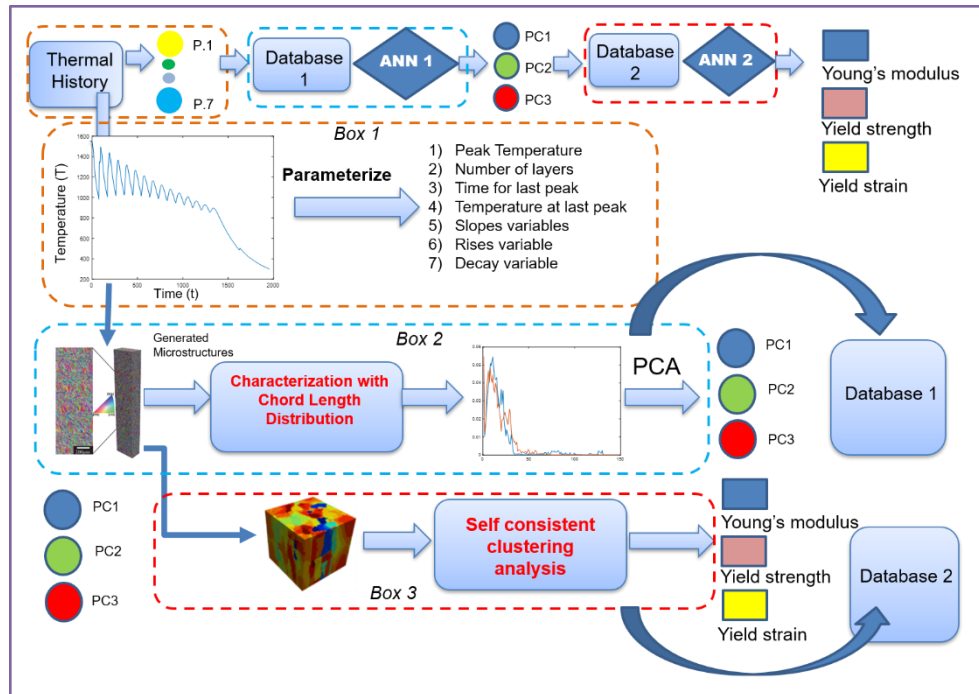


Figure 4-6: Framework for P-S-P modeling of AM

Based on the proposed microstructure characterization metric, a P-S-P framework (**Figure 4-6**) for material design is formulated, and the relationships between P-S-P in AM are explored. The first step is to use the coupling of Thermal CFD-CA-SCA [92] methods to generate a large simulation database for multi-layer parts build of powder bed fusion AM process with varied

process parameters (for example, laser power and laser scan speed). The simulation database includes thermal history, microstructure, final properties and performance (for example yield stress and ultimate strengths). From process to microstructure, a new parameterized form of thermal history is proposed to represent thermal history with different process parameters and locations in parts. The simulated microstructures are represented by the proposed microstructure characterization metric (Section 4.2.1). A neural network can be trained to find relationship between process and microstructure with thermal history parameters as the inputs and microstructure characterization metric as the output. From structure to property, neural networks will be used to link microstructure characterization metrics with simulated material property. In the end, the P-S-P framework for material design will be established and we will be able to observe how different thermal history influence microstructure and then the final properties and performance.

#### 4.3.1 Creating the dataset

For database generation, 4 multi-layer powder bed depositions with different laser power and laser scan speed were simulated for material In625. Each simulation is called a ‘case’. For each case, there are 10 layers of deposition and a single track for each layer. The details for each case are shown in the Table 4-2. Temperature field, microstructure, and mechanical properties such as young’s modulus and yield strength were predicted for each case by our models. The sampling scheme is also illustrated in Figure 4-7.

Table 4-2: Experimental details of the four builds.

Case	Laser power (W)	Laser speed (mm/s)	Layers	Layer thickness (mm)	Total tracks in each layer	Total domain for microstructure (mm)
1	300	1230	10	0.04	5 mm x 1	[0.99,0.165,0.446]
2	300	1529	10	0.04	5 mm x 1	[0.99,0.165,0.446]
3	241	1529	10	0.04	5 mm x 1	[0.99,0.165,0.446]
4	241	1230	10	0.04	5 mm x 1	[0.99,0.165,0.446]

The thermal-CFD model was used to predict thermal history for the thin wall. The thermal-CFD model was calibrated using a Proper Generalized Decomposition (PGD) method against the experiment data from Air Force Research Laboratory (AFRL). To calibrate a CA model using experiments, the substrate grains were first calibrated so that the solidification model was performed based on the accurate grain substrate (as mentioned in Section 4.3.1). In order to calculate the mechanical response using Direct Fourier Transform (DFT) at different points on thin wall, representative volume element analysis was selected. We used the experimental data from

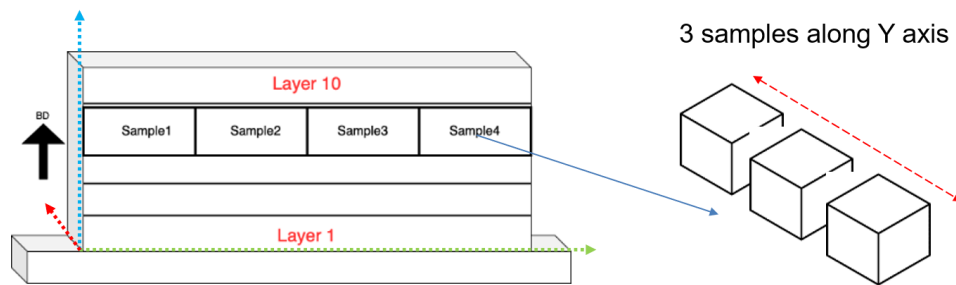


Figure 4-7: Sampling scheme for RVEs. In each layer 12 samples are taken with 4 varying x-axis locations and 3 varying y-axis locations.

Air Force Research Laboratory Additive Manufacturing Challenge 3 and 4 for Inconel 625 to calibrate the material law.

#### 4.3.2 Parameterizing the temperature history

After observing the thermal history data, the temperature parameterization technique was revised to include a new set of parameters which are as follows:

- 1) Peak Temperature
- 2) Lowest Temperature
- 3) First Decay Variable
- 4) Number of Peaks
- 5) Mean Heat Gap
- 6) Relative Peak Variable 1
- 7) Relative Peak Variable 2
- 8) Relative Peak Variable 3
- 9) Relative Peak Variable 4

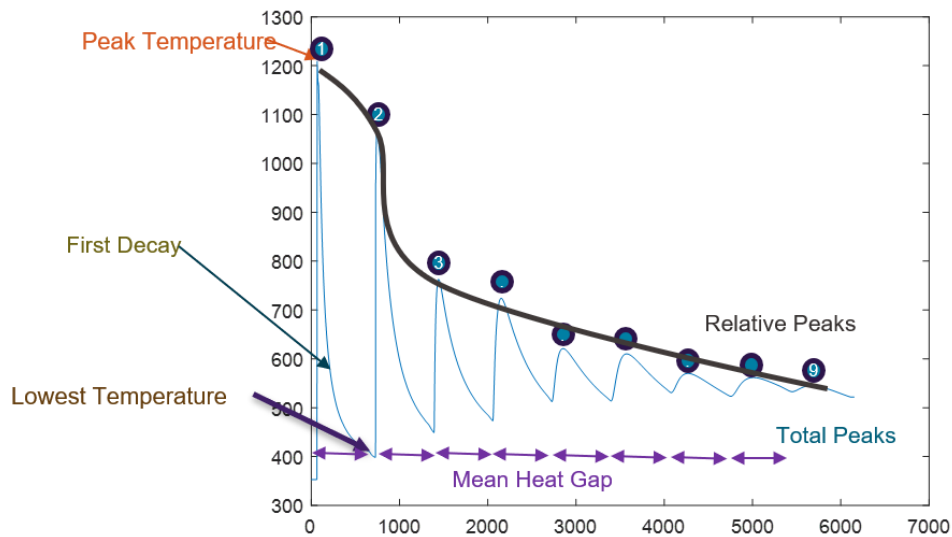
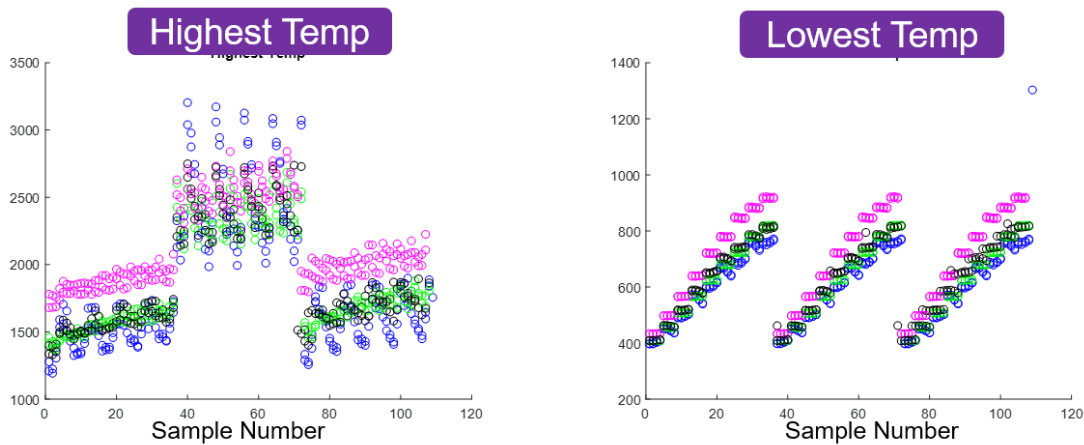


Figure 4-8: Visual explanation of the thermal history parameters.

The thermal history data was analyzed for all the 960 samples. When parameterization was applied, it did not work for the data points located on the top layer of the wall because those data points only had one peak. For that reason, only three out of the nine parameters were calculated, and others were not applicable (NA). To solve this issue, we removed these erroneous data points. From the entire set of 960 data points, we were left with 856. The remaining data points were parameterized and were then analyzed. The first analysis we conducted was to list the highest temperature from all the data points (Figure 4-9).



*Figure 4-9: Highest and lowest temperature scatter plot of all the data points. The x-axis sample number represents sample number of each case/wall.*

As can be seen in Figure 4-9, there are three distinct clusters based on the location along the y-direction. The cluster in the middle with the highest temperature corresponds to the sample taken at the middle of the wall. Next, looking at the **Figure 4-10**, we observe nine different clusters corresponding to the nine locations of the sample in the build direction i.e. one sample per layer. Lastly, the mean heat gap is presented in **Figure 4-11**. The two distinct heat gaps were formed because of the two different scan speeds that were selected for the initial design of experiments.

From the preceding discussion, we conclude that the parameters capture very critical information about location as well as processing condition.

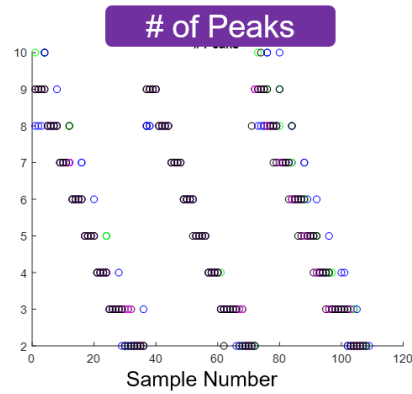


Figure 4-10: Scatter plot for number of peaks observed in temperature history. Nine clear clusters along y-axis are observed which are related with the layer number.

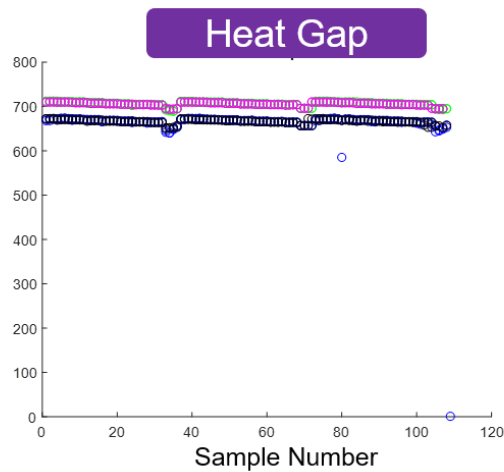


Figure 4-11: Scatter plot for number of mean heat gap observed in temperature history. Two distinct levels are observed corresponding to the two different scan speeds.

### 4.3.3 Principal Component Analysis

The nine initial parameters were deemed sufficient to capture the information in the temperature profile, but additional correlation analysis was done to make sure the smallest possible

set of parameters are used for our design purposes. Failing to find a strong correlation between the variables, we moved on to performing the PCA on the parameters. It was observed that the first five Principal Components (PCs) are enough to explain more than 95% of the variation of the data. Similar PCA was done on ARCLD data of the microstructures. Instead of having 4 CLDs (each being 15 dimensional), 24 PCs were used to represent the microstructure. Following section will discuss the Machine Learning model efficacy of current feature engineering.

#### 4.3.4 Process-Structure relationship

The third task is to develop a reduced order model for process-structure in AM based on microstructure characterization technique described above. Linking process parameters directly is difficult because it is hard to represent microstructure by grain size and orientation. Therefore, microstructure characterization was done using ARCLD. Principal Component Analysis (PCA) was used to reduce dimension of microstructure characteristics. Then, several machine learning methods were employed and compared to investigate relationship between process parameters and microstructure.

After the mechanical properties simulation, we developed a database of 534 samples as few of the samples did not have a good convergence in mechanical property simulation. In the final database, thermal history, microstructures, and mechanical properties were reduced to  $9 \times 534$ ,  $23 \times 534$ , and  $2 \times 534$  matrices, respectively. Before formulating the proposed composite neural network, we built smaller networks to see their predictive performance with the current data. For all the neural networks we used one hidden layer with varying neurons per layer, hyperbolic tangent activation functions from input to hidden and hidden to output layers, and loss function was mean squared error between the ground truth and predicted values. For all the cases

we used a 70%-15%-15% training testing and validation split of the data. We used PyTorch to build the neural networks. The result is not too encouraging as the R-squared value is low 0.31 Figure 4-12.

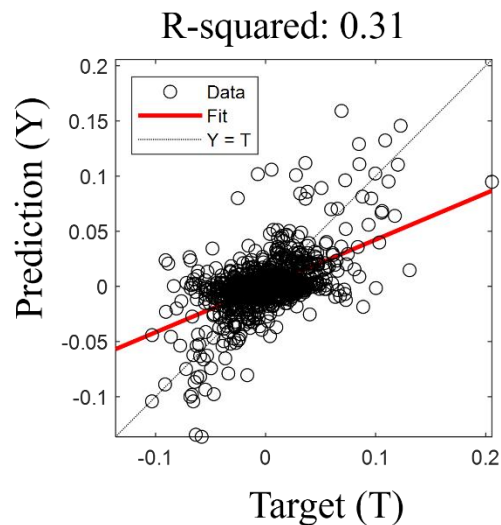


*Figure 4-12: Process-Structure mapping using neural networks.*

Upon investigation, it was revealed that the RVE size is too small to capture the salient features of microstructure. However, having a larger RVE also has its pitfalls: larger RVE results in fewer samples from the build wall, and larger samples are more expensive to compute their properties. Carefully considering the above restriction, the size of RVE was increased by three times and the regression was performed again. The results are much improved as seen in Figure 4-13A. The results can further be significantly increased if instead of using PCAs, the original parameters of the computed ARCLD are used which give an r-squared value of 0.99 Figure 4-13B.

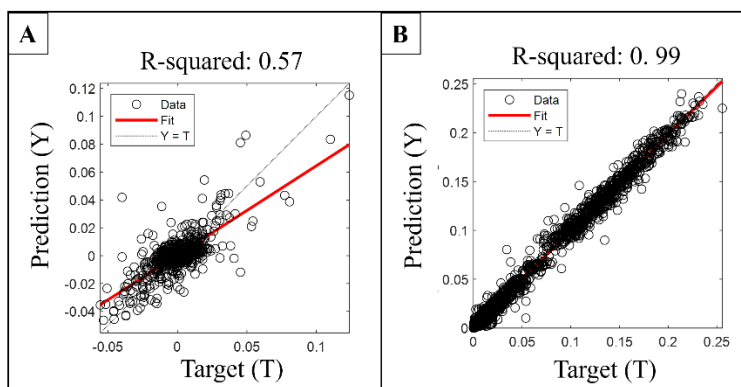


Figure 4-13: Process-Structure mapping using neural networks with larger RVEs. (A) using 23 PCAs. (B) using 56 CLD parameters.

Next step is to build the Structure-Property mapping to complete the PSP link. We built two separate models for the two separate properties: Yield Strength and Young's modulus. The results are very poor as seen in Figure 4-14.

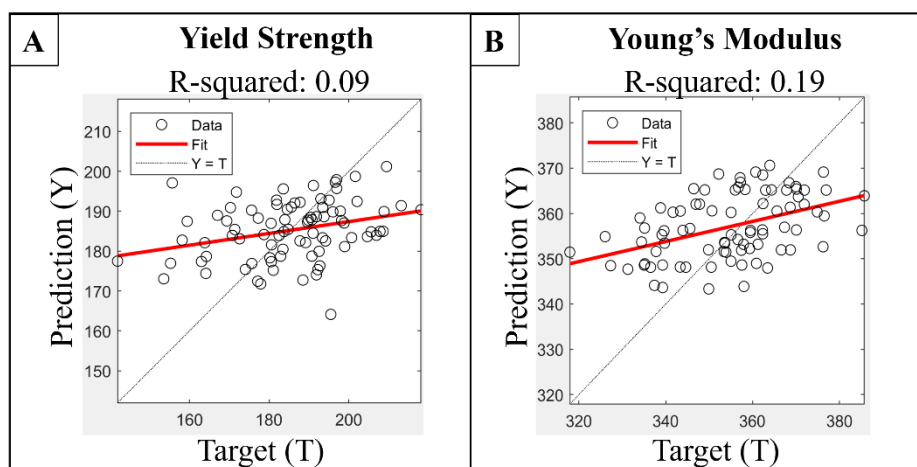


Figure 4-14: Structure-Property mapping using neural networks. (A) Yield Strength prediction. (B) Young's Modulus prediction.

Alternatively, we attempted to build direct Process-Property mapping using neural networks. The results are slightly better, but still not significant. Upon looking at the property distribution, it was noticed that the property values are too random, and this is adding too much

noise to the model making it difficult to predict the properties accurately. The probable cause of these erroneous values is the underlying assumption of symmetric boundary conditions. The small RVEs that we have extracted are not at all symmetric. Thus, the property predictions are almost constant without any major deviation between them as seen in Figure 4-16.

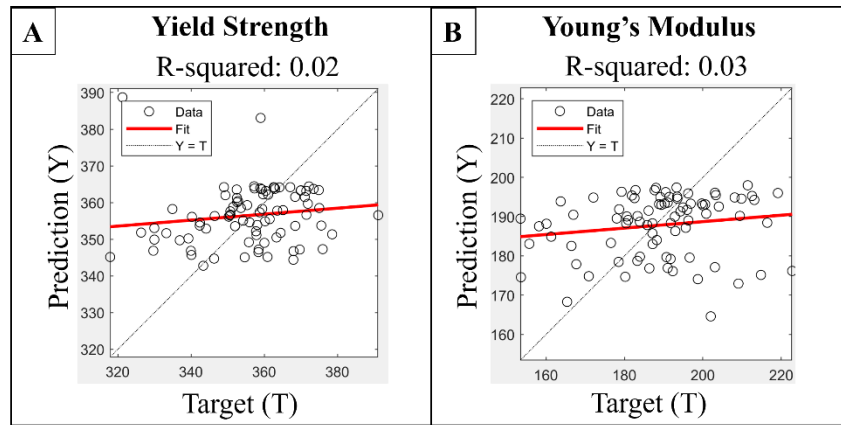


Figure 4-15: Process-Property mapping using neural networks. (A) Yield Strength. (B) Young's Modulus.

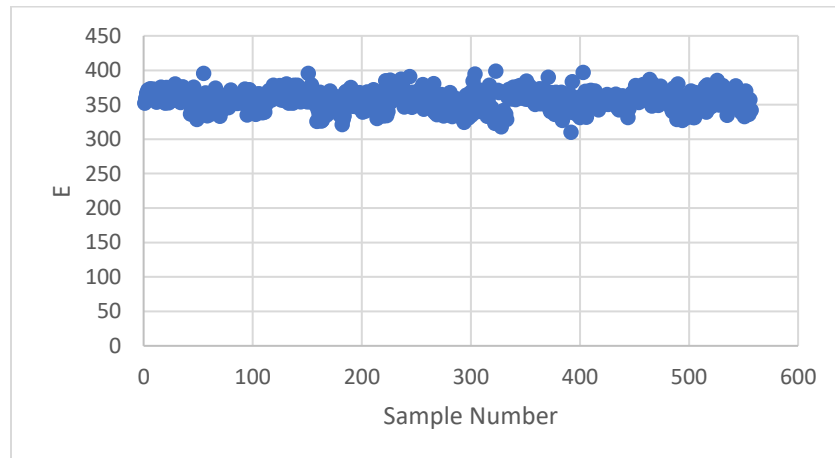


Figure 4-16: Young's Modulus of the dataset against sample number.

In the future work of the current framework, we can retry to compute the mechanical properties using a model other than FFT. Another approach could be to use much larger RVE size, so the effect of the boundary condition assumption is not significant. Once, the property values are accurately calculated, we can have the complete PSP link which can be an efficient tool for

studying the effect of processing conditions on the properties of metal AM parts. While the methods used in this case study are specific for the dataset presented, they can be altered to suit a variety of investigations and data types.

#### 4.4 Application in Cellular Automaton (CA) model Calibration

The CA model consists of two sub-models: (i) the nucleation model and, (ii) the grain growth model [80,93]. In the nucleation model, nucleation sites are randomly distributed in space with a given density. Grains nucleate from the nucleation sites when undercooling (the temperature difference between the liquidus temperature and the local temperature) is higher than a critical undercooling value, also chosen randomly for each site from a given distribution, as are the crystal orientations of newly nucleated grains. For the grain growth model, the growth velocity is governed by a physically based dendrite tip growth kinetics law. However, some physical parameters in the CA model, such as nucleation site density and dendrite growth rate coefficients, are unknown and hard to measure directly from experiments. Therefore, it is necessary to calibrate the physical parameters in the model using microstructure images from experiments to simulate the microstructure evolution accurately.

The question is how to quantitatively assess the difference between the microstructures from simulation and experiment, respectively. Without a single, easy-to-interpret scale measure of error, it is challenging to compare simulated and experimental microstructures to calibrate the unknown physical parameters in the model. The microstructure simulation model is often validated by visually comparing the morphology of grains in experiments and simulations. To automate this process, and to increase accuracy and robustness, it is necessary to develop models to quantitatively characterize microstructures, compare the results from both simulations and

experiments, and then calibrate (infer) the unknown parameters in the CA model. The first step of this approach is to identify descriptors to characterize the high-dimensional microstructural features. There are some popular descriptors readily available that can extract these features from a given microstructure such as equivalent spherical diameter [94], elongation ratio [95], and other area-based grain statistics. But these methods have limitations, e.g., despite its wide use, equivalent spherical diameter [94] fails to capture the anisotropy of a grain: an absolute spherical grain and an oval grain both can theoretically have the same equivalent spherical diameter. Equivalent spherical diameter also does not capture the critical grain shape orientation information of the grains under study. Elongation ratio [95] measures the ratio of major and minor axis by assuming the shape of the grain as an oval, whereas the grains in AM do not conform to any generalized shape. Other grain area-based statistics are similarly unable to provide any information about the shape of the grain. To overcome these limitations, we look towards another method, angularly resolved chord length distribution (ARCLD) [96] which has been talked at length in the previous section (4.2).

Another challenge is that when calibrating the parameters in the CA model, it is difficult to manually tune the CA model parameters through trial-and-error. An automated approach is needed to tune the model parameters to match microstructures between simulations and experiments. This can be achieved by casting the calibration problem as an optimization problem with the objective of minimizing the difference between responses from simulations and experiments. The most prevalent optimization techniques such as linear and quadratic programming could be used to find the optimum, but the well-known drawback of these approaches is that they are expensive and can get stuck at a local minimum. Other global optimization algorithms, such as genetic algorithm [97], can achieve the global optimum.

However, genetic algorithm is best suited for problems where the underlying function evaluation does not take a lot of time, which is untrue for the expensive CA simulation. A single CA simulation of additively manufactured microstructure implemented with parallelized C++/MPI codes in this work can take up to 10 hours on a high-performance computing Linux workstation with 6 computing processors. Alternatively, Bayesian optimization (BO) [98] is a very efficient optimization algorithm that requires minimum function evaluation and can also find the global optimum. An additional relevant feature of BO is that it works well with highly nonlinear functions, which is often expected of the calibration problems. In the literature, BO has been used to calibrate computational models [99], including material simulation models such as physics-based precipitation model [100]. However, the application of Bayesian optimization in CA calibration is limited [101,102].

In this work, a 3D Cellular Automaton method is used to predict microstructure evolution during the laser scan of a bare plate, representative of track melting and solidification during an additive manufacturing process. To calibrate the CA model, a grain characterization method combined with a Bayesian optimization framework is proposed to quantitatively compare microstructure images from simulations and experiments and automatically calibrate parameters in the CA model. In detail, the Angularly Resolved Chord Length Distribution (ARCLD) is applied to characterize grain structures which consider both grain size and orientations. To quantitatively compare the ARCLDs for microstructures from simulation and experiments, a Dissimilarity Score (DS) is created using the Earth Mover's Distance (EMD) method as the metric of dissimilarity. The Bayesian optimization algorithm is used to tune parameters in the CA model to efficiently calibrate the model by minimizing the DS. The results show the effectiveness of the proposed

calibration framework and the improved performance of the microstructure prediction. The novelty of our work is two-fold: (i) we introduce the DS metric to quantitatively differentiate between granular microstructures, and (ii) we use this metric in conjunction with Bayesian optimization to calibrate the CA model parameters efficiently and accurately.

#### 4.4.1 CA simulations

The CA method is used to simulate the evolution of grain growth during the AM process. The CA method can predict columnar, equiaxed and mixed grains. In our simulations, a predefined microstructure (usually equiaxed grains) is first generated to represent the pre-existing microstructure in the substrate. Material within the melt pool region is then melted, and new grains grow from the existing substrate grains and new nucleation sites during resolidification. Columnar grains are more likely to form than equiaxed grains formed under high thermal gradients in the melt pool region.

The CA model consists of two models: (i) heterogeneous nucleation model, and (ii) grain growth model. The nucleation model determines the number of nucleation sites, locations of nucleation sites, and crystal orientations. The nucleation site density ( $n_p$ ) usually must be calibrated based on experimental grain measurements. In the grain growth model, for computation efficiency, the dendrite tip growth rate is described with a polynomial approximation following the dendrite tip growth kinetics law:

$$v(\Delta T) = \lambda_1 \cdot \Delta T + \lambda_2 \cdot \Delta T^2, \quad (4-13)$$

where  $v$  is dendrite tip growth rate (mm/s);  $\lambda_1$  (mm/(s K)) and  $\lambda_2$  (mm/(s K<sup>2</sup>)) are coefficients of grain growth rate that must be calibrated based on dendrite tip growth kinetics;  $\Delta T$  is undercooling (K),  $\Delta T = T_l - T$ ;  $T$  is the local temperature; and  $T_l$  is the liquidus temperature.

In this work, single-track bare plate laser scans (no powder) on Inconel 625 are simulated for three cases. The laser scan parameters for Cases A, B, and C, corresponding to experimental cases published by NIST [103] as described in the next section, are listed in Table 1. The beam diameter is 100  $\mu\text{m}$ . The beam diameter is the full width at half maximum with Gaussian distribution. The velocity and temperature fields during each scan are simulated using a thermal-fluid model, details of which can be found in [104]. To predict the microstructure during the solidification process of each case, the resulting temperature field is transferred as the input to a cellular automaton (CA) model. with domain size [0.3, 0.20, 0.067] mm in the [x, y, z] coordinates. The x direction is the laser scan direction. The CA mesh uses cubical cells of side length 0.5  $\mu\text{m}$ , giving  $3.216 \times 10^7$  cells. The computational domain of the CA model is smaller than the thermal-fluid model, allowing a finer cell size; linear interpolation method is used to transfer the temperature field from the thermal-fluid model to the finer CA mesh. More details of the CA method can be found in the authors' previous papers [80,93].

In the CA model, an initial substrate microstructure must be created before modeling the solidification process in AM. These grains are created through a separate CA simulation by uniformly cooling the substrate from above the liquidus temperature, with a constant cooling rate

of -20.3 K/s. The critical undercooling values of nucleation sites are selected randomly from a Gaussian distribution:

$$\frac{dn}{d(\Delta T)} = \frac{n_p}{\Delta T_\sigma \sqrt{2\pi}} \exp \left[ -\frac{1}{2} \left( \frac{\Delta T - \Delta T_{mean}}{\Delta T_\sigma} \right)^2 \right], \quad (4-14)$$

where  $n$  is the nucleation site density (number per volume);  $\Delta T$  is undercooling;  $n_p$  is the mean nucleation site density ( $\text{mm}^{-3}$ );  $\Delta T_\sigma$  is the standard deviation of the distribution;  $\Delta T_{mean}$  is the mean nucleation critical undercooling. For initial substrate,  $\Delta T_\sigma = 0.5$  K and  $\Delta T_{mean} = 2.0$  K; for the laser scan simulations,  $\Delta T_\sigma = 5.0$  K and  $\Delta T_{mean} = 18.0$  K. The total number of nucleation sites in the bulk,  $N_v$ , is calculated by

$$N_v = n_p V, \quad (4-15)$$

where  $V$  is the volume of the microstructure domain. Since  $n_p$  is unknown and hard to measure directly in experiments, we need to calibrate  $n_p$  based on the experimental microstructure.  $n_p$  is different for substrate creation and the laser scan simulation, which need to be calibrated separately. More details are discussed in Results section.

In the CA model, nucleation sites are activated (begin growing) when the critical undercooling for that site is reached. Grains grow with a velocity given by Equation (4-14). During the laser scan simulation, existing grains can be remelted and resume growing when the local temperature drops below the liquidus temperature; new grains can also be nucleated from sites in the melt pool.

The mean nucleation site density ( $n_p$ ) and two grain growth rate coefficients ( $\lambda_1$  and  $\lambda_2$ ) are unknown and must be calibrated against experiments. For the sake of calibration efficiency, because growth rate depends more strongly on  $\lambda_2$  than  $\lambda_1$ , only two parameters are calibrated:  $n_p$  and  $\lambda_2$ .

#### 4.4.2 Model Calibration Framework

The calibration of CA model parameters is a sequential process: (1) The model parameters are calibrated for the substrate microstructure only, and (2) the calibration is repeated for the laser scan microstructure, using the substrate microstructure as an initial condition. Figure 4-17 shows the schematic of the framework for calibrating the CA microstructure model in AM using the Dissimilarity Score (DS) for each of steps (1) and (2). The basis of our framework lies in formulating the objective function to incorporate the dissimilarity score as a function of the to-be-identified calibration parameters:

$$\begin{aligned}
 Y(x) &= DS(Simulation(x), Experiment) \\
 &= \frac{1}{N} \sum DS(Simulation_j(x), Experiment_j),
 \end{aligned}
 \tag{4-16}$$

where  $x$  are the calibration parameters,  $j$  is the index of experimental images and corresponding simulations with the same unique processing conditions, and  $N$  is the total number of such unique experiments. To gauge the predictive capability of the calibration, it is advised to have at least one experiment set aside which can act as a test set.

We begin with a set of experimental images that act as ground truth. Next, the set of parameters,  $x$ , that are most consequential to the model calibration are determined based on literature and experience with CA modeling. Based on the range of these parameters, we perform an initial design of experiments and generate a small set of  $x$  values with which to perform CA simulations. For each value of  $x$ , the resulting microstructure images from simulations are compared with all available ground truth images and their DS and then the objective function  $Y(x)$  are calculated. For the laser scan calibration, equation (18) is computed by averaging over the two experimental cases compared with the corresponding simulations. However, for the substrate material calibration, only one simulated microstructure is computed, and therefore in (18) each experimental substrate is compared with a single simulation, i.e., the simulation data is the same for all value of  $j$ .

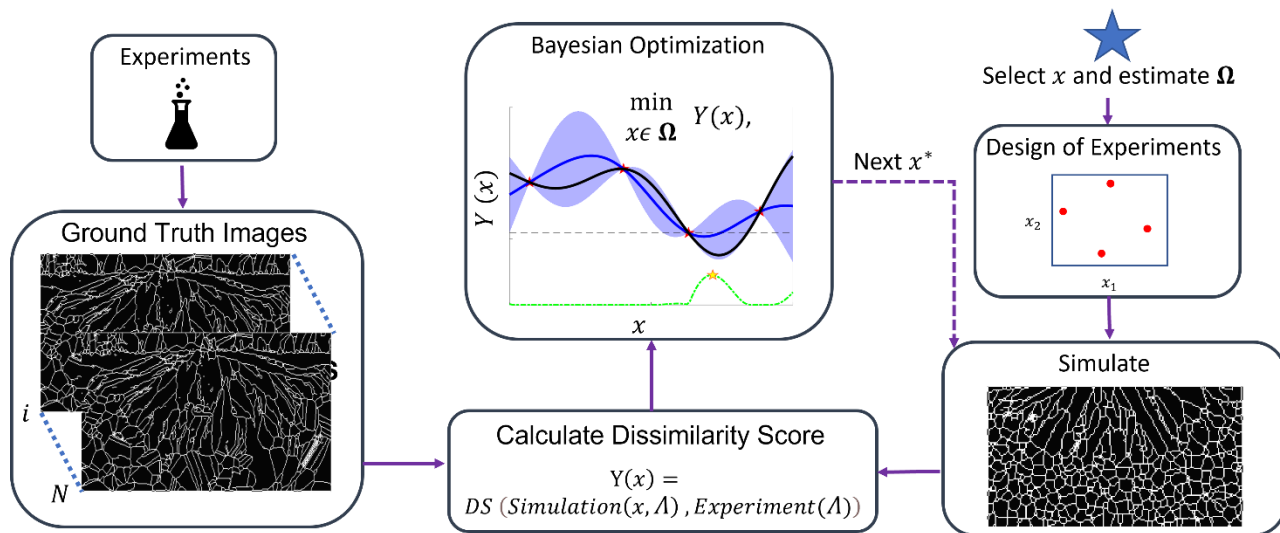


Figure 4-17: Framework for model calibration of Additive Manufacturing microstructure simulation using Dissimilarity Score.

BO can be used to optimize  $x$  to minimize the objective function defined above. In BO, first a surrogate model is built using the initial data points of parameter  $x$  and responses  $Y(x)$ . As explained in Section 2.3, BO provides us with the next point to sample,  $x^*$ , which is then input into the CA model to perform new simulations to calculate  $Y(x^*)$ . This is repeated iteratively until reaching some termination criteria, which could be the number of iterations, improvement in activation function or objective function, etc.

Though the framework is not restricted by the number of images or the parameters, in our study there are only three experimental images with unique processing conditions ( $N = 3$ ), and two calibration parameters  $\theta$ : nucleation density ( $n_p$ ) and grain growth rate coefficient ( $\lambda_2$ ). Based on experience and the literature [93,105,106], we set two different ranges of these parameters for the two separate calibrations (substrate formation and laser scan). For substrate formation the range is set as  $\{n_p, \lambda_2\} \in [1 \times 10^6, 2 \times 10^7] \times [1.5 \times 10^{-4}, 2.5 \times 10^{-4}]$ , while for the laser scan it is  $\{n_p, \lambda_2\} \in [3 \times 10^3, 1 \times 10^8] \times [0.3, 1.5]$

#### 4.4.3 Results and discussion

The result section is divided into two parts: (1) Calibration of CA model parameters for substrate microstructure, and (2) Calibration of CA model parameters for laser scan microstructure. As previously mentioned, though the framework for calibrating both is same, but the design space and BO intricacies differ.

##### 4.4.3.1 Substrate calibration

The calibration process was initiated by selecting four sampling locations of nucleation site density ( $n_p$ ) and grain growth coefficient ( $\lambda_2$ ) as shown in Figure 4-18. For the grain growth model

in equation (1),  $\lambda_1 = -5.44 \times 10^{-5} \text{ mm}/(sK)$  is chosen for the substrate microstructure. The value of  $\lambda_1$  is chosen based on experience within the parameter range from  $-6.0 \times 10^{-5} \text{ mm}/(sK)$  to  $3.0 \times 10^{-5} \text{ mm}/(sK)$  for nickel-based alloy from literature [93,105–107].

Using these initial values, CA simulations are carried out to predict the substrate microstructure. As the output of CA simulation is 3D, we slice the microstructure perpendicular to the laser scan direction and extract the resultant 2D images. As we are only interested in the substrate region, we crop it out. Then, using equation (4-11), we average out the CLD of all the cropped-out cross-sections. Then using equation (4-12), DS is calculated by comparing the substrate region of one simulation against the extracted substrate microstructures from the three available experiments three available experiments. The three experiments are with different processing conditions but the substrate area are identical since the substrate microstructures are not affected by the laser scan. The DS results of the initial four simulations are listed in Table 4-3. One cropped out sample from each simulation (Figure 4-19 A) along with the ground truth images (Figure 4-19 B) are shown in Figure 4-19. Though it is hard to visually compare these microstructures with the three ground truth cases, one prominent result that can be drawn is that Sample 4 has the biggest grains amongst all the simulations, and it is also very different from the ground truth images. The resulting largest DS value for Sample 4 is yet another proof of the efficacy of DS.

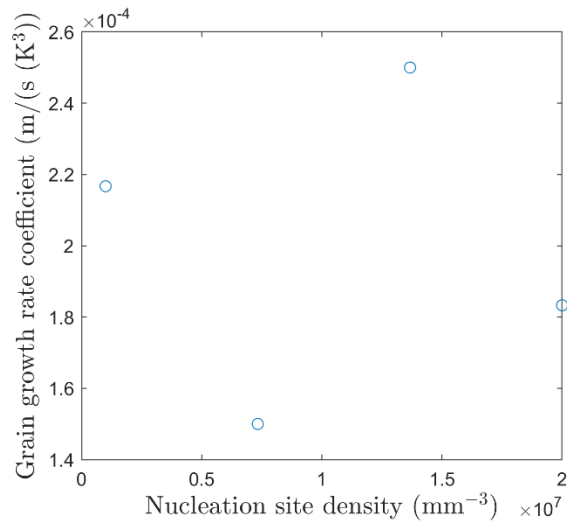


Figure 4-18: Initial design space of parameters for substrate grains calibrations.

Table 4-3: Initial calibration parameters and dissimilarity scores for substrate grains calibration.

Parameters			Dissimilarity Score (substrates)			
#	Nucleation Density ( $\text{mm}^{-3}$ )	Growth rate Coefficient ( $\times 10^{-4} \text{ mm}/(\text{s K}^2)$ )	Case A	Case B	Case C	Average (Y)
1	$1.37 \times 10^7$	2.50	2.1254	4.1399	1.5031	2.589
2	$2.00 \times 10^7$	1.83	3.5073	6.2229	3.1618	4.297
3	$7.33 \times 10^6$	1.50	2.1024	4.3446	1.5535	2.666
4	$1.00 \times 10^6$	2.17	7.4062	4.6889	7.7441	6.613

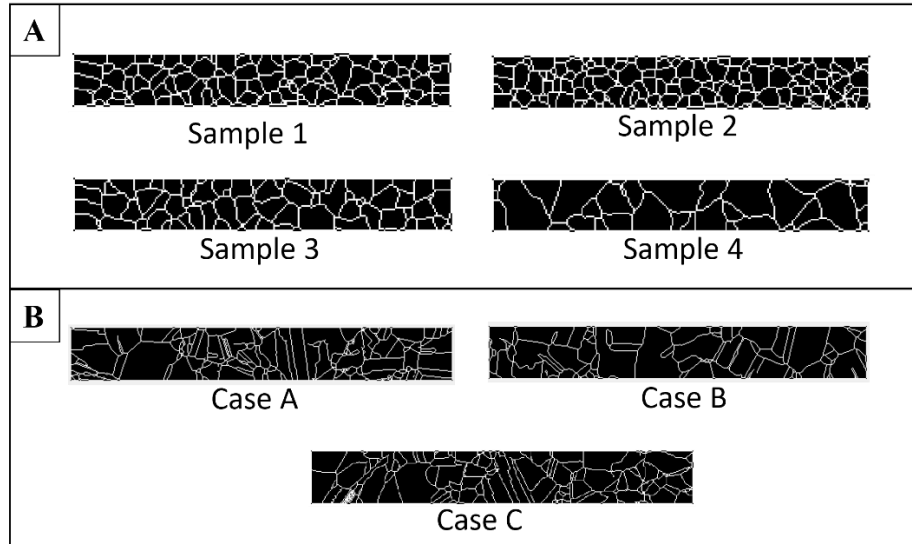


Figure 4-19: Four initial simulation vs experimental substrate microstructures. (A) Select cross-sections of simulated substrate microstructures; (B) Experimental substrate microstructures for Case A, B, and C.

The average DS values from the three images is our target function  $Y$  to minimize using BO. The initial values of the parameters along with  $Y$  is used to build the GP surrogate model for BO. Using EI as our activation function,  $Y$  was optimized in 17 iterations at which the termination criteria were met. The resulting history of  $Y$  is plotted in Figure 4-20. It is observed that in just six iterations, a close-to-optimal solution was discovered. We note the typical exploration VS exploitation behavior of BO in the consecutive peaks and troughs. A 3D representation of the calibration space is shown in Figure 4-21. The resulting surrogate model exhibits a very non-linear shape which would have been very difficult to optimize if a non-BO approach had been applied. The optimal value of  $Y$  obtained by our model is 1.88, and the optimal value of parameters  $x^*$  is:  $3.68 \times 10^6 \text{ mm}^{-3}$  and  $2.5 \times 10^{-4} \text{ m}/(\text{s K}^2)$ .

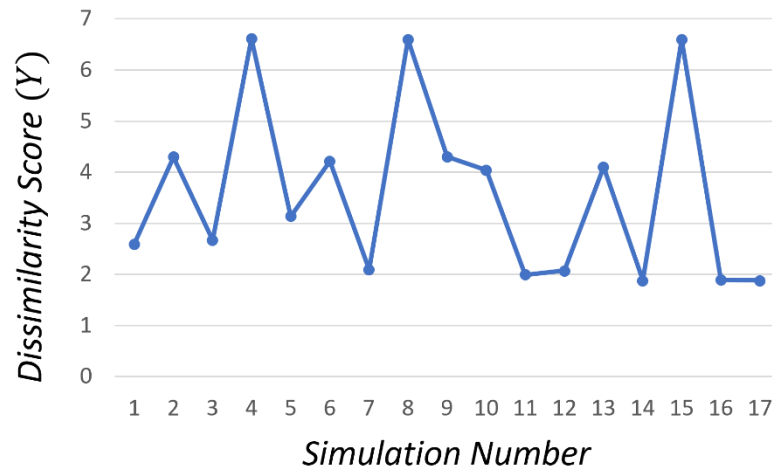


Figure 4-20: History of Dissimilarity Score computed for CA parameters calibration.

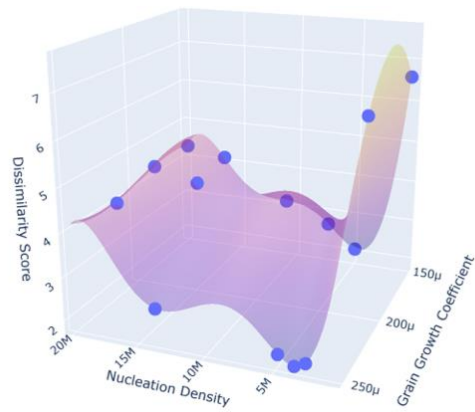


Figure 4-21: Calibration space of Bayesian optimization process. The surface plot represents the GP model of DS, and the blue spheres represents the samples.

#### 4.4.3.2 Laser scan calibration

Similar to substrate calibration, we begin laser scan microstructure simulation model calibration by selecting four sampling locations of nucleation site density ( $n_p$ ) and grain growth coefficient ( $\lambda_2$ ) as shown in Figure 4-22 and tabulated in Table 4-4. For the grain growth model in equation (1),  $\lambda_1 = -0.89 \text{ mm}/(\text{s K})$  is used for the laser microstructure, and the range of design parameters  $n_p$  and  $\lambda_2$  is different from the previous calibration:  $\{n_p, \lambda_2\} \in [3 \times 10^3, 1 \times 10^8] \times [0.3, 1.5] = \Omega$ . The units of  $n_p$  and  $\lambda_2$  are  $\text{mm}^{-3}$  and  $\text{mm}/(\text{s K}^2)$  respectively. The parameter range of  $n_p$ ,  $\lambda_2$  and value of  $\lambda_1$  are chosen based on the material properties of Inconel 625 in additive manufacturing.

Using the initial four values, CA simulations are carried out to predict the laser scan microstructure. Just like in previous calibration, we slice the 3D microstructure perpendicular to the laser scan direction and extract the resultant 2D images. Using equations (4-11) and (4-12) we evaluate the DS of each simulation against only two experiments compared to three experiments in the substrate calibration. One set of experiment data is left out for validating the calibration results. The DS results are summarized in Table 4-4.

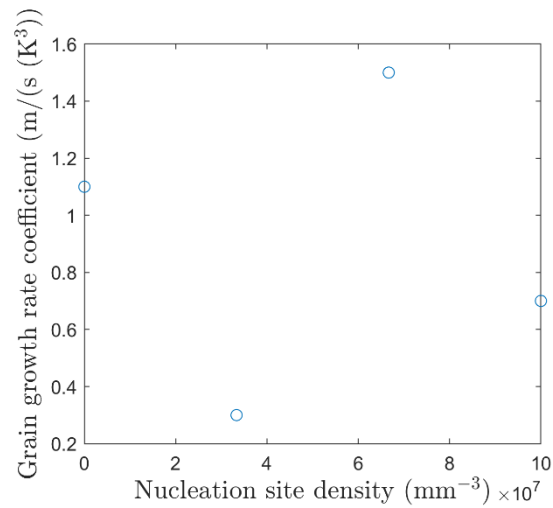


Figure 4-22: Initial design space of parameters for laser scan microstructure calibrations

Table 4-4: Initial calibration parameters and dissimilarity scores for laser scan microstructure calibration.

Parameters		Dissimilarity Score			
#	Nucleation Density ( $\text{mm}^{-3}$ )	Growth rate Coefficient	Case B	Case C	Average (Y)
			1	$3.33 \times 10^7$	
2	$1.00 \times 10^8$	0.7	3.611	1.429	2.520
3	$3.00 \times 10^3$	1.1	1.654	1.277	1.465
4	$6.67 \times 10^7$	1.5	3.202	1.309	2.255

Similar to the previous substrate simulation calibration, BO was performed on the initial dataset and iterated until we reached the termination criterion i.e., 10 iterations. Additionally, we

observe that there was no significant gain in expected improvement after the fourth iteration as seen in Figure 4-23.

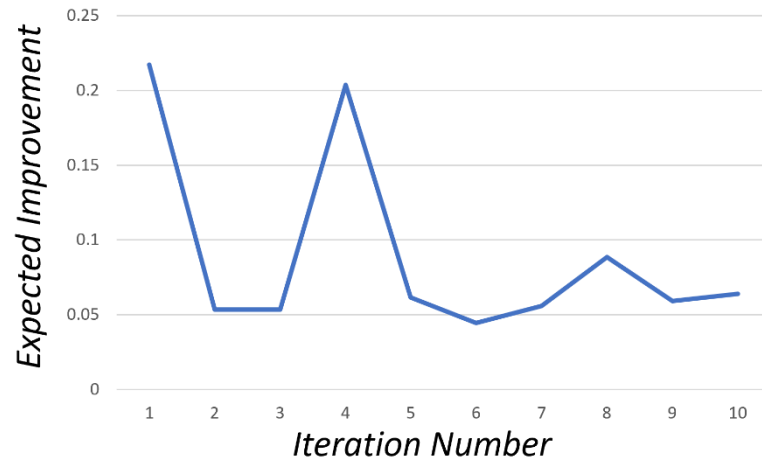


Figure 4-23: Maximum Expected Improvement Score for each iteration of Bayesian Optimization.

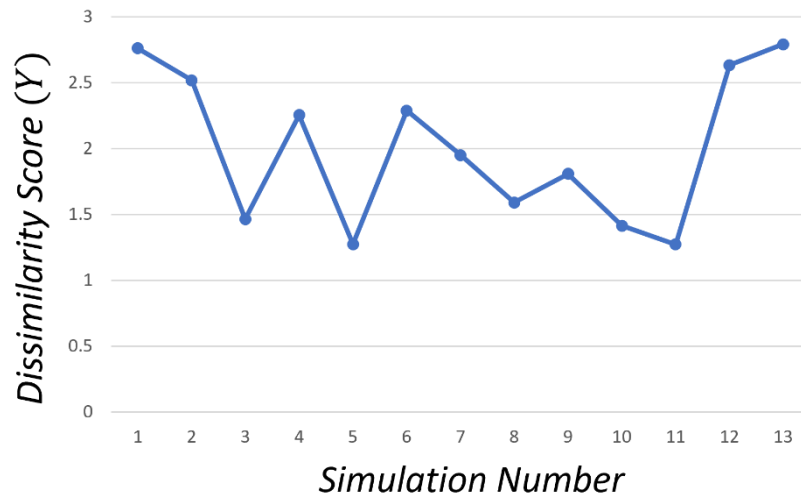


Figure 4-24: Dissimilarity Score of each iteration for calibration of the entire laser scan microstructure.

The DS results of all the iterations are plotted in . It is observed that we had reached close to the optimum in the first iteration (Simulation # 5) after the initial four samples (DS=1.2734),

and further runs did not improve the score too much. This proved the efficacy of using BO which can find the optimal result in minimal possible runs. If we had terminated the run sooner, the loss in accuracy wouldn't be too significant. Depending on the computational budget, one can decide to either run more simulations or just use the very next suggested point in BO. The best score was 1.2717 with the corresponding optimal point as  $x^*$  is:  $3 \times 10^3 \text{ mm}^{-3}$  ( $n_p$ ) and  $0.3 \text{ mm}/(\text{s K}^2)$  ( $\lambda_2$ ) at simulation number 11. The final calibrated microstructure from simulation for Case B and Case C are shown in Figure 4-25 A and C. The cropped experiment microstructures with the same domain size of simulated microstructures are also shown in Figure 4-25B and C for Case B and C, respectively. We test Case A with the calibrated design parameters. The simulated and experiment microstructures for Case A are shown in Figure 4-26. The DS score for Case A is 0.8857, which demonstrates that the simulation agrees well with experiment images for Case A.

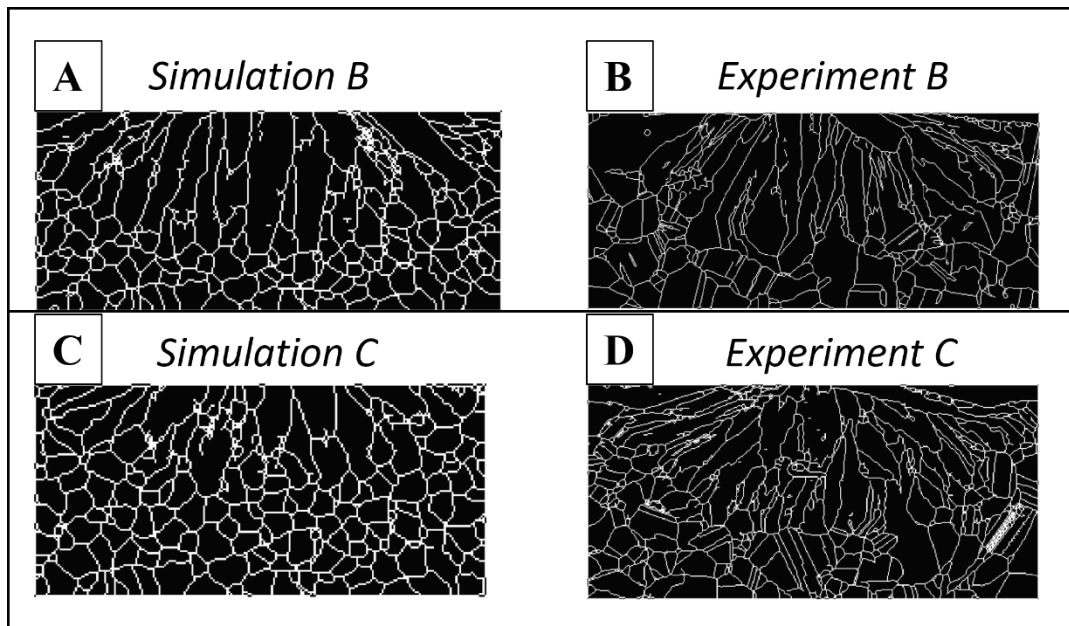


Figure 4-25: Calibrated microstructure for case B and C compared with experimental images.

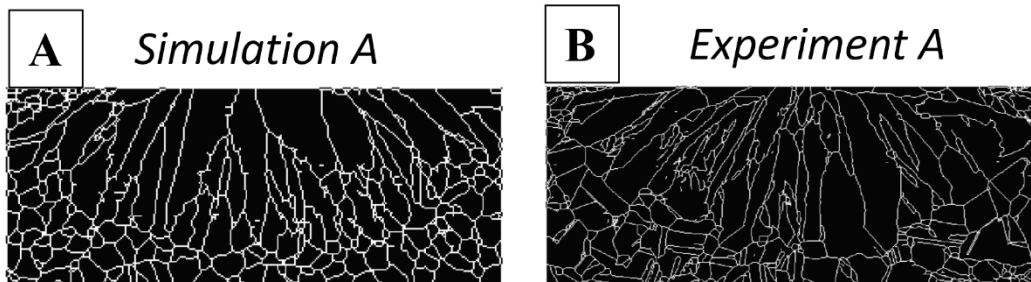


Figure 4-26: Calibrated microstructure for case A compared with experimental images as the testing case.

#### 4.5 Summary

In this chapter, we expanded the use of Chord Length Distribution (CLD) to not only characterize the microstructure more efficiently, but also to develop a novel metric, named “Dissimilarity Score”, which can differentiate between granular microstructures quantitatively. Previously there was no metric which could do this quantitative differentiation, and the state-of-the-art involved error-prone visual comparison. This hindered not only model accuracy, but also the calibration process. Because of the development of this novel metric, the calibration process of microstructure simulation model can be automated. We presented an application of this calibration framework using DS in its center to calibrate the Cellular Automaton (CA) simulation model. The calibration of CA is two step process where the first step involves calibration of the substrate and the second step involves calibration of the build microstructure.

We also modified the CLD to enable the effective, yet reduced, microstructure presentation. Based on this reduced order effective representation, we endeavored to build a Process-Structure-Property model for metal AM to save the cost of expensive process-structure and structure-property simulation. Though we achieved encouraging results for process-structure relationship, but the whole PSP chain could not be completed because of the noise in property

calculation occurring due to the small size of RVE. In future, the PSP model could be completed with a better property dataset.

In the previous chapters we discussed characterization techniques for quasi-random and granular microstructures but there are some microstructures do not fall in any general category and can be classified as complex microstructures. For such microstructures, it is almost impossible to characterize them using the traditional tools that we have talked about so far. In the next section we explore the possibility of using advance machine learning tools such as transfer learning to characterize the complex microstructures so that they can be used for design.

## Chapter 5 Transfer Learning for Complex Multi-Scale

### Microstructures with Limited Data

#### 5.1 Introduction

Silicone rubbers are extensively used due to their durability under different conditions and applications including cookware, sound damping materials and medical devices. In such applications, silicone elastomers are often used under dynamic loading conditions, and they often fail due to fatigue. During a fatigue process, the factor that determines the lifetime of usage is the gradual growth of minor cracks over long periods of time. The goal of this study is to use image samples of such surface cracks to build and quantify their relationship with mechanical properties and environmental factors.

There have already been extensive studies on elastomer viscoelastic properties [108–112], elastomeric fracture and fatigue in order to determine the factors and underlying mechanisms that influence the process of crack propagation [1-5]. One such theory of analysis is Linear elastic fracture mechanics (LEFM) which describes the fracture behavior of brittle materials and assumes linear elasticity in the bulk material except for the crack tip region where the crack tip propagation is characterized by the Griffith energetic criterion [113]. The Griffith crack propagation theory argues that fracture energy  $\Gamma$  is equilibrated by the strain energy  $\mathcal{G}$  such that  $\Gamma = \mathcal{G}$  at the point of failure. This theory can be extended for soft materials that form blunt crack tips with large strains and non-linear behaviors at the crack tips. Accordingly, energy dissipation is determined by different length scales near the highly stretched region of the blunt crack, as described by Creton

and Ciccotti [114]. In the far-field loading zone, bulk energy dissipation occurs, and can be described by the viscoelastic properties of the material. Details of the crack propagation process dominate the behavior close to the crack tip. In a small region very close to the crack tip, material damage takes place at the molecular level. The related meso-scale material damage includes cavitation, fibrillation and the formation of secondary cracks [114,115], resulting in distinct fracture surface morphologies. For this reason, we hypothesize that images of the fracture surface morphology contain information about the fracture process that be mined by subsequent analysis of the fracture surface.

Fracture surfaces are historical imprints of a crack front that has traversed through the bulk material. Like the grooves of vinyl records, information during fracture can be traced along the fracture surface pattern, giving us a more detailed overview. Many studies described their observations and tried to explain the underlying mechanisms. In the 1950s, Thomas and Greensmith [116] reported the transition from a rough, irregular torn surface to a smooth surface along with the increase of crack speed in natural rubber and styrene-butadiene rubber. In addition to the irregular roughness, step-like, faceted surfaces were also found to commonly exist in amorphous materials, forming so-called crosshatch patterns [117–119]. Quite a few mechanisms have been proposed to understand the crack surface formation process. Seitz et al. [118] and Baumberger et al.[120] attributed to the strong anisotropy generated with certain angles in the stress field [118,121,122]. Gent et al., Tanaka et al., and many other researchers elucidated by discussing the mode mixites and the intersection of secondary cracks ahead of the tip [115,117,122–124]. Although given such extended discussions about fracture surfaces, the field of discussion is mostly limited to fast fracture of gels or crosslinked elastomers, and very few

focused on fatigue experiments. Additionally, because of the time-consuming nature of fatigue experiments, learning the fatigue fractography will not only help build a better correlation between the measured mechanical responses of the material and the created surface pattern, but also provide a possibility to reversely predict the fatigue properties from a fracture surface in future applications, so that repetitions in fatigue studies can be avoided or reduced.

In this study, we focus on previously reported crack surfaces of silicone rubber samples that were collected from fatigue experiments under different temperatures [125]. In the previous work, a change in crack surface morphology under different temperature and loading conditions was found, that when temperature increases, fatigue samples under the same strain show the transition from rough, cross-hatched surfaces to smoother surfaces. Here, we aim to identify the strong correlation between the collected mechanical properties and the observed patterns and to find the most important determining factors relevant to the formation of the surface morphologies. To this end, the first step involves using the right tools to characterize the underlying microstructure of the fracture surface.

The selection of the characterization techniques has two considerations: (i) the nature of material, and (ii) the properties under study. If the material possesses a regular pattern, then physical descriptors like principal axis orientation angle, elongation ratio [10] etc. could be used. However, if the pattern of the material appears to be random but still has an underlying spatial correlation, then statistical functions like the two-point correlation function [10] could be used. However, sometimes the microstructures are not amenable to characterization by regular methods. Under such circumstances, machine learning methods such as Convolutional Neural Networks (CNNs) can be used to characterize microstructure images.

The microstructure of the crack surface is one such material system that is not trivial to characterize. In literature, the basic features of complex surfaces have been characterized by using spectral density function [126] and extracting the  $h-2$  value [127]. Alternatively, some researchers have tried to extract special descriptors such as dendrite length [128] etc to describe complex surfaces. The limitation of such studies is that they are looking at one particular aspect among all the available features at one time. Such crack-surfaces can be thought of having two different scales as seen in Figure 5-1: (i) meso-scale consisting of the general shape of the ridges, and (ii) micro-scale involving the minute changes in roughness occurring at high spatial frequencies. The characterization techniques mentioned earlier generally target one or the other, and that too only partially. The  $h-2$  value only gives a superficial metric of the local roughness, whereas the spectral density function could be a more effective representation of these roughness features, especially at the micro scale. Similarly, dendrite lengths are also very limited in capturing only certain statistics of the crack geometry, but they are not all inclusive. Alternative methods to characterizing the macro-scale property could be through image-based toughness analysis, such as using convolutional neural networks as mentioned in the previous paragraph.

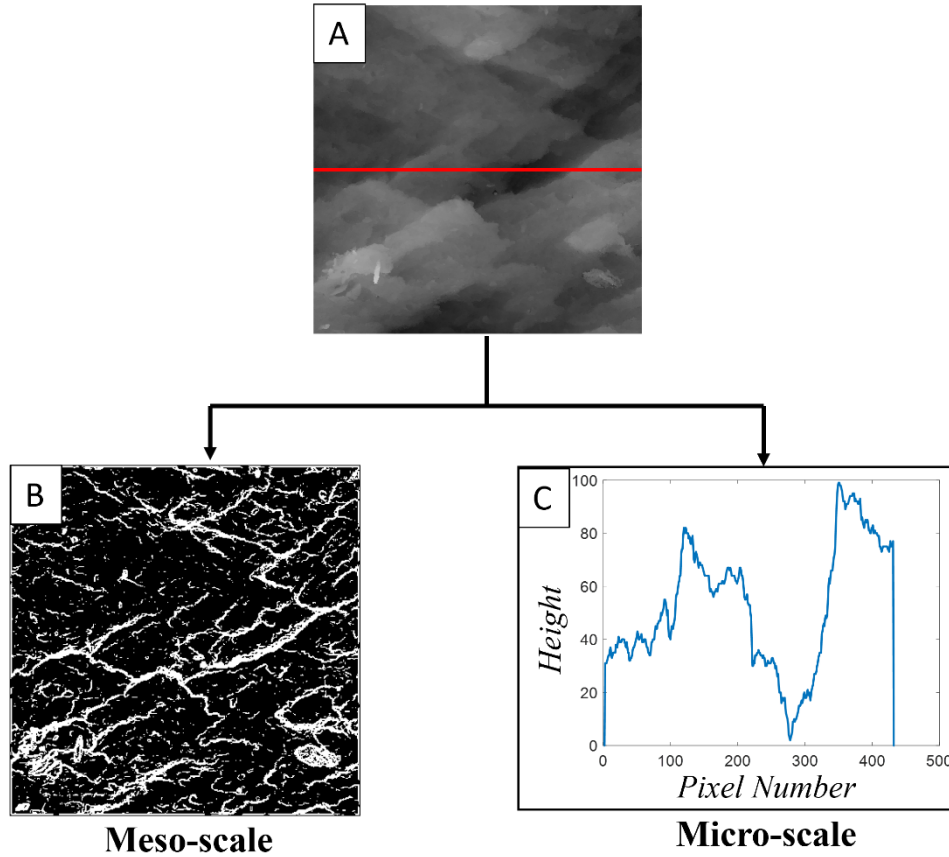


*Figure 5-1: Extracting multi-scale features of a fractured surface of filled silicone rubber. A: Grey scale height image of a silica rubber sample. The red line is a line scan that provides 1D height information(C). B: Meso-scale features which capture the step-like patterns. C: Local roughness computed by scanning the red line over the original image in (A).*

Before discussing CNNs use in image-based toughness analyses, there have been other studies which have attempted to link microstructures to their properties through fracture surface images. One such image-based study by Jandesjek et al [129] implemented a 2D Digital Image Correlation (DIC) method for analyzing fracture parameters of metal materials. However, DIC requires sequential images with special surface treatments for them to produce good results. Another study by Zhang et al. [130] used real microstructure images when designing a Finite Element Model (FEM) to predict fracture toughness. The study found that the FEM could make

more accurate predictions compared to using simplified image representations. However the study didn't provide a machine learning approach for end-to-end image-property prediction, for which we propose to overcome the limitation using machine learning algorithms like transfer learning on CNN as mentioned in 2.2.

In transfer learning, a pre-trained model (i.e., a model whose weights are calibrated) is used to carry out a task which it was not originally trained to do. For example, a model that was trained on classifying items like pencils, cars, etc., is used to classify skin lesions [55]. Because the use of TL for image analysis is a fairly new trend, so far it has not been employed for rubber crack surface in any way, as per the author's knowledge, In this study we aim to employ the concept of TL for crack-surface analysis of rubber.

However, one limitation of TL is that the original model should be trained on a dataset that is broad enough so that it can be useful for the transfer learning task. One well-known dataset for images for successful image-based transfer learning is known as "ImageNet", created by Deng et al. in 2009 [56]. This dataset consists of tens of millions of cleanly sorted and accurately labeled images. Based on the ImageNet dataset, there is a ImageNet Large Scale Visual Recognition Challenge [57] which is a benchmark in object category classification and detection. The challenge has been held annually since 2010 and has produced a lot of efficient deep learning models. Some of the widely used deep learning models include: VGG16 and VGG19 [58], Inception [59], Xception [60], etc.

These pre-trained neural networks have been used for a variety of tasks such as predicting material properties [131], classification of skin lesions [55], microstructure reconstruction [132], and structure-property mapping [131] etc. In this study we propose to characterize. the meso-scale

features of surface roughness using transfer learning for the first time. To take into account for micro-scale features, we propose to first extract the 2D Spectral Density function (SDF) [10] to capture the fine details of roughness, which are otherwise not discernable, and then apply transfer learning on it. The rest of the chapter is outlined as follows: Methods are explained in Section 5.2 including experimental details, post-processing of images, SDF generation, and transfer learning details; Next, we apply the current scheme on two datasets and present the results in Section 5.3.1 (artificial dataset) and Section 5.3.2 (silicone rubber experimental dataset); Lastly, we present conclusion and future directions in Section 4

## 5.2 Methods

### 5.2.1 Experiment Setup

**Sample preparation:** Silicone rubber samples were tested as received from Beijing Institute of Aeronautical Materials (BIAM). The silicone rubber components include 120-1 Phenyl silicone rubber (Shanghai resin factory, China), Cr<sub>2</sub>O<sub>3</sub> (Tianjin Fengchuan Chemical Reagent Technologies, China), GY-209 hydroxyl-ended polysiloxane (Zhonghao Chenguang Research Institute of Chemical Industry, China) Bis(tert-butyldioxyisopropyl)benzene (BIPB) (Shanghai Farida Chemical Co., China) and its filler is Aerosil 380 silica (Degussa, Germany). Detailed compositions are shown in Supplemental information. The filler content was controlled to be 37 phr (parts per hundred rubber) of silica filler and crosslinking agent to be 0.8 phr of peroxide. The components were mixed on a two-roll miller at room temperature. The compounds were press-molded into a 1 mm-thick plate at 170°C for about 10 minutes, and post-cured in an air-circulated oven at 100°C for 2 hours.

**Mechanical tests:** To obtain the fracture surface of the specimens, mode I fatigue tests were performed to obtain the crack growth behavior of the rubber samples. The tests were performed on an Electroforce linear motor from TA Instruments with an environmental chamber to control the temperature. The temperature varied from 22°C (Room temperature) to 100°C for the silicone rubber samples. The samples have dimensions of approximately 25.4 mm × 25.4 mm × 1mm and loaded in pure shear geometry as shown in Figure 3(A), where  $l_0$  is the width,  $h_0$  is the gauge length between two clamps (5 mm), and  $a$  is the crack. Cyclic sinusoidal displacements at a frequency of 2 Hz were applied on the samples with a displacement amplitude of  $\delta_0$  (Varied from 1.25 mm to 5 mm). A pre-conditioning step of 2000 cycles was first applied to the sample without introducing a notch to minimize the influence of Mullins effect in the bulk material. After the pre-conditioning cycles, a razor blade was used to introduce a ~2 mm pre-crack on one edge of the sample. Then, another round of cyclic loading with the same  $\delta_0$  and frequency was applied. The fatigue test continued until substantial crack propagation was observed.

**Data acquisition:** The fatigue crack surfaces were visualized with an Olympus 3D laser confocal microscope with a 10× objective lens. Figure 5-3(B) shows the schematic of the setup. For each rubber specimen, multiple square-shaped crack surface images can be collected depending on the crack length after the fatigue experiment. Each picture has a dimension of 1024 × 1024 pixels (~1.2 mm length). Figure 5-3 shows a set of representative sample images of one intensity image and one height image. Intensity image captures the brightness and luminance change of the figure, therefore recording details based on light source quality. Here, only height images are used for the machine learning process because the height images are presented in color gradients based on the

height variations in 3-dimension. In addition, a datafile of the height data can also be exported so that the height image can be reconstructed using coding tools.

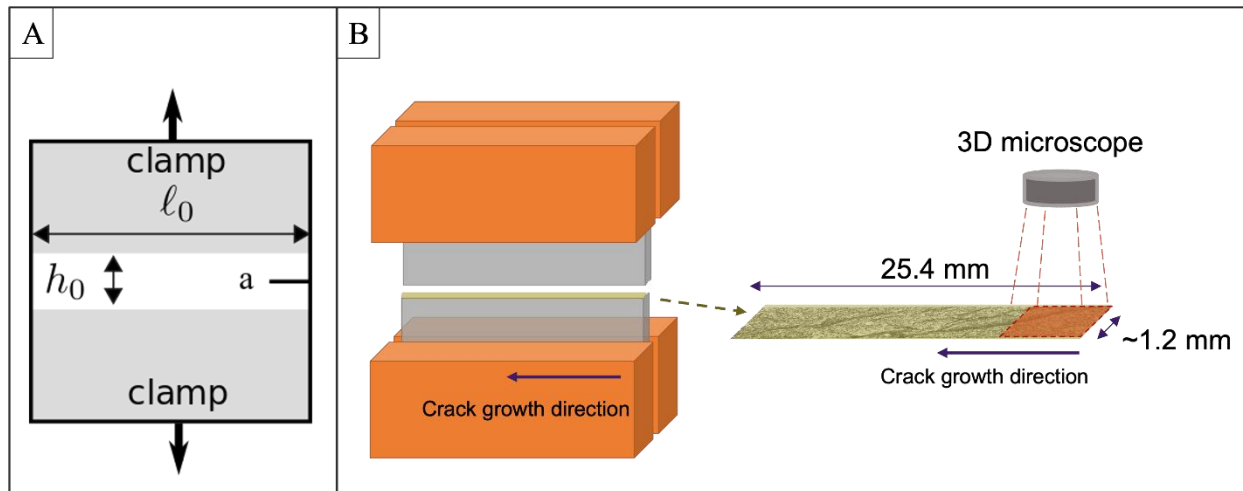


Figure 5-2: The experimental setup. (A) Model I fatigue test in pure shear geometry. The middle white area is the test area. An initial pre-crack 'a' was introduced before the fatigue test. (B) Schematic of the fatigue crack surface observation process using a 3D microscope.

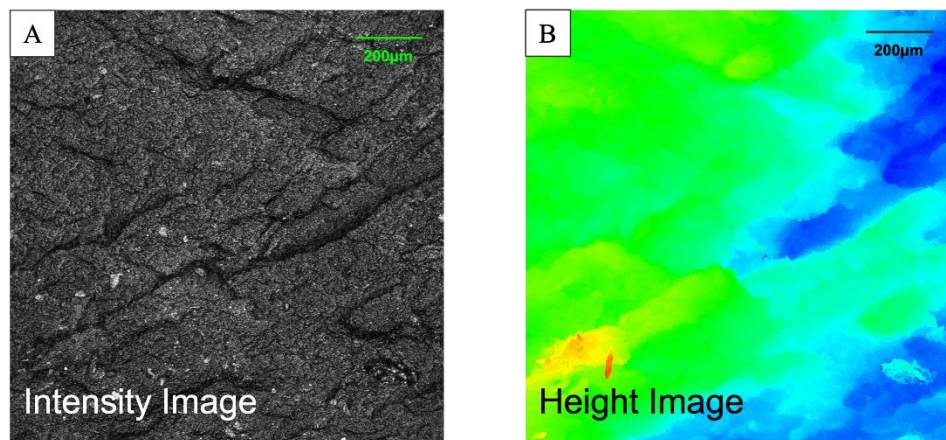


Figure 5-3: Sample sets of one intensity image and one height image from a 3D scan.

## 5.2.2 Post processing of images

While the 3D microscope has provided an abundant variety of details, the raw images provided cannot be directly used for transfer learning. The absolute heights of the samples are not all the same, and their length scale needs to be normalized in order to provide comparison between different specimens. Moreover, random noises have been detected for many images and need to be removed in analysis.

**Data Cleanup:** The height measurements from each sample must be post-processed in a standardized method to remove statistical inaccuracies and ensure reliable results. First, each instance was cropped to the same size ( $696 \times 696$ ) to exclude height values the microscope recorded off the samples. For each instance, the 1<sup>st</sup> and 99<sup>th</sup> percentile height values were found and any measurement in the instance that was outside this range was raised or lowered to the corresponding threshold to prevent statistical outliers from affecting the height range of each instance. Finally, height values from each instance had their 1st percentile subtracted to give every instance a common minimum of 0. This cleanup was done with the raw height data, before transforming it into an image.

**Height Image:** To use the height images as input to a DNN model we need to adjust the dimension. For this the post-processed data from each instance must be turned into an image with intensity values of 0-255. We divided each data point by the maximum height range found in our dataset before scaling by 255 to ensure the intensity value of each data point was on the same physical length scale. For this dataset, most height ranges were considerably smaller than the maximum as 160 of the 194 images have an intensity range less than 120 when linearly scaled, and 189 of the 194 have a range of less than 200. A piece-wise scaling function was applied to the intensity values

to improve contrast for TL. The scaling function in Figure 5-4 **Error! Reference source not found.** amplifies the growth rate of intensity values from 0-120 and decreases it for values from 120-255. Ultimately, an intensity of 120 is shifted to 200.

**Spectral Density Function:** The SDF of each image was calculated by performing a Fast Fourier Transform (FFT) on the post-processed data. A Hann window was applied after the FFT to dampen spectral leakage as the height data cannot be represented by a periodic function. The resulting SDF was then normalized by its maximum value and scaled logarithmically.

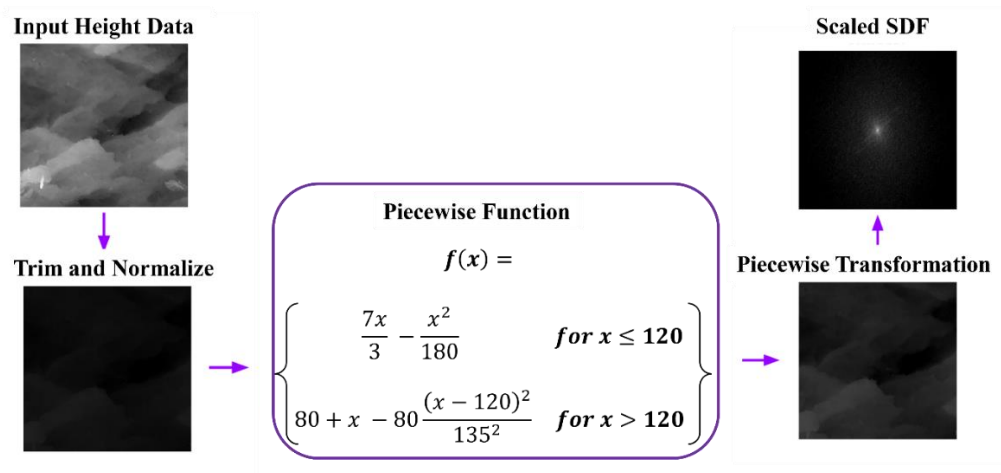


Figure 5-4: Visualization of post-processing steps for height images

### 5.2.3 Transfer Learning methodology using Pruning for Feature Extraction

In this section we introduce the proposed method to employ TL for extension of microstructure features critical for structure-property ML. Here we use a widely pre-trained model, VGG 19, as an example to how it can be employed for TL in the context of building structure-property relations. The network configuration of VGG 19 is shown in Figure 5-5 A. As the name

suggests the model consists of nineteen layers from which the first sixteen are convolution layers, and the remaining three are fully connected dense layers. These layers are divided into six blocks with the first five blocks having max-pooling at the end of each block. A block is visualized as the connected layers without having any space in between them, as depicted in Figure 5-5. As the total number of trainable parameters for VGG 19 are over 100 million, it will be impossible to train them on a small dataset. To transfer the knowledge of the pre-trained network, we can use the weights of the first sixteen layers and only train the last three layers (Figure 5-5 A). Using pre-trained weights of certain layers is commonly referred to as “*freezing* the layers”. Another approach of using VGG19 could be that only the first sixteen layers are used, but the last three layers are replaced by a totally different set of layers as seen in Figure 5-5 B. The customizations of pre-trained networks often require trial-and-error to obtain satisfactory ML results.

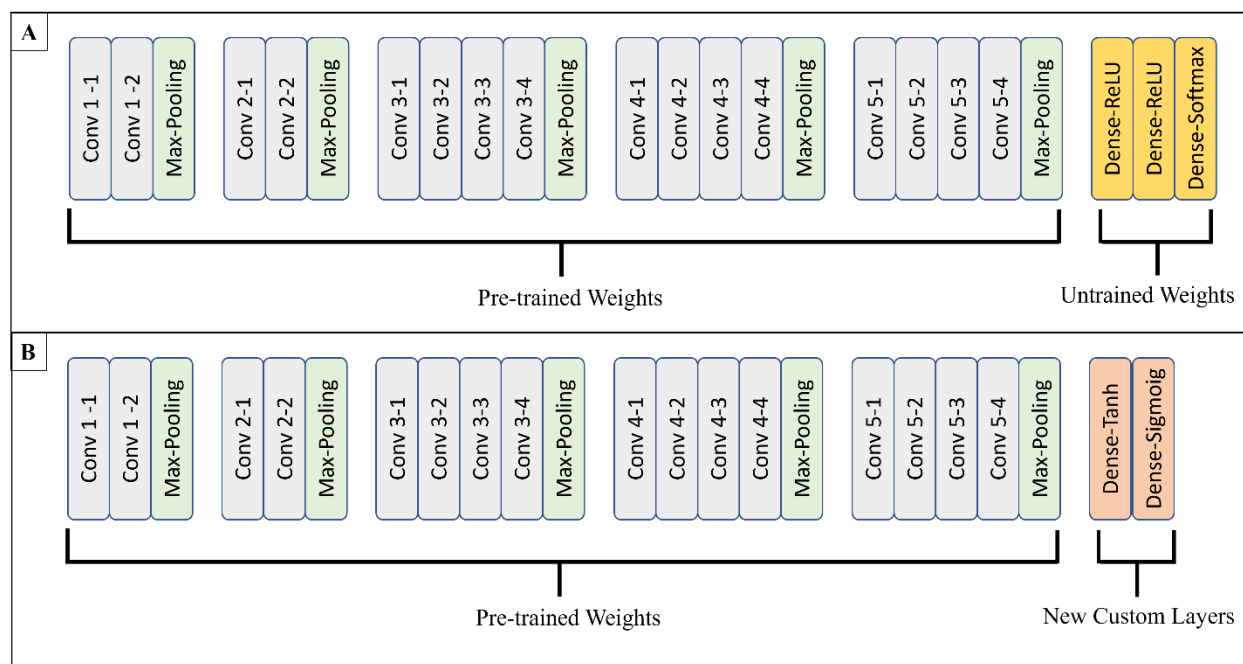


Figure 5-5: Examples of VGG 19 model customizations. The names of the layers are written inside the sub-blocks. (A) the weights of the first 16 layers are frozen, while the last three layers are trainable. (B) The first layers are used as in (A), but the last three layers are replaced with custom two layers.

Apart from simply modifying the final layers, alternate approaches can be applied to Transfer Learning. Since each layer and block extracts certain specific features from the models [133], it is possible to *prune* the model at any layer and extract only the features at that specific layer. Previous studies such as Zarski et al. [134] have already found pruning to be effective with CNNs in Transfer Learning applications. This process is referred to as pruning because it effectively cuts out the contributions of a pruned layer to the whole architecture [135]. In this sense pruning can be viewed as a form of compressions as it decreases the number of parameters in a model [136]. This method can also be used to remove the final layers of a model so that focus can be brought to the output of an intermediate layer. This intermediate layer can be any type of layer such as the pooling or convolution layers shown in Figure 5-5.

The use of pruning with Transfer Learning can be necessary at times due to a structural mismatch between the source task of the pre-trained model and the target task it is being transferred to [135]. This mismatch exists when the target task uses significantly less data than what the pre-trained model was trained on. However, there are tradeoffs to consider when determining how to prune a model. Pruning can remove unimportant weights so that a model avoids the risk of overfitting while becoming more relevant to its target task, but this also leads to a drop in the accuracy of the model [135]. One study by Gordon, Due, and Andrews [136] further explored this trade off and found that the ideal pruning amount was 30 – 40% before an increase in loss occurred. To ensure a pre-trained model is useful, some extent of its inductive bias from its pretraining must be maintained.

Different from past studies that are primarily focused on pruning only weights whereas this study prunes whole layers considering how filters behave in different convolution layers of any deep CNN. Filter identifies where certain features are present and produces a feature map indicating their locations [132]. The filters in the first layer focus on simple features such as edges, corners, and dots which vary depending on the surface texture of the material. The filters deeper into the model extract more complex and less visually interpretable features [132]. This is illustrated in Figure 5-6 where the feature map becomes quite vague compared to the original image as we go deeper into the model. Why later feature maps become increasingly complex is because the filters in later layers are identifying patterns from the features maps provided by filters in the previous layers. For example, a filter farther in the model may combine the edge features found in the first filters to create patterns of shapes. The process of *pruning* can help us extract specific features from the model. If the feature under study is simpler, then the model can be pruned

at the start, whereas if the feature is more complex, then it has a higher chance of being characterized by deeper layers. As such this study will also consider how pruning to different layers affect the model's performance.

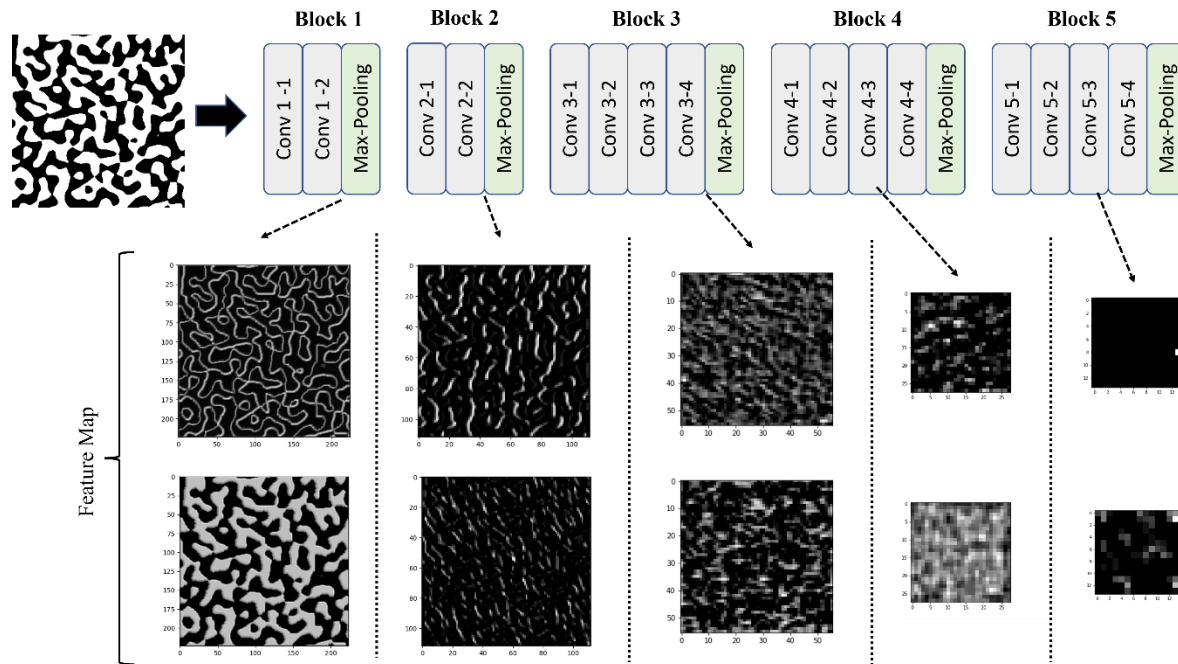


Figure 5-6: Features extracted from different layers in a pre-trained VGG 19 model with a sample input.

Another feature to consider when extracting features by pruning is the size of the output. Depending on where we prune the model, we can have different sizes. As seen in Figure 5-6, the output varies hugely. This high-dimensional output goes against the concept of transfer learning as this huge dimensional characterization will potentially require a huge dataset. The first step in reducing the dimension of these feature maps is to apply GlobalAveraging2D which is a built in function in keras [137], and computes one value from each filter. Thus, the output is reduced to the number of filters. For example, the output of Block 2 would just be of the size 128, and the output of Block 5 would be 512. However, these dimensions are still large enough to inhibit modeling on a small dataset because a general rule-of-thumb is to have data at least ten times the

dimension of input. To this end, we propose to apply Principal Component Analysis (PCA) to further reduce the characterization dimension. At the end, if we have roughly  $n/10$  parameters to represent the microstructure, then it is believed that a meaningful structure-property relationship can be built, where  $n$  is the number of datapoints.

Building on the transfer learning methodology introduced earlier, we present in Figure 5-7 our characterization framework for extracting the meso-scale features of fracture surface based on the structure-property relation. We start by  $N$  images of the fracture surface and input them into the transfer learning model. We prune the model as previously described at a certain block, and then extract the feature map at that location. After that we apply to GlobalAveraging2D to reduce the dimension to the number of filters at that location. To further reduce the dimension, we apply PCA. One can have different threshold levels for PCA to reduce the dimensionality. We recommend keeping the explained variance to around 70-80 % for PCA. Using the explained variance as a variable, we can further control the dimensionality of our input. Now that we have minimum possible parameters to represent the microstructure, we compute its property if it is a simulation or measure the property if it is an experiment. Using the reduced set of microstructure parameters as input and property values as output, we train multiple linear and non-linear regression models to see how well the model explains the variance in the data. Though primarily we could be looking at R-squared value, but other metrics such as RMSE should also be considered. We repeat the same procedure by pruning the pretrained model at a different location. This is done iteratively until we find the optimal pruning location, where the R-squared value is maximized. To mitigate the stochasticity and sample bias, we can repeat the regression part with different training and testing datasets. In this study, we repeat the train-test split along with PCs to

property regression thirty-five times. This number is a balance between the computational cost and reliability of our results.

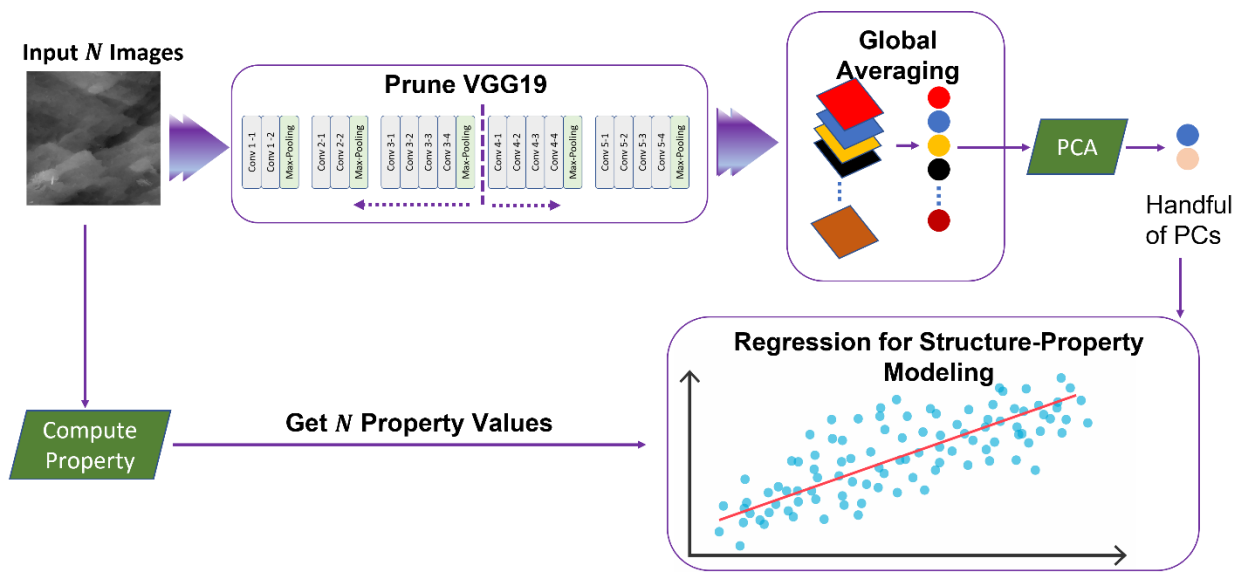


Figure 5-7: Framework for extracting microstructure features using pruned Transfer Learning models.

## 5.3 Result and Analysis

### 5.3.1 Artificial Dataset

To study the efficacy of our approach to characterize microstructure, we present a test example in this section. The idea is to create artificial digital microstructures, compute their properties and apply the proposed framework to observe the effect of pruning and optimizing a pretrained model. To create artificial microstructures, we use the reconstruction capabilities of SDF [15]. The backbone of SDF is Fourier transform (FT). Just like FT decomposes a waveform into sum of sinusoids of different frequencies, SDF decomposition of microstructures would represent its dominant microstructural features. A simple shape of SDF has been used which can

be thought of as a step-function having two primary tunable parameters as seen in Figure 5-8:  $W$ , which is the width of the peak, and  $P$ , which is the index of the start of the peak. We can use  $W$  and  $P$  to reconstruct microstructures having very different shapes as seen in Figure 5-9.

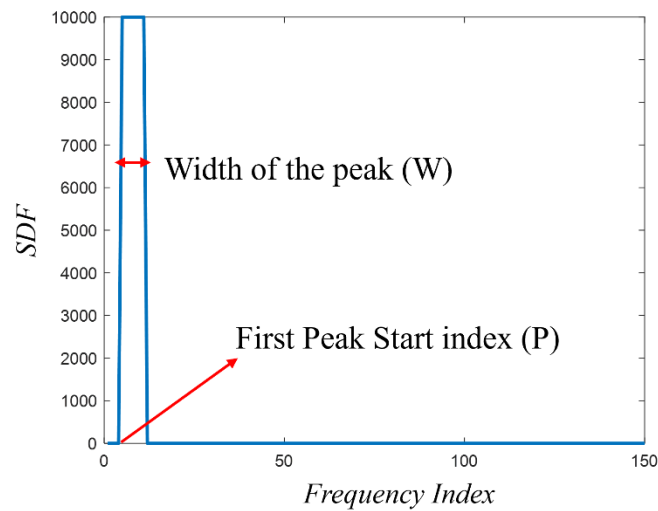


*Figure 5-8: Shape of SDF used to reconstruct artificial microstructures.*

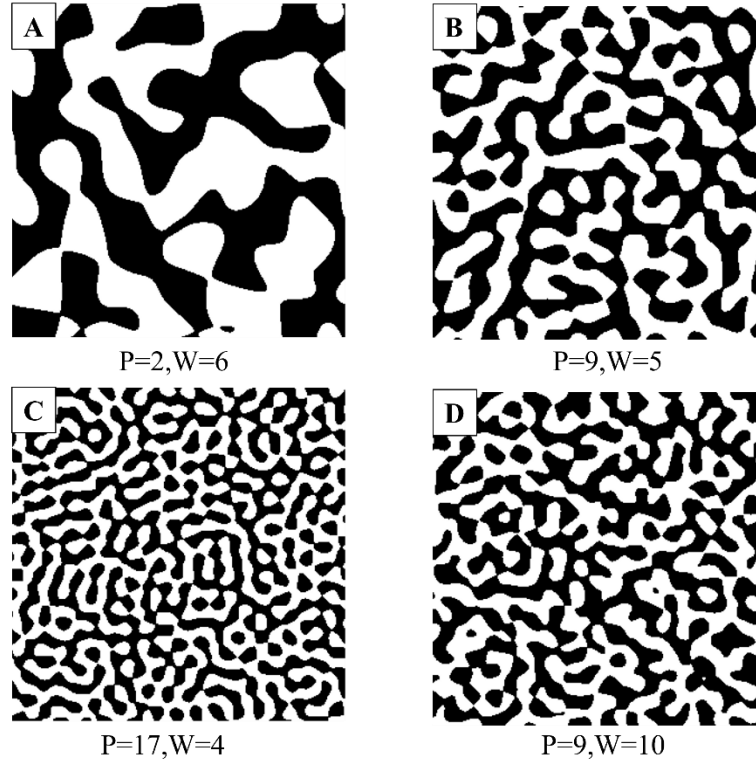


Figure 5-9: Unique artificial microstructures created from different SDFs which are controlled by two tuning parameters  $W$  and  $P$ .

The property of interest for this test example is optical absorption associated with solar cell design which takes a scalar value between 0 and 1. It is calculated using the Rigorous Couple Wave Analysis (RCWA) as detailed in [12]. For more details on RCWA the readers are directed to [138]. To summarize, the input for our model will be the microstructure image and the output is a scalar value representing 2D material property. To build the structure-property prediction model, we created a dataset of 224 artificial microstructures and their corresponding properties, split into training and test set with the ratios 80% : 20%.

Next, we implement the pruning technique introduced in Section 5.2.3. The level of variation explained by principal components was set to 99% and that controlled the number of principal components at a pruning location. Table 5-2 shows a few representative prediction results of the

model. As can be seen, the best model is given by the pruning location: *Block3\_Pool 1* which leads to a test r-squared accuracy of 0.9. It is also evident that as we move deeper into the model, the number of principal components increase for this material type. A big jump is evident from Block 3 to Block 4 in the number of principal components and that may have played a big role in the loss of accuracy in the model. Because a small dataset of 156 training images is not sufficient to train 43 parameters using regression. It is also noted that the best achievable r-squared accuracy is from the Random Forest regression method. This suggests that the underlying model has non-linearity.

*Table 5-1: Test R-squared results for different pruning locations. The results are color coded with green being good and red being worse and yellow in-between.*

<b>Pruning Location</b>	<b>Number of PCs</b>	<b>Random Forest</b>	<b>Lasso</b>	<b>Ridge</b>	<b>Gradient Boosting</b>
Block1_Pool	1	0.72	0.43	0.22	0.74
Block2_Pool	4	0.80	0.74	0.76	0.85
Block3_Pool	5	0.90	0.8	0.82	0.82
Block4_Pool	43	0.75	0.82	0.66	0.8
Block5_Pool	78	0.66	0.72	0.53	0.78

Next, we try to test the limits of our approach by decreasing the size of the dataset. We tried four different dataset sizes: 224, 100, and 50. For each of these datasets we run the regression 35 times at the pruning location identified from the previous exercise with the large dataset. As mentioned earlier, the repetition is to cater for stochasticity and data bias. The results are shown in Table 5-2. It is evident that the accuracy (test R-squared value) decreases with decrease in data size. Another important observation is that the decrease in accuracy is very subtle when the dataset is decreased to 100 images from 224 as the best test R-square value changes from 0.812 to 0.793. However, decreasing further to 50 results in a big loss of accuracy as the test R-square value

changes from 0.793 to 0.4999. We note that even with just 100 images we were able to build a predictive model with average test r-squared accuracy of 0.793. This shows the robustness of the methodology even for a very small dataset. It should be noted that, besides data size, the accuracy is expected to depend on the complexity of a microstructure and the nature of its relationship with the property. In this case, the structure-property relation is relatively straightforward link, and the property is solely dependent on microstructure.

*Table 5-2: Test r-squared values of predictive models with varying total number of images. The results are color coded with green being good and red being worse.*

Number of Images	Random Forest	Lasso	Gradient Boosting	Ridge
224	0.812	0.662	0.623	0.808
100	0.793	0.563	0.434	0.792
50	0.499	0.311	-0.842	0.403

### 5.3.2 Experiment Dataset – Silicone Rubber

In this section, we first describe the observed mechanical behavior of our test specimen, silicone rubber in the designed fatigue test and explain the important mechanical parameters to be included as features for model training purposes. Then, we apply the methodology introduced in early section to perform two main tasks for silicone rubber: (i) To analyze the surface and calculate correlations of crack surface with different properties, and (ii) To build a predictive model that can estimate the mechanical conditions responsible for the fatigue crack propagation.

#### 5.3.2.1 Experimental Data Interpretation

A complete experimental analysis of the same dataset can be found in [124]. Its mechanical behavior is summarized in short in this section, which can all be found in detail in [124]. The cyclic displacement will generate hysteresis loop on a stress-strain plot, with the area between the loading and unloading curve showing the amount of energy dissipation.[124] From the small strain regime of the loading curve during the cyclic displacement, the effective elastic modulus  $E$  can be obtained from the slope of the stress-strain curve. The modulus  $E$  decreases with the increase of strain amplitude due to the Mullins effect [124] and can be thought to be related to the concentration of bonds/matrix-filler interactions required to be damaged for fatigue crack propagation. The fatigue fracture behavior is described by plotting the crack propagation speed  $\frac{da}{dn}$  (nm/cycle,  $n$  is cycle number) as a function of the input energy  $\Gamma$ . In [124] we further proposed to plot the crack speed  $\frac{da}{dn}$  as a function of  $\mathcal{G}$  as the stored elastic energy at the crack tip. The silicone rubber fatigue data points overlaid onto a power law relation at room temperature (22° C) with a power law index of 1.5, while the high temperature data points deviated from the power law relation:

$$\frac{da}{dn} = a_0 \left( \frac{\mathcal{G}}{Eh_0} \right)^{1.5}$$

This deviation can be correlated with the corresponding fracture surface morphology differences.[124] The extent of deviation is quantified by an arbitrary pre-factor  $a_0$  with a unit in microns. Here, crack surface height profile, strain and temperature are selected for training, mainly because they are the easiest observable environmental parameters when a prediction is needed based on the crack surfaces. In addition,  $\frac{da}{dn}$ ,  $E$  and  $a_0$  are selected as important features for correlation analysis as they are shown to be the most representative to describe a fatigue process.

### 5.3.2.2 Structure-Property Correlation Analysis

The main objective of this study is to quantify the relationship of different features with the three properties of interest:  $\frac{da}{dn}$ ,  $E$ , and  $a_0$ . In the author's hypothesis there are two different features of interest as mentioned in Figure 5-1: meso-scale and micro-scale. To capture the effects of each scale, we built three different types of regression model based on the framework introduced in Figure 5-7. In one type of model, the input is only the height images from the experiments. In the next model, the input is the SDF of the height images. And in the last model, the input is the height image as well as the SDF of the height image. The output for all these models are the aforementioned three properties of interest. We repeat the model building 35 times for each model using six different regression techniques to ensure we can capture different complex relationships and cater for shortcomings of any single regression model. We focus on the average R-squared value as well as the standard error of R-squared value from these models. The results are presented in Table 5-3 below.

It is observed that with the height image as input, we can have an average R-squared value as high as 0.6357 for  $\frac{da}{dn}$  with standard error around 0.03 using ridge regression. This means that the height images alone can explain 64% variation in the  $\frac{da}{dn}$  with 95% confidence interval of  $\pm 6\%$ . For the elastic modulus  $E$ , the best average R-squared value is 0.2895 which shows a lower correlation. Lastly, for  $a_0$  The best average R-squared value is 0.55 using Gaussian Process. This shows that the underlying relationship is highly non-linear.

As shown in Table 5-3 , when we build model using SDF as input then we observe that the best average R-squared value is decreased to 0.2993 and the standard error is increased to 0.0572.

This implies that the underlying relationship of  $\frac{da}{dn}$  with SDF is weaker than with height images.

We also observe that there is no correlation with the remaining two properties.

Table 5-3: Model accuracy results using the Transfer Learning framework with Height Image, SDF, and both combined as inputs. The results are color coded with green being good and red being worse. Some results are omitted because the results were too bad and skewed the color scheme.

		Average Test R-squared						Std Error of Test R-squared					
		RF	Lasso	Ridge	GB	GP	Linear	RF	Lasso	Ridge	GB	GP	Linear
Height	$\frac{da}{dn}$	0.2888	0.5762	0.6357	0.3646	0.3528	0.5332	0.1322	0.0442	0.0308	0.0557	0.0555	0.0690
	$E$	0.2374	0.1907	0.2895	-	0.0480	0.1290	0.0651	0.0899	0.0508	0.0839	0.1011	0.0888
	$a_0$	0.1505	-	0.2457	-	0.5496	-	0.1490	0.2268	0.1413	0.5940	0.0732	0.4707
SDF	$\frac{da}{dn}$	-	0.0370	0.2993	0.1743	-	0.1509	0.1413	0.1362	0.0572	0.0386	0.1537	0.1110
	$E$	-	-	-	-	-	-	0.3868	0.2191	0.1236	0.1051	0.2702	0.1142
	$a_0$	-	-	-	-	-	-	-	-	0.2108	0.4773	-	-
SDF + Height	$\frac{da}{dn}$	0.5049	0.4563	0.3475	0.4291	0.2920	0.6961	0.0462	0.1069	0.1769	0.0638	0.0663	0.0246
	$E$	0.0728	-	0.3108	0.2089	-	0.1654	0.0842	0.1347	0.0709	0.0548	0.1859	0.0945
	$a_0$	-0.243	-0.581	-0.013	0.506	-0.185	0.105	0.511	0.550	0.318	0.082	0.447	0.159

In the last model, we combine both inputs to verify whether there is some unique information in each of height image and SDF. Since the best R-squared values is highest at 0.6961 for  $\frac{da}{dn}$ , it is evident that there is some unique information which has increased the model accuracy overall. Apart from the average R-squared value, the standard error is also lowest at 0.0246 which shows that it is a much more robust model and less susceptible to changes in data. The best average R-

squared value for  $E$  also increases which further strengthens the case of SDF capturing unique information which is not captured by the feature extraction of the raw height image using Transfer Learning. For  $a_0$ , we observe that R-squared values are lower than the first model. This is perhaps because of the small dataset size and the increase in predictors. If the new predictors do not add value to the model, then the accuracy of the model can be affected negatively in the case where the dataset is limited.

In the above analysis we perform a quantitative analysis on the relationship of microstructure features with the properties of a crack surface for the first time in the author's knowledge. The authors acknowledge that the R-squared values may differ if there was a much larger dataset, but as is the case with most material science problems we usually have a small dataset to study. This study primarily acts as test-bed example of the framework. In future, we could replicate this study on another material having a very large dataset and then we can also study the effect of the size of the dataset.

### 5.3.2.3 Predictive Model

The primary objective of this study is to build a predictive model which can accurately estimate a given property only with height image and environmental conditions as an input. This can be critical for forensic analysis of crack surfaces. To find the model with the best input, we employ a stepwise linear regression.

We start by building a model using the same framework as in the previous section. In the first model, we used only the height image as an input. We then added environmental features such

as temperature and strain and observe the prediction accuracy. The results are tabulated in Table 5-4. We note that when we add temperature along with height as input the average R-squared value for  $\frac{da}{dn}$  increases but for the other two, it decreases. This is perhaps because the temperature is not adding significant value in addition to the height image for the other two properties. If we add strain to the height image, we notice that prediction accuracy increases for all properties. The best model is the one which has all the features i.e., height image, strain, and temperature. The best average R-squared values are 0.85, 0.79, and 0.72 for  $\frac{da}{dn}$ ,  $E$ , and  $a_0$ , respectively.

Table 5-4: Model Accuracy results for the different predictive models having different inputs.

		Average Test R-squared					
		RF	LASSO	RIDGE	GB	Gaussian	Linear
Height + Strain + Temperature	$\frac{da}{dn}$	0.6742	0.7720	0.8353	0.7946	0.7915	0.8504
	$E$	0.6565	0.7049	0.7903	0.7828	0.6394	0.7819
	$a_0$	0.2487	-0.2650	-0.0812	-0.0092	0.7181	-1.7368
Height + Strain	$\frac{da}{dn}$	0.4366	0.7308	0.7825	0.5233	0.6438	0.7721
	$E$	0.7266	0.7832	0.8190	0.7178	0.6020	0.8243
	$a_0$	0.2965	0.2247	0.1009	-1.2495	0.6307	-0.3179
Height + Temperature	$\frac{da}{dn}$	0.6313	0.5039	0.7276	0.4291	0.4946	0.7062
	$E$	0.0304	-0.0015	0.1447	-0.1895	-0.4644	-0.0069
	$a_0$	-0.1266	-0.8167	-1.3801	-0.6021	0.4272	-
Height	$\frac{da}{dn}$	0.2888	0.5762	0.6357	0.3646	0.3528	0.5332
	$E$	0.2374	0.1907	0.2895	-0.0053	0.0480	0.1290
	$a_0$	0.1505	-0.2076	0.2457	-0.5804	0.5496	-0.5831

Even with such a small dataset, we have successfully achieved accuracy of 0.85 test R-squared value. This shows the efficacy of transfer learning in doing prediction modeling for crack-

surface analysis and prediction. With a larger dataset, this value can be even higher, and thus it can be a very reliable tool for forensic analysis of crack surfaces.

#### 5.4 Summary

In this chapter, we explore the possibility of using Transfer Learning (TL) to augment crack-surface analysis of complex microstructures with limited image data, where complex morphology cannot be characterized by the widely used microstructure characterization techniques. To overcome the challenge that pretrained models in TL cannot necessarily be used directly for the required purposes as their weights are tuned for a specific purpose. To use TL for structure-property mapping, we propose to manually prune the pre-trained model to retain the pre-trained weights of the convolution layers so that only a few weights of our custom layers are needed to extract relevant underlying microstructural features with limited data. The extracted features are determined based on how strongly they are correlated with the properties of interest.

We first apply this technique to a test dataset for which the microstructures are created using the spectral density function (SDF) and the optical property is calculated by physics-based simulations. Even on a small dataset of 224, we were able to achieve 90% test R2 value, demonstrating the effectiveness of our approach. Next, we apply the framework on the crack surface of silicone rubber to achieve two goals: (i) to analyze the surface and calculate correlations of crack surface with different properties, and (ii) to build a predictive model that can estimate the input conditions responsible for the crack surface. For (i), for the first time we are able to quantify the relationships between the two microstructure features (meso-scale and micro-scale) with properties of interest associated with fatigue fracture behavior. For (ii), we build predictive models using height images, strain, and temperature, which gives us test R2 accuracy of 0.85. This

accuracy is achieved with only 194 images of which only 70% are used as training. This shows the efficacy of our approach. With more data, we anticipate building an even more accurate model.

Thus, this study acts as a testbed to use TL for microstructure analysis and prediction. Some limitations include the complexity of the microstructure and its relationship to the property of interest. If the microstructure is too complex, or if it is hard to distinguish one from the other, then it will require a lot more data to train. And it is obvious that the properties of interest should have an underlying relationship with the microstructure in order to perform the analysis.

## Chapter 6 Conclusions and Future Work

### 6.1 Contributions

To facilitate the creation of P-S-P relations as well as the design of complex microstructural material systems, the overarching contribution of this work is to develop and enhance microstructural analysis techniques as presented in Chapter 1. We have developed (i) a computational structure – property model to estimate OPVC performance, (ii) an efficient three-phase microstructure reconstruction tool using SDF, (iii) an SDF based design framework to optimize materials such as solar cells, (iv) a metric which quantifies the dissimilarity between granular microstructures, (v) a model calibration framework using dissimilarity score for granular microstructure simulations, and (vi) a transfer learning based technique to perform analysis, and build predictive models, for complex microstructures.

The prominent research contributions made in each chapter are summarized as follows:

- a) In Chapter 3, we start by studying the relationship between SDF and physical descriptors which gives us insight into the different changes in shapes of SDF. Next, we extend the use of SDF for efficient reconstruction of three-phase microstructures. Lastly, we introduce an SDF-based design framework to find optimal processing conditions of any quasi-random material. To demonstrate the efficacy of our framework, we use OPVC as an example material system to optimize its incident photon to converted electron (IPCE) ratio. To efficiently implement the framework, we use coarse grained molecular dynamic (CGMD) simulations to bypass the costly experiments. Furthermore, to balance the accuracy and

efficiency of CGMD simulations, we modify the original SDF framework to present a multi-fidelity version of it.

- b) In Chapter 4 we extend the use of chord length distributions (CLD) by modifying it to characterize granular microstructures efficiently. Leveraging this modification, we present a novel dissimilarity metric, Dissimilarity Score (DS), that can quantitatively differentiate between granular microstructures. Building on this quantified difference of granular microstructures, we present a framework for calibrating the granular microstructure simulation parameters. Using Inconel 625 alloy as an example, we demonstrate the efficacy of our framework by calibrating the Cellular Automaton simulation parameters. We used NIST testbed data as ground truth to validate our work. In the same chapter, we present a framework to build P-S-P mapping of additively manufactured alloys. We show encouraging results of P-S mapping but could not complete the S-P mapping because of inaccurate property simulation.
- c) In Chapter 5, we modify and apply the Transfer Learning approach to characterize complex microstructures which cannot be characterized by other methods such descriptors or SDF. We show the effectiveness of characterization by pruning a pre-trained model on a artificial dataset. We further study the effect of data size on the accuracy of the structure-property model. Lastly, we use the presented technique on actual data of Silica Rubber for (i) novel quantitative analysis of crack-surface to quantify relationship with different properties, and (ii) building a predictive model that can estimate the environmental conditions which resulted in a particular crack-surface.

## 6.2 Future Work

There are several open-ended questions and opportunities identified during the formulation of this dissertation. Some of them are described below:

- a) So far in this dissertation, the focus had been to use 1D SDF for isotropic materials as SDF efficiently reduces the design space of such materials. However, for anisotropic materials there is no method out there that can reduce the 2D representation of SDF to a lower order. Iyer et.al. [15] have presented a simple approach to characterize as well as reconstruct anisotropic materials using SDF. However, these materials are aligned in a particular direction, but that is not necessarily the case for some of the material systems out there e.g., in the case of crack surfaces [121], there is no directional preference and yet the overall microstructure is anisotropic. One such possibility is using convolution neural networks to directly use these anisotropic SDFs similar to how Ieracitano et.al. used in their study [139]. But this approach restricts design and lacks interpretability. For design, GANs [131] could be used to create custom SDFs, but interpretability is a more challenging problem to solve.
- b) The Structure-Property map could not be built in Chapter 4 because of the erroneous property data. The error originated from the assumption about the RVE: DFT-based property calculation assumes that microstructure is isotropic which is not the case in that small size of simulation. But if the size of simulation is increased, the number of data points decreases, and the calculation time increases. To overcome the effect of data reduction, more simulations can be performed i.e., a few more single-track walls can be simulated to augment the data. However, there is no obvious solution for overcoming the cost of simulating the properties of this dataset. Once we have larger RVE, even the

characterization using CLDs would be much more accurate since there will be more boundaries to detect.

- c) The granular microstructure simulation framework presented in Chapter 4 was implemented on a very small dataset from NIST. One out of 3 images was treated as a test image. This creates data bias i.e., depending on the data to be separated for test, the results could be very different. To be more confident on the proposed approach, it should be applied on a larger dataset so that a few images could be separated out as a test set. Additionally, the current images from NIST have visual defects (grain boundaries), and these can create noise in the data. A post-processing should be performed on all the ground truth images to remove these twin boundaries.
- d) The entire dissertation has focused on characterizing microstructures with the assumption that the microstructures are devoid of any defects. Whereas this is not the case for many material systems. In literature a lot of work has been done to characterize defects separately [140,141], but there is a need to characterize microstructure features along with defects to represent the microstructure holistically. In most design scenarios, we do not just want to characterize the microstructure, but also reconstruct it. The reconstruction of such a microstructure would be even more challenging. Akin to how this thesis is divided into three different material types, there would be different solutions to characterize and reconstruct different material types with different types of defects.
- e) For the characterization of crack-surfaces in Chapter 5, we have used Transfer Learning technique. Based on the popularity, we directly used VGG19 architecture as our underlying pre-trained neural network. However, there exist many other pre-trained model for different purposes [142] that could have also been used. In fact, there is a possibility that

another pre-trained model could have provided a better accuracy for characterizing the complex crack-surface. This possibility needs to be explored by trying multiple pre-trained models and comparing their accuracy. Moreover, these multiple models could be modified, or pruned, in various ways this increasing the number of choices for feature extraction many-folds. Thus, an efficient automated method similar to *AutoML* [143] tools could be developed to automate the process of feature extraction by quickly checking through multiple pretrained model options.

This thesis contributes to the current MCR techniques by expanding the understanding of current tools, developing new tools for MCR, as well as employing novel uses of current established and developing techniques. As MCR techniques are material dependent, this thesis primarily focuses on three general material types: continuous, granular, and complex microstructures. These contributions are expected to directly help in the design of such material systems as well to provide the scientific community with diverse ideas of using MCR to accelerate computational material design for all materials.

## Appendix

### A.1 Nanomine Repository

Developing and understanding a tool that can help other scientists is one thing but bringing it to their doorsteps in a very user-friendly way is a totally different feat. Keeping in view the accelerated materials development [2] framework, it is extremely important that all the data and related tools are made available universally. Towards this goal, SDF is incorporated as one of the MCR tools on the NanoMine portal.

With the advent of Materials Genome Initiative (MGI) in the United States and a similar focus on material development around the world, quite a few materials data repositories and tools have been made available online [144–147]. While most of these repositories concentrate on computational data, NanoMine [148] is an open source platform with the goal of storing and curating widely varying experimental data on polymer nanocomposites. The information stored from papers and other resources includes physical properties, microstructures, and processing conditions. The flexible data schema allows to incorporate data from other existing scientific metadata. Additionally, NanoMine also makes available tools to characterize and analyze the microstructure data which can be very useful in nanocomposite design. A collection of module tools for microstructure characterization & reconstruction and simulation software to model bulk nanocomposite material response augments knowledge generated by experimental data.

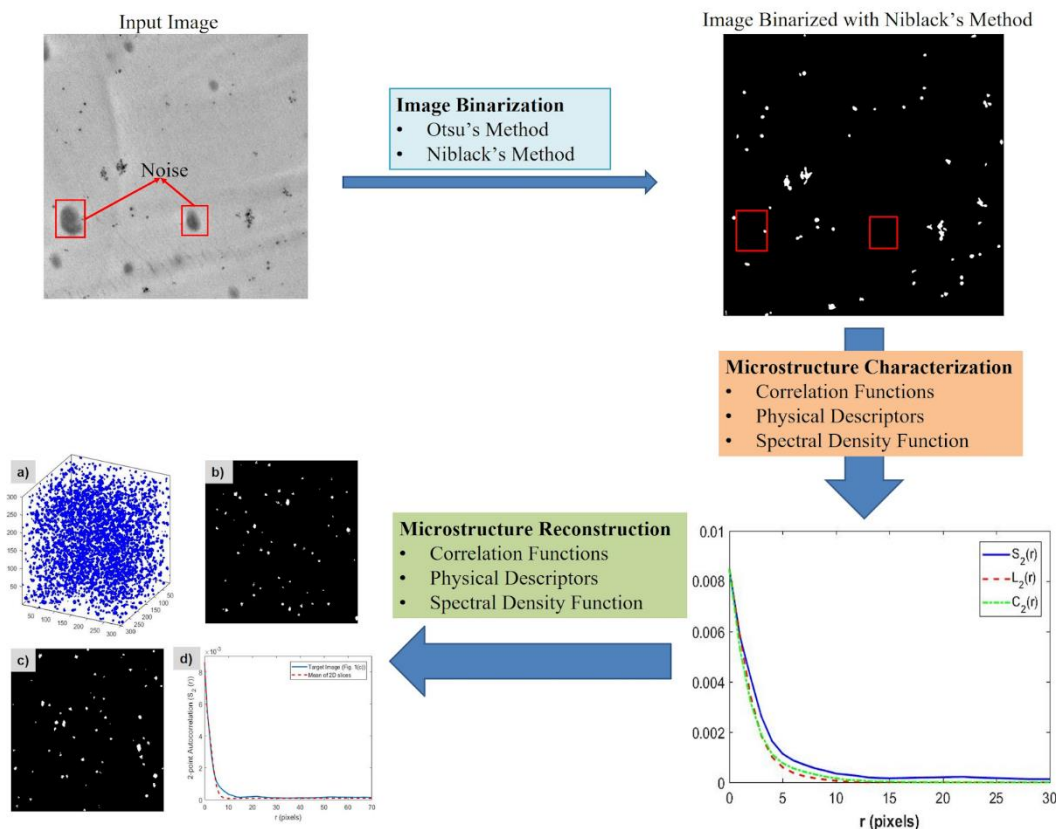


Figure A-1: The flowchart highlights the key features of MCR tools in Nanomine, starting from binarization of a TEM image using either of the two techniques (Otsu or Niblack). After that, the image can be characterized using the three broad methods (Correlation Function, Physical Descriptors, and Spectral Density Function). Lastly, a statistical equivalent of the microstructure image can be reconstructed in 2D or 3D to enable FEA simulations.

The MCR techniques developed in IDEAL lab have been incorporated into NanoMine to provide parsimonious microstructure analysis workflow for researchers as shown in Figure A-1. We provide two popular binarization tools namely, Otsu's Method [149] and Niblack's Method [150], as well as three microstructure characterization and reconstruction techniques: correlation function, physical descriptors, and spectral density function. These MCR techniques are applicable to two-phase, isotropic nanocomposites. They provide quantitative descriptors of the structure that can be used for data comparison or analysis.

Each tool is accompanied by detailed instructions on how to interact with the tool as well as recommendations for how to select tools best suited for their microstructure. The newly added “Intelligent Characterization” tool selects the most suitable characterization method between the “physical descriptors” [151] –and the SDF approaches based on analyzing the user uploaded image(s). The example result in Figure A-2 shows that SDF is preferred over physical descriptors for this particular microstructure. Characterization results such as those shown in Figure A-2 (c), generated on SDF parameterization, can be easily passed to the NanoMine Database for subsequent use in machine learning and other data mining procedures.

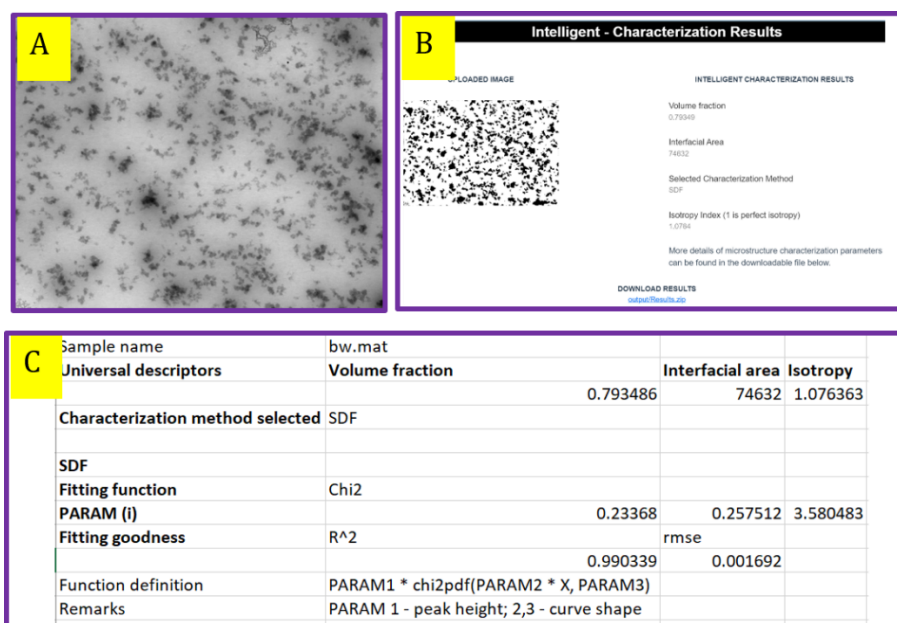


Figure A-2: (A) Transmission electron microscopy (TEM) image of a (B) The results page of Intelligent Characterization using the input image in (A) shows the binarized image as well as some basic information; (C) The output (downloadable excel file) containing detailed description of the SDF parameters.

The MCR tools can also be used for reconstructing statistically equivalent 2D or 3D images for a given isotropic microstructure image. Figure A-3 shows an example of the result page for

microstructure reconstruction using the physical descriptor-based method. Minor discrepancies of the two correlation functions (original versus reconstructed) are contributed by the noise in the original image and the approximation introduced by using the descriptors. Such reconstructed images can serve as inputs to structure-property simulations to predict material behavior and therefore are key components of material design workflows.

Our MCR tools have several user-friendly features that make these tools attractive for researchers. For example, all computations are performed on the NanoMine server; all tools support commonly used image file formats (PNG, JPEG and TIF) and the ability to analyze zip files containing a batch of images; and NanoMine provides e-mail alerts to users upon completion of their requests. Our system's capability of storing and characterizing multiple (batch of) images from the same material sample is very useful for understanding the material heterogeneity and providing an informative statistical description.

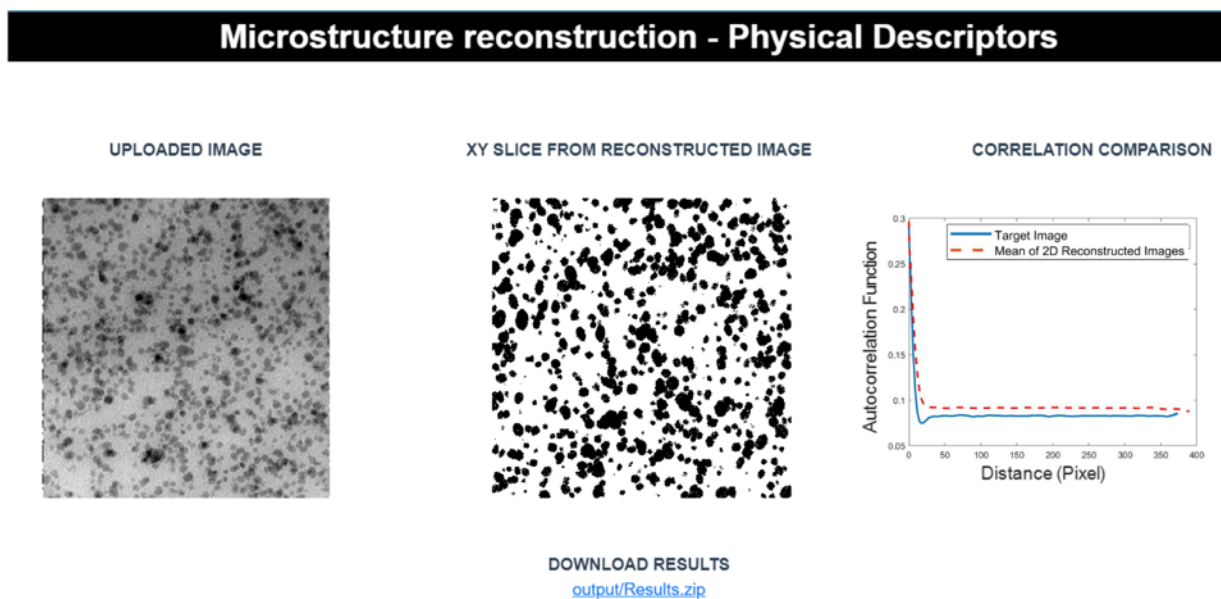


Figure A-3: TEM Image reconstruction using Nanomine. (Left) TEM micrograph of silica in poly (ethylene oxide) (Middle) One 2D slice from the 3D reconstruction of the original image using Physical

*Descriptor technique. (Right) Comparison of two-point correlation functions between reconstructed and original (target) images.*

## A.2 Three-phase characterization and reconstruction

The material systems studied in the previous sections were purely two-phase, i.e., each element of the microstructure consisted of either one phase or the other. In this section the SDF study was advanced to incorporate and aid in the characterization and reconstruction of materials that consist of three phases. The material system under study is Organic Photovoltaic Cells (OPVCs).

OPVC materials are generally regarded as two-phase materials i.e. donor and acceptor [152,153] (see Figure A-4 (a)), but there is also evidence of a third phase [154] which may behave slightly differently. If there were to exist a third phase, then we can assume that this phase would be placed like an interphase, i.e., it would occur at the boundary of the two materials. Arbitrary thresholding was done on an analogue XSTM image of OPVC specimen to create a three-phase microstructure image (Figure A-4 (b)).

From literature, one way to characterize a three-phase microstructure is to use any three independent two-point correlation functions from the nine available [155]. The nine available two-point correlation functions for any three-phase material are:  $P_{11}, P_{12}, P_{13}, P_{21}, P_{22}, P_{23}, P_{31}, P_{32}, P_{33}$ . The three auto-correlations ( $P_{11}, P_{22}, P_{33}$ ) are fairly easy to calculate using SDF because of the relationship mentioned in Section 2.1. The problem, however, is to calculate the remaining cross-correlation functions efficiently because the traditional brute-force method is very expensive especially if it used inside a simulated-annealing reconstruction.

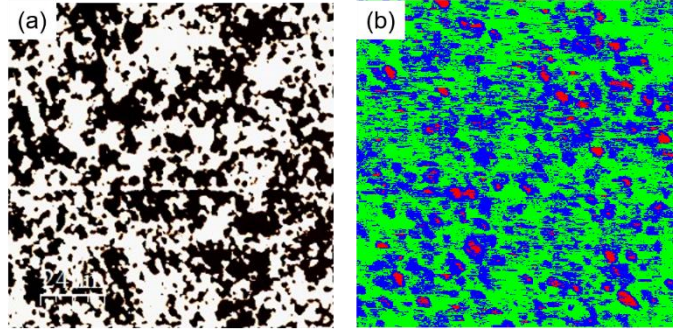


Figure A-4: (a) is a binarized XSTM image of a sample of OPVC material, (b) is the three-phase image obtained after arbitrarily adjusting the threshold of the XSTM image.

Using available information on SDF, Fast Fourier Transform (FFT) and their relationship, a new FFT-based method is developed in this work to calculate the SDF equivalent of a cross-correlation function such as  $P_{21}$ .

Comparing the definition of two-point correlation function from [156] :

$$f_2(h, h' | r_t) = \mathfrak{I}^{-1}[\overline{\mathfrak{N}_k^h} \mathfrak{N}_k^{h'}], \quad (6-1)$$

Where  $\mathfrak{N}_k^h = \mathfrak{I}(M_s^h)$ ,  $\overline{\mathfrak{N}_k^h}$  is the complex conjugate of  $\mathfrak{N}_k^h$ , and  $h$  donates the phase and [10]:

$$S_2(r) = \mathfrak{I}^{-1}(\rho(k)) = f_2(h, h' | r_t), \quad (6-2)$$

where  $\rho(k)$  is the SDF, and  $h$  and  $h'$  are the same.

This leads to the relationship:

$$\rho^*(k) = \mathfrak{I}(M_1) * \mathfrak{I}(M_2), \quad (6-3)$$

which is named cross-SDF for ease of reference.

After the development of cross-SDF to cater for efficient calculation of cross-correlation function, now a sample microstructure is considered as a test case (Fig. 16 (b)). Because the blue phase, i.e., the interphase, always divides the other two phases, red phase will always lie inside of green phase. This implicit correlation leads to the hypothesis that only two correlation functions are sufficient to characterize and consequently reconstruct the three-phase material. But the definition of the two-phase will be slightly different from the original and intuitive understanding of a phase. As seen in Figure A-5, the microstructure is divided into three phases: phase 1 is the original green phase, phase 2 is the combination of blue phase and red phase, and lastly phase 3 is the red phase.

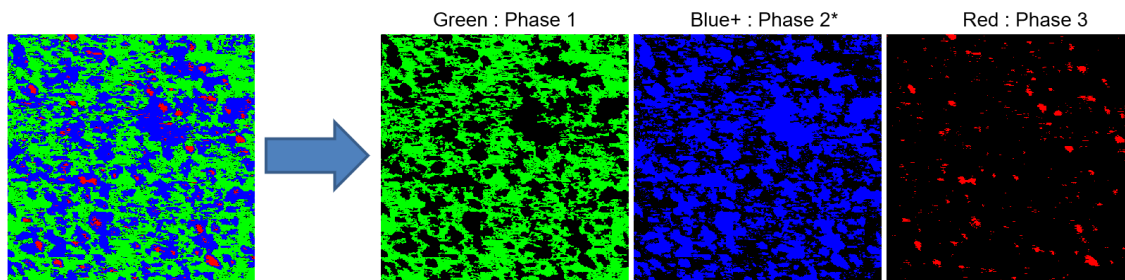


*Figure A-5: Three phase material is broken down into three phases.*

To characterize the microstructure, first the SDF of green phase is calculated which is equivalent of  $P_{11}$ . Next, the cross-SDF of blue and red phase is calculated as shown in Figure A-6. This concludes the characterization process for the three-phase material.

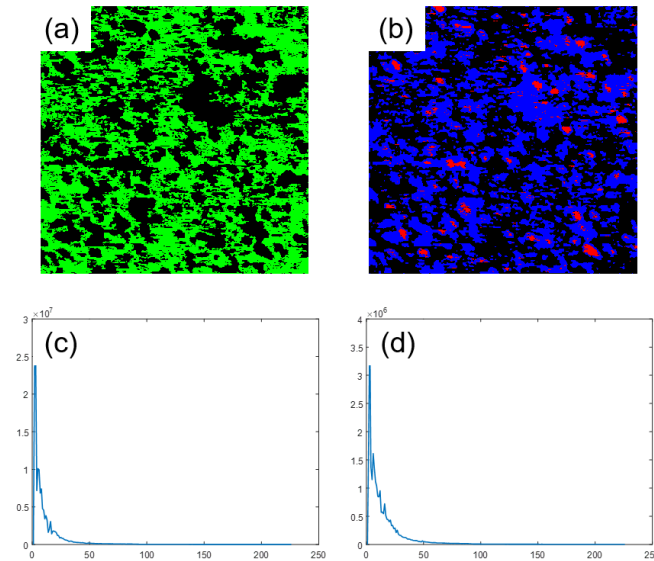


*Figure A-6: (a) is the green phase of the three-phase microstructure, (b) is the blue and red phase of the microstructure, (c) is the SDF of (a), and lastly (d) is the cross-SDF of blue and red phases.*

The strategy for the reconstruction of the three-phase microstructure is shown in Figure A-7. It involves first creating the green phase by using the SDF reconstruction method explained in section 2.1. In the next step, simulated annealing is done to place red particles inside the blue phase. The cost function used is the error of the cross-correlation function between the blue and the red phase. Lastly, both the images are coalesced into a three-phase microstructure.

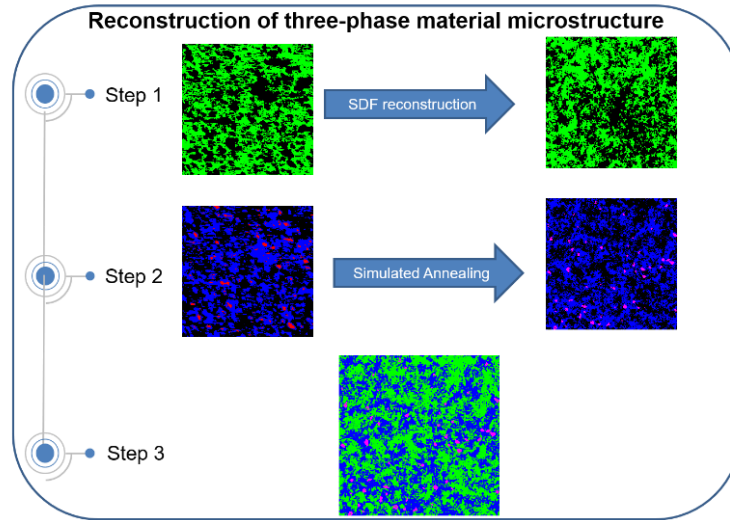


Figure A-7: The scheme for reconstructing a three-phase material microstructure.

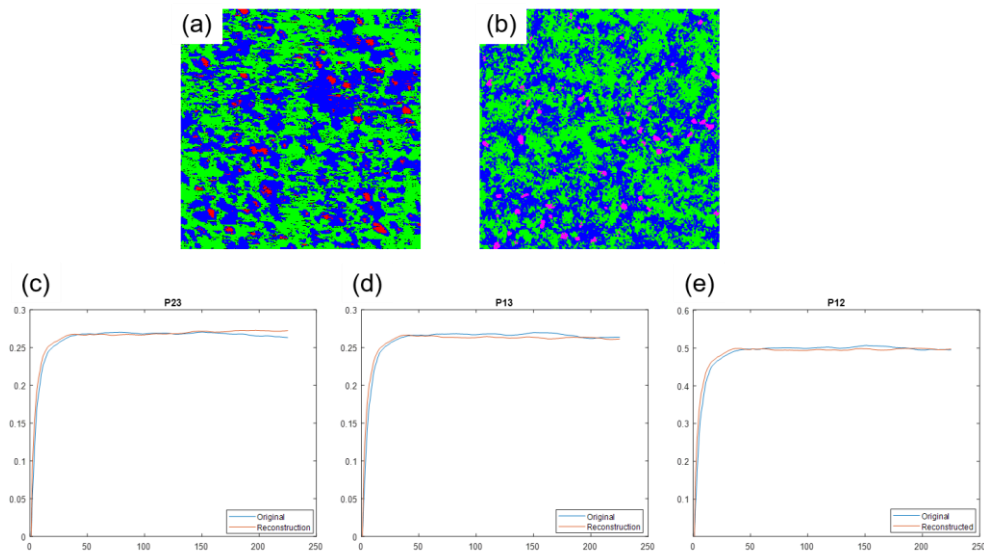


Figure 6-1: (a) is the original image. (b) is the reconstructed image. (c, d, and e) are the two-point correlation functions  $P_{23}$ ,  $P_{13}$ , and  $P_{12}$  respectively.

To verify the reconstruction, three of the nine available two-point correlation functions were selected which were not used in the reconstruction technique. They are:  $P_{13}$ ,  $P_{12}$  and  $P_{23}$ . Additionally, instead of using the efficient SDF based correlation functions, brute-force method was selected to calculate the correlation functions. The results (Figure A-8) show a good agreement

of the original image with the reconstructed image as per the three independent two-point correlation functions selected.

## References

- [1] Kalil Tom And Wadia, C., 2011, “Materials Genome Initiative for Global Competitiveness,” *Genome*, (June), pp. 1–18.
- [2] Correa-Baena, J. P., Hippalgaonkar, K., van Duren, J., Jaffer, S., Chandrasekhar, V. R., Stevanovic, V., Wadia, C., Guha, S., and Buonassisi, T., 2018, “Accelerating Materials Development via Automation, Machine Learning, and High-Performance Computing,” *Joule*, **2**(8), pp. 1410–1420.
- [3] Wang, C., Fu, H., Jiang, L., Xue, D., and Xie, J., 2019, “A Property-Oriented Design Strategy for High Performance Copper Alloys via Machine Learning,” *npj Comput. Mater.*, **5**(1).
- [4] Thostenson, E. T., and Chou, T. W., 2006, “Processing-Structure-Multi-Functional Property Relationship in Carbon Nanotube/Epoxy Composites,” *Carbon N. Y.*, **44**(14), pp. 3022–3029.
- [5] Smith, J., Xiong, W., Yan, W., Lin, S., Cheng, P., Kafka, O. L., Wagner, G. J., Cao, J., and Liu, W. K., 2016, “Linking Process, Structure, Property, and Performance for Metal-Based Additive Manufacturing: Computational Approaches with Experimental Support,” *Comput. Mech.*, **57**(4), pp. 583–610.
- [6] Fromm, B. S., Adams, B. L., Ahmadi, S., and Knezevic, M., 2009, “Grain Size and Orientation Distributions: Application to Yielding of  $\alpha$ -Titanium,” *Acta Mater.*, **57**(8), pp. 2339–2348.

- [7] Fátima Vaz, M., and Fortes, M. A., 1988, “Grain Size Distribution: The Lognormal and the Gamma Distribution Functions,” *Scr. Metall.*, **22**(1), pp. 35–40.
- [8] Fullwood, D. T., Niezgodá, S. R., Adams, B. L., and Kalidindi, S. R., 2010, “Microstructure Sensitive Design for Performance Optimization,” *Prog. Mater. Sci.*, **55**(6), pp. 477–562.
- [9] Ma, H. S., Prévost, J. H., Jullien, R., and Scherer, G. W., 2001, “Computer Simulation of Mechanical Structure-Property Relationship of Aerogels,” *J. Non. Cryst. Solids*, **285**(1–3), pp. 216–221.
- [10] Bostanabad, R., Zhang, Y., Li, X., Kearney, T., Brinson, L. C., Apley, D. W., Liu, W. K., and Chen, W., 2018, “Computational Microstructure Characterization and Reconstruction: Review of the State-of-the-Art Techniques,” *Prog. Mater. Sci.*, **95**, pp. 1–41.
- [11] Bargmann, S., Klusemann, B., Markmann, J., Schnabel, J. E., Schneider, K., Soyarslan, C., and Wilmers, J., 2018, “Generation of 3D Representative Volume Elements for Heterogeneous Materials: A Review,” *Prog. Mater. Sci.*, **96**, pp. 322–384.
- [12] Yu, S., Zhang, Y., Wang, C., Lee, W. K., Dong, B., Odom, T. W., Sun, C., and Chen, W., 2017, “Characterization and Design of Functional Quasi-Random Nanostructured Materials Using Spectral Density Function,” *J. Mech. Des. Trans. ASME*, **139**(7).
- [13] Lee, W. K., Yu, S., Engel, C. J., Reese, T., Rhee, D., Chen, W., and Odom, T. W., 2017, “Concurrent Design of Quasi-Random Photonic Nanostructures,” *Proc. Natl. Acad. Sci. U. S. A.*, **114**(33), pp. 8734–8739.

- [14] Farooq Ghumman, U., Iyer, A., Dulal, R., Munshi, J., Wang, A., Chien, T., Balasubramanian, G., and Chen, W., 2018, "A Spectral Density Function Approach for Active Layer Design of Organic Photovoltaic Cells," *J. Mech. Des. Trans. ASME*, **140**(11).
- [15] Iyer, A., Dulal, R., Zhang, Y., Ghumman, U. F., Chien, T. Y., Balasubramanian, G., and Chen, W., 2020, "Designing Anisotropic Microstructures with Spectral Density Function," *Comput. Mater. Sci.*, **179**, p. 109559.
- [16] Latypov, M. I., Kühbach, M., Beyerlein, I. J., Stinville, J. C., Toth, L. S., Pollock, T. M., and Kalidindi, S. R., 2018, "Application of Chord Length Distributions and Principal Component Analysis for Quantification and Representation of Diverse Polycrystalline Microstructures," *Mater. Charact.*, **145**, pp. 671–685.
- [17] Evans, J. C., Morgan, P. H., and Renaud, R. H., 1978, "Simulation of Electron Spin Resonance Spectra by Fast Fourier Transform. A Novel Method of Calculating Spectra to Include Isotopic Substitution, Superhyperfine Coupling, Instrument Time Constant and Modulation Broadening In," *Anal. Chim. Acta*, **103**(2), pp. 175–187.
- [18] Berrut, J. P., 1986, "A Fredholm Integral Equation of the Second Kind for Conformal Mapping," *J. Comput. Appl. Math.*, **14**(1–2), pp. 99–110.
- [19] Lim, J. S., and S., J., 1990, "Two-Dimensional Signal and Image Processing," ph.
- [20] Cooley, J. W., Lewis, P. A. W., and Welch, P. D., 1969, *The Fast Fourier Transform and Its Applications*.

- [21] Fullwood, D. T., Niezgoda, S. R., and Kalidindi, S. R., 2008, "Microstructure Reconstructions from 2-Point Statistics Using Phase-Recovery Algorithms," *Acta Mater.*, **56**(5), pp. 942–948.
- [22] Huang, J. S., Goldberg, W. I., and Bjerkaas, A. W., 1974, "Study of Phase Separation in a Critical Binary Liquid Mixture: Spinodal Decomposition," *Phys. Rev. Lett.*, **32**(17), pp. 921–923.
- [23] Huntington, M. D., Engel, C. J., Hryn, A. J., and Odom, T. W., 2013, "Polymer Nanowrinkles with Continuously Tunable Wavelengths," *ACS Appl. Mater. Interfaces*, **5**(13), pp. 6438–6442.
- [24] Ramakrishna Reddy, K. T., Koteswara Reddy, N., and Miles, R. W., 2006, "Photovoltaic Properties of SnS Based Solar Cells," *Sol. Energy Mater. Sol. Cells*, **90**(18–19), pp. 3041–3046.
- [25] Chiu, M. Y., Jeng, U. S., Su, C. H., Liang, K. S., and Wei, K. H., 2008, "Simultaneous Use of Small- and Wide-Angle X-Ray Techniques to Analyze Nanometerscale Phase Separation in Polymer Heterojunction Solar Cells," *Adv. Mater.*, **20**(13), pp. 2573–2578.
- [26] Furukawa, M., Horita, Z., Nemoto, M., Valiev, R. Z., and Langdon, T. G., 1996, "Microhardness Measurements and the Hall-Petch Relationship in an Al-Mg Alloy with Submicrometer Grain Size," *Acta Mater.*, **44**(11), pp. 4619–4629.
- [27] Fan, G. J., Choo, H., Liaw, P. K., and Lavernia, E. J., 2006, "Plastic Deformation and Fracture of Ultrafine-Grained Al-Mg Alloys with a Bimodal Grain Size Distribution," *Acta Mater.*, **54**(7), pp. 1759–1766.

- [28] Ni, J., and Incropera, F. P., 1995, “Extension of the Continuum Model for Transport Phenomena Occurring during Metal Alloy Solidification-II. Microscopic Considerations,” *Int. J. Heat Mass Transf.*, **38**(7), pp. 1285–1296.
- [29] Chen, S., Cai, W., Piner, R. D., Suk, J. W., Wu, Y., Ren, Y., Kang, J., and Ruoff, R. S., 2011, “Synthesis and Characterization of Large-Area Graphene and Graphite Films on Commercial Cu-Ni Alloy Foils,” *Nano Lett.*, **11**(9), pp. 3519–3525.
- [30] Turner, D. M., Niezgod, S. R., Kalidindi, S. R., and Woodruff, G. W., 2016, “Efficient Computation of the Angularly Resolved Chord Length Distributions and Lineal Path Functions in Large Microstructure Datasets.”
- [31] Wolff, S. J., Lin, S., Faierson, E. J., Liu, W. K., Wagner, G. J., and Cao, J., 2017, “A Framework to Link Localized Cooling and Properties of Directed Energy Deposition (DED)-Processed Ti-6Al-4V,” *Acta Mater.*, **132**, pp. 106–117.
- [32] Beckermann, C., Diepers, H. J., Steinbach, I., Karma, A., and Tong, X., 1999, “Modeling Melt Convection in Phase-Field Simulations of Solidification,” *J. Comput. Phys.*, **154**(2), pp. 468–496.
- [33] Kim, Y. T., Goldenfeld, N., and Dantzig, J., 2000, “Computation of Dendritic Microstructures Using a Level Set Method,” *Phys. Rev. E - Stat. Physics, Plasmas, Fluids, Relat. Interdiscip. Top.*, **62**(2 B), pp. 2471–2474.
- [34] Boettinger, W. J., Warren, J. A., Beckermann, C., and Karma, A., 2002, “Phase-Field Simulation of Solidification,” *Annu. Rev. Mater. Sci.*, **32**(1), pp. 163–194.

- [35] Liu, Z., Bessa, M. A., and Liu, W. K., 2016, “Self-Consistent Clustering Analysis: An Efficient Multi-Scale Scheme for Inelastic Heterogeneous Materials,” *Comput. Methods Appl. Mech. Eng.*, **306**, pp. 319–341.
- [36] Tan, L., and Zabaras, N., 2007, “A Level Set Simulation of Dendritic Solidification of Multi-Component Alloys,” *J. Comput. Phys.*, **221**(1), pp. 9–40.
- [37] Rodgers, T. M., Madison, J. D., and Tikare, V., 2017, “Simulation of Metal Additive Manufacturing Microstructures Using Kinetic Monte Carlo,” *Comput. Mater. Sci.*, **135**, pp. 78–89.
- [38] Zhang, Y., and Zhang, J., 2019, “Modeling of Solidification Microstructure Evolution in Laser Powder Bed Fusion Fabricated 316L Stainless Steel Using Combined Computational Fluid Dynamics and Cellular Automata,” *Addit. Manuf.*, **28**, pp. 750–765.
- [39] Xu, H., Liu, R., Choudhary, A., and Chen, W., 2015, “A Machine Learning-Based Design Representation Method for Designing Heterogeneous Microstructures,” *J. Mech. Des. Trans. ASME*, **137**(5).
- [40] Lomax, H., Pulliam, T., Zingg, D., and Kowalewski, T., 2002, “Fundamentals of Computational Fluid Dynamics,” *Appl. Mech. Rev.*, **55**(4), p. B61.
- [41] Abdolhosseini Qomi, M. J., Krakowiak, K. J., Bauchy, M., Stewart, K. L., Shahsavari, R., Jagannathan, D., Brommer, D. B., Baronnet, A., Buehler, M. J., Yip, S., Ulm, F. J., Van Vliet, K. J., and Pellenq, R. J. M., 2014, “Combinatorial Molecular Optimization of Cement Hydrates,” *Nat. Commun.*, **5**(1), pp. 1–10.

- [42] Rahimi-Aghdam, S., Bažant, Z. P., and Caner, F. C., 2017, “Diffusion-Controlled and Creep-Mitigated ASR Damage via Microplane Model. II: Material Degradation, Drying, and Verification,” *J. Eng. Mech.*, **143**(2), p. 04016109.
- [43] van Beek, A., Ghumman, U. F., Munshi, J., Tao, S., Chien, T. Y., Balasubramanian, G., Plumlee, M., Apley, D., and Chen, W., 2021, “Scalable Adaptive Batch Sampling in Simulation-Based Design with Heteroscedastic Noise,” *J. Mech. Des. Trans. ASME*, **143**(3).
- [44] Ghumman, U. F., Van Beek, A., Munshi, J., Balasubramanian, G., Chien, T., and Chen, W., 2021, “Two Stage Optimization of Organic Photovoltaic Cells Using Large Scale Coarse-Grained Molecular Dynamics Simulations.”
- [45] Niezgodá, S. R., Turner, D. M., Fullwood, D. T., and Kalidindi, S. R., 2010, “Optimized Structure Based Representative Volume Element Sets Reflecting the Ensemble-Averaged 2-Point Statistics,” *Acta Mater.*, **58**(13), pp. 4432–4445.
- [46] Drugan, W. J., and Willis, J. R., 1996, “A Micromechanics-Based Nonlocal Constitutive Equation and Estimates of Representative Volume Element Size for Elastic Composites,” *J. Mech. Phys. Solids*, **44**(4), pp. 497–524.
- [47] Xu, H., Liu, R., Choudhary, A., and Chen, W., 2014, “A Machine Learning-Based Design Representation Method for Designing Heterogeneous Microstructures,” *Proc. ASME Des. Eng. Tech. Conf.*, **2B**(5).
- [48] Bostanabad, R., Bui, A. T., Xie, W., Apley, D. W., and Chen, W., 2016, “Stochastic Microstructure Characterization and Reconstruction via Supervised Learning,” *Acta*

- Mater., **103**, pp. 89–102.
- [49] Bostanabad, R., Chen, W., and Apley, D. W., 2016, “Characterization and Reconstruction of 3D Stochastic Microstructures via Supervised Learning,” *J. Microsc.*, **264**(3), pp. 282–297.
- [50] Liu, X., and Shapiro, V., 2015, “Random Heterogeneous Materials via Texture Synthesis,” *Comput. Mater. Sci.*, **99**, pp. 177–189.
- [51] Cang, R., Li, H., Yao, H., Jiao, Y., and Ren, Y., 2018, “Improving Direct Physical Properties Prediction of Heterogeneous Materials from Imaging Data via Convolutional Neural Network and a Morphology-Aware Generative Model,” *Comput. Mater. Sci.*, **150**, pp. 212–221.
- [52] Yang, Z., Li, X., Brinson, L. C., Choudhary, A. N., Chen, W., and Agrawal, A., 2018, “Microstructural Materials Design via Deep Adversarial Learning Methodology,” *J. Mech. Des. Trans. ASME*, **140**(11).
- [53] HECHT-NIELSEN, R., 1992, “Theory of the Backpropagation Neural Network,” *Neural Networks Percept.*, pp. 65–93.
- [54] Kim, Y., Kim, Y., Yang, C., Park, K., Gu, G. X., and Ryu, S., 2021, “Deep Learning Framework for Material Design Space Exploration Using Active Transfer Learning and Data Augmentation,” *npj Comput. Mater.*, **7**(1), pp. 1–7.
- [55] Jasil, S. P. G., and Ulagamuthalvi, V., 2021, “Deep Learning Architecture Using Transfer Learning for Classification of Skin Lesions,” *J. Ambient Intell. Humaniz. Comput.*

- [56] Jia Deng, Wei Dong, Socher, R., Li-Jia Li, Kai Li, and Li Fei-Fei, 2009, “ImageNet: A Large-Scale Hierarchical Image Database,” *ieeexplore.ieee.org*, pp. 248–255.
- [57] Russakovsky, O., Deng, J., Su, H., Krause, J., Satheesh, S., Ma, S., Huang, Z., Karpathy, A., Khosla, A., Bernstein, M., Berg, A. C., and Fei-Fei, L., 2015, “ImageNet Large Scale Visual Recognition Challenge,” *Int. J. Comput. Vis.*, **115**(3), pp. 211–252.
- [58] Simonyan, K., and Zisserman, A., 2015, “Very Deep Convolutional Networks for Large-Scale Image Recognition,” *3rd Int. Conf. Learn. Represent. ICLR 2015 - Conf. Track Proc.*
- [59] Szegedy, C., Vanhoucke, V., Ioffe, S., Shlens, J., and Wojna, Z., 2016, “Rethinking the Inception Architecture for Computer Vision,” *Proc. IEEE Comput. Soc. Conf. Comput. Vis. Pattern Recognit.*, **2016-Decem**, pp. 2818–2826.
- [60] Chollet, F., 2017, “Xception: Deep Learning with Depthwise Separable Convolutions,” *Proc. - 30th IEEE Conf. Comput. Vis. Pattern Recognition, CVPR 2017*, **2017-Janua**, pp. 1800–1807.
- [61] Wang, H., Emmerich, M., Van Stein, B., and Bäck, T., 2017, “A New Acquisition Function for Bayesian Optimization Based on the Moment-Generating Function,” *2017 IEEE Int. Conf. Syst. Man, Cybern. SMC 2017*, **2017-Janua**, pp. 507–512.
- [62] Yu, S., Wang, C., Zhang, Y., Dong, B., Jiang, Z., Chen, X., Chen, W., and Sun, C., 2017, “Design of Non-Deterministic Quasi-Random Nanophotonic Structures Using Fourier Space Representations,” *Sci. Rep.*, **7**(1), pp. 1–10.

- [63] Ghumman, U. F., van Beek, A., Munshi, J., Chien, T. Y., Balasubramanian, G., and Chen, W., 2021, "SDF-Based Inverse Process Design of Solar Cells Using Molecular Dynamics Simulations," Proc. ASME Des. Eng. Tech. Conf., **3B-2021**.
- [64] Tao, S., Van Beek, A., Apley, D. W., and Chen, W., 2021, "Multi-Model Bayesian Optimization for Simulation-Based Design," J. Mech. Des. Trans. ASME, **143**(11).
- [65] Huang, D., Allen, T. T., Notz, W. I., and Zeng, N., 2006, "Global Optimization of Stochastic Black-Box Systems via Sequential Kriging Meta-Models," J. Glob. Optim., **34**(3), pp. 441–466.
- [66] Olsson, A., Sandberg, G., and Dahlblom, O., 2003, "On Latin Hypercube Sampling for Structural Reliability Analysis," Struct. Saf., **25**(1), pp. 47–68.
- [67] Munshi, J., Chen, W., Chien, T. Y., and Balasubramanian, G., 2021, "Machine Learned Metaheuristic Optimization of the Bulk Heterojunction Morphology in P3HT:PCBM Thin Films," Comput. Mater. Sci., **187**, p. 110119.
- [68] Munshi, J., Chien, T. Y., Chen, W., and Balasubramanian, G., 2020, "Elasto-Morphology of P3HT:PCBM Bulk Heterojunction Organic Solar Cells," Soft Matter, **16**(29), pp. 6743–6751.
- [69] Hansoge, N. K., Huang, T., Sinko, R., Xia, W., Chen, W., and Keten, S., 2018, "Materials by Design for Stiff and Tough Hairy Nanoparticle Assemblies," ACS Nano, **12**(8), pp. 7946–7958.
- [70] Humphrey, W., Dalke, A., and Schulten, K., 1996, "VMD: Visual Molecular Dynamics,"

- J. Mol. Graph., **14**(1), pp. 33–38.
- [71] Vögele, M., Holm, C., and Smiatek, J., 2015, “Coarse-Grained Simulations of Polyelectrolyte Complexes: MARTINI Models for Poly(Styrene Sulfonate) and Poly(Diallyldimethylammonium),” J. Chem. Phys., **143**(24), p. 243151.
- [72] Munshi, J., Farooq Ghumman, U., Iyer, A., Dulal, R., Chen, W., Chien, T. Y., and Balasubramanian, G., 2018, “Composition and Processing Dependent Miscibility of P3HT and PCBM in Organic Solar Cells by Coarse-Grained Molecular Simulations,” Comput. Mater. Sci., **155**, pp. 112–115.
- [73] Munshi, J., Dulal, R., Chien, T., Chen, W., and Balasubramanian, G., 2019, “Solution Processing Dependent Bulk Heterojunction Nanomorphology of P3HT/PCBM Thin Films,” ACS Appl. Mater. Interfaces, **11**(18), pp. 17056–17067.
- [74] Reyes-Reyes, M., Kim, K., and Carroll, D. L., 2005, “High-Efficiency Photovoltaic Devices Based on Annealed Poly(3-Hexylthiophene) and 1-(3-Methoxycarbonyl)-Propyl-1-Phenyl-(6,6) C61 Blends,” Appl. Phys. Lett., **87**(8), p. 083506.
- [75] Li, G., Shrotriya, V., Huang, J., Yao, Y., Moriarty, T., Emery, K., and Yang, Y., 2010, “High-Efficiency Solution Processable Polymer Photovoltaic Cells by Self-Organization of Polymer Blends,” *Materials for Sustainable Energy: A Collection of Peer-Reviewed Research and Review Articles from Nature Publishing Group*, World Scientific Publishing Co., pp. 80–84.
- [76] Kadem, B., Hassan, A., and Cranton, W., 2016, “Efficient P3HT:PCBM Bulk Heterojunction Organic Solar Cells; Effect of Post Deposition Thermal Treatment,” J.

- Mater. Sci. Mater. Electron., **27**(7), pp. 7038–7048.
- [77] Boettinger, W. J., Warren, J. A., Beckermann, C., and Karma, A., 2002, “Phase-Field Simulation of Solidification,” *Annu. Rev. Mater. Res.*, **32**(1), pp. 163–194.
- [78] Chadwick, A. F., and Voorhees, P. W., 2021, “The Development of Grain Structure during Additive Manufacturing,” *Acta Mater.*, **211**, p. 116862.
- [79] Shi, Y., Zhang, Y., Xu, Q., Liu, B., Cui, H., and Mi, G., 2012, “Modeling and Simulation of Dendrite Growth in Solidification of Al-Si-Mg Ternary Alloys,” *IOP Conf. Ser. Mater. Sci. Eng.*, **33**(1).
- [80] Lian, Y., Lin, S., Yan, W., Liu, W. K., and Wagner, G. J., 2018, “A Parallelized Three-Dimensional Cellular Automaton Model for Grain Growth during Additive Manufacturing,” *Comput. Mech.*, **61**(5), pp. 543–558.
- [81] Rappaz, M., and Gandin, C. A., 1993, “Probabilistic Modelling of Microstructure Formation in Solidification Processes,” *Acta Metall. Mater.*, **41**(2), pp. 345–360.
- [82] Tonks, M. R., and Aagesen, L. K., 2019, “The Phase Field Method: Mesoscale Simulation Aiding Material Discovery,” *Annu. Rev. Mater. Res.*, **49**(1).
- [83] Rodgers, T. M., Bishop, J. E., and Madison, J. D., 2018, “Direct Numerical Simulation of Mechanical Response in Synthetic Additively Manufactured Microstructures,” *Model. Simul. Mater. Sci. Eng.*, **26**(5).
- [84] Fullwood, D. T., Niezgoda, S. R., Adams, B. L., and Kalidindi, S. R., 2010, “Microstructure Sensitive Design for Performance Optimization,” *Prog. Mater. Sci.*,

- 55(6), pp. 477–562.
- [85] Roberts, A. P., and Torquato, S., 1999, “Chord-Distribution Functions of Three-Dimensional Random Media: Approximate First-Passage Times of Gaussian Processes,” *Phys. Rev. E - Stat. Physics, Plasmas, Fluids, Relat. Interdiscip. Top.*, **59**(5), pp. 4953–4963.
- [86] Talukdar, M. S., Torsaeter, O., Ioannidis, M. A., and Howard, J. J., 2002, “Stochastic Reconstruction of Chalk from 2D Images,” *Transp. Porous Media*, **48**(1), pp. 101–123.
- [87] Yan, W., Lin, S., Kafka, O. L., Lian, Y., Yu, C., Liu, Z., Yan, J., Wolff, S., Wu, H., Ndip-Agbor, E., Mozaffar, M., Ehmann, K., Cao, J., Wagner, G. J., and Liu, W. K., 2018, “Data-Driven Multi-Scale Multi-Physics Models to Derive Process–Structure–Property Relationships for Additive Manufacturing,” *Comput. Mech.*, **61**(5), pp. 521–541.
- [88] Sinclair, K., 2002, *Linear Algebra Guide*.
- [89] Mallows, C. L., and Kullback, S., 1959, *Information Theory and Statistics.*, Courier Corporation.
- [90] Yu, Z., and Herman, G., 2005, *On the Earth Mover’s Distance as a Histogram Similarity Metric for Image Retrieval*.
- [91] Sharma, G., Abbas, S. H., and Gupta, V. K., “Solving Multi-Objective Transportation Problem to Reduce Transportation Cost and Time,” *J. J. Adv. Math.*, **11**(1).
- [92] Yu, C., Kafka, O. L., and Liu, W. K., 2019, “Self-Consistent Clustering Analysis for Multiscale Modeling at Finite Strains,” *Comput. Methods Appl. Mech. Eng.*, **349**, pp.

339–359.

- [93] Lian, Y., Gan, Z., Yu, C., Kats, D., Liu, W. K., and Wagner, G. J., 2019, “A Cellular Automaton Finite Volume Method for Microstructure Evolution during Additive Manufacturing,” *Mater. Des.*, **169**, p. 107672.
- [94] Ennings, B. R. J., Arslow, K. P., Thomson, J. J., and Ottewill, R. H., 1988, “Particle Size Measurement: The Equivalent Spherical Diameter,” *Proc. R. Soc. London. A. Math. Phys. Sci.*, **419**(1856), pp. 137–149.
- [95] Hovington, P., Pinard, P. T., Lagacé, M., Rodrigue, L., Gauvin, R., and Trudeau, M. L., 2009, “Towards a More Comprehensive Microstructural Analysis of Zr-2.5Nb Pressure Tubing Using Image Analysis and Electron Backscattered Diffraction (EBSD),” *J. Nucl. Mater.*, **393**(1), pp. 162–174.
- [96] Latypov, M. I., Kühbach, M., Beyerlein, I. J., Stinville, J. C., Toth, L. S., Pollock, T. M., and Kalidindi, S. R., 2018, “Application of Chord Length Distributions and Principal Component Analysis for Quantification and Representation of Diverse Polycrystalline Microstructures,” *Mater. Charact.*, **145**, pp. 671–685.
- [97] Sastry, K., Goldberg, D., and Kendall, G., 2005, “Genetic Algorithms,” *Search Methodol. Introd. Tutorials Optim. Decis. Support Tech.*, pp. 97–125.
- [98] Pelikan, M., Goldberg, D., and Cantu-Paz, E., 1999, “BOA: The Bayesian Optimization Algorithm,” *Proc. Genet. Evol. Comput. Conf. GECCO-99*, **1**.
- [99] Kennedy, M. C., and O’Hagan, A., 2001, “Bayesian Calibration of Computer Models,” *J.*

- R. Stat. Soc. Ser. B Stat. Methodol., **63**(3), pp. 425–464.
- [100] Tapia, G., Johnson, L., Franco, B., Karayagiz, K., Ma, J., Arroyave, R., Karaman, I., and Elwany, A., 2017, “Bayesian Calibration and Uncertainty Quantification for a Physics-Based Precipitation Model of Nickel-Titanium Shape-Memory Alloys,” *J. Manuf. Sci. Eng. Trans. ASME*, **139**(7).
- [101] Kuhn, J., Spitz, J., Sonnweber-Ribic, P., Schneider, M., and Böhlke, T., 2021, *Identifying Material Parameters in Crystal Plasticity by Bayesian Optimization*, Springer US.
- [102] Perdikaris, P., and Karniadakis, G. E., 2016, “Model Inversion via Multi-Fidelity Bayesian Optimization: A New Paradigm for Parameter Estimation in Haemodynamics, and Beyond,” *J. R. Soc. Interface*, **13**(118).
- [103] Stoudt, M. R., Williams, M. E., Levine, L. E., Creuziger, A., Young, S. A., Heigel, J. C., Lane, B. M., and Phan, T. Q., 2020, “Location-Specific Microstructure Characterization Within IN625 Additive Manufacturing Benchmark Test Artifacts,” *Integr. Mater. Manuf. Innov.*, **9**(1), pp. 54–69.
- [104] Gan, Z., Lian, Y., Lin, S. E., Jones, K. K., Liu, W. K., and Wagner, G. J., 2019, “Benchmark Study of Thermal Behavior, Surface Topography, and Dendritic Microstructure in Selective Laser Melting of Inconel 625,” *Integr. Mater. Manuf. Innov.*, **8**(2), pp. 178–193.
- [105] Rai, A., Markl, M., and Körner, C., 2016, “A Coupled Cellular Automaton–Lattice Boltzmann Model for Grain Structure Simulation during Additive Manufacturing,” *Comput. Mater. Sci.*, **124**, pp. 37–48.

- [106] Amir Reza Ansari Dezfoli, Y.-L. L. and M. M. R., 2021, “Microstructure and Elements Concentration of Inconel 713LC,” crystals, **11**(1065).
- [107] Rolchigo, M., Stump, B., Belak, J., and Plotkowski, A., 2020, “Sparse Thermal Data for Cellular Automata Modeling of Grain Structure in Additive Manufacturing,” Model. Simul. Mater. Sci. Eng., **28**(6).
- [108] Yeh, C. J., Dowland, M., Schmidt, R. G., and Shull, K. R., 2016, “Fracture and Thermal Aging of Resin-Filled Silicone Elastomers,” J. Polym. Sci. Part B Polym. Phys., **54**(2), pp. 263–273.
- [109] Silvaroli, A. J., Heyl, T. R., Qiang, Z., Beebe, J. M., Ahn, D., Mangold, S., Shull, K. R., and Wang, M., 2020, “Tough, Transparent, Photocurable Hybrid Elastomers,” ACS Appl. Mater. Interfaces, **12**(39), pp. 44125–44136.
- [110] Liou, H. C., Sabba, F., Wang, Z., Wells, G., and Balogun, O., 2021, “Layered Viscoelastic Properties of Granular Biofilms,” Water Res., **202**, p. 117394.
- [111] Mars, W. V., and Fatemi, A., 2003, “Fatigue Crack Nucleation and Growth in Filled Natural Rubber,” Fatigue Fract. Eng. Mater. Struct., **26**(9), pp. 779–789.
- [112] Toki, S., Sics, I., Ran, S., Liu, L., Hsiao, B. S., Murakami, S., Senoo, K., and Kohjiya, S., 2002, “New Insights into Structural Development in Natural Rubber during Uniaxial Deformation by in Situ Synchrotron X-Ray Diffraction,” Macromolecules, **35**(17), pp. 6578–6584.
- [113] Griffiths, A. A., 1995, “The Phenomena of Rupture and Flow in Solids,” Masinovedenie,

- 4(1), pp. 9–14.
- [114] Soft Ternary -Semirings-I Ravi Kumar, O. B., Sankara Rao, B., Madhusudhana Rao, D., and -, al, 2016, “Fracture and Adhesion of Soft Materials: A Review,” [iopscience.iop.org](http://iopscience.iop.org).
- [115] Gent, A. N., and Pulford, C. T. R., 1984, “Micromechanics of Fracture in Elastomers,” *J. Mater. Sci.*, **19**(11), pp. 3612–3619.
- [116] Greensmith, H. W., and Thomas, A. G., 1955, “Rupture of Rubber. III. Determination of Tear Properties,” *J. Polym. Sci.*, **18**(88), pp. 189–200.
- [117] Tanaka, Y., Fukao, K., ... Y. M.-E. (Europhysics, and 1998, undefined, 1998, “Discontinuous Crack Fronts of Three-Dimensional Fractures,” [iopscience.iop.org](http://iopscience.iop.org), **43**(6), pp. 664–670.
- [118] Seitz, M., Martina, D., Baumberger, T., Matter, V. K.-S., and 2009, undefined, “Fracture and Large Strain Behavior of Self-Assembled Triblock Copolymer Gels,” [pubs.rsc.org](http://pubs.rsc.org).
- [119] Fukahori, Y., and Andrews, E. H., 1978, “Fracture Surface Roughness in Highly Deformable Polymers,” *J. Mater. Sci.*, **13**(4), pp. 777–785.
- [120] Baumberger, T., Caroli, C., Martina, D., letters, O. R.-P. review, and 2008, undefined, 2008, “Magic Angles and Cross-Hatching Instability in Hydrogel Fracture,” *APS*, **100**(17).
- [121] Baumberger, T., Caroli, C., Martina, D., and Ronsin, O., 2008, “Magic Angles and Cross-Hatching Instability in Hydrogel Fracture,” *Phys. Rev. Lett.*, **100**(17), p. 178303.
- [122] Ronsin, O., Caroli, C., Letters), T. B.-E. (Europhysics, and 2014, undefined, “Crack Front

- Echelon Instability in Mixed Mode Fracture of a Strongly Nonlinear Elastic Solid,”  
iopscience.iop.org.
- [123] Kolvin, I., Cohen, G., materials, J. F.-N., and 2018, undefined, “Topological Defects Govern Crack Front Motion and Facet Formation on Broken Surfaces,” nature.com.
- [124] Leblond, J., Karma, A., ... L. P.-J. of the M., and 2019, undefined, “Configurational Stability of a Crack Propagating in a Material with Mode-Dependent Fracture Energy-Part I: Mixed-Mode I+ III,” Elsevier.
- [125] Chen, Q., Xu, S., Lu, M., Liu, J., and Shull, K. R., 2021, “Temperature-Dependent Viscoelastic Energy Dissipation and Fatigue Crack Growth in Filled Silicone Elastomers,” ACS Appl. Polym. Mater., **3**(12), pp. 6207–6217.
- [126] Gong, Y., Misture, S. T., Gao, P., and Mellott, N. P., 2016, “Surface Roughness Measurements Using Power Spectrum Density Analysis with Enhanced Spatial Correlation Length,” J. Phys. Chem. C, **120**(39), pp. 22358–22364.
- [127] Jacobs, T. D. B., Junge, T., and Pastewka, L., 2017, “Quantitative Characterization of Surface Topography Using Spectral Analysis,” Surf. Topogr. Metrol. Prop., **5**(1), p. 013001.
- [128] Calandri, M., Yin, S., Aldwell, B., Calignano, F., Lupoi, R., and Ugués, D., “Texture and Microstructural Features at Different Length Scales in Inconel 718 Produced by Selective Laser Melting,” mdpi.com.
- [129] Jandejsek, I., Gajdoš, L., Šperl, M., and Vavřík, D., 2017, “Analysis of Standard Fracture

- Toughness Test Based on Digital Image Correlation Data,” *Eng. Fract. Mech.*, **182**, pp. 607–620.
- [130] Zhang, R., Mohammed, I. K., Taylor, A. C., and Charalambides, M. N., 2022, “A Microstructure Image-Based Numerical Model for Predicting the Fracture Toughness of Alumina Trihydrate (ATH) Filled Poly(Methyl Methacrylate) (PMMA) Composites,” *Compos. Part B Eng.*, **232**, p. 109632.
- [131] Zhao, S., Liu, Z., Lin, J., ... J. Z.-A. in N., and 2020, undefined, “Differentiable Augmentation for Data-Efficient Gan Training,” *proceedings.neurips.cc*.
- [132] Bostanabad, R., 2020, “Reconstruction of 3D Microstructures from 2D Images via Transfer Learning,” *CAD Comput. Aided Des.*, **128**.
- [133] on, F. C.-P. of the I. conference, and 2017, undefined, “Xception: Deep Learning with Depthwise Separable Convolutions,” *openaccess.thecvf.com*.
- [134] Źarski, M., Wójcik, B., Książek, K., and Mischczak, J. A., 2021, “Finicky Transfer Learning-A Method of Pruning Convolutional Neural Networks for Cracks Classification on Edge Devices.”
- [135] Liu, B., Cai, Y., Guo, Y., and Chen, X., 2021, “TransTailor: Pruning the Pre-Trained Model for Improved Transfer Learning,” *35th AAAI Conference on Artificial Intelligence, AAAI 2021, AAAI*, pp. 8627–8634.
- [136] Gordon, M. A., Duh, K., and Andrews, N., 2020, “Compressing BERT: Studying the Effects of Weight Pruning on Transfer Learning,” pp. 143–155.

- [137] Gulli, A., and Pal, S., 2017, “Deep Learning with Keras,” p. 318.
- [138] Pommet, D. A., Grann, E. B., Moharam, M. G., and Gaylord, T. K., 1995, “Stable Implementation of the Rigorous Coupled-Wave Analysis for Surface-Relief Gratings: Enhanced Transmittance Matrix Approach,” *JOSA A*, Vol. 12, Issue 5, pp. 1077-1086, **12**(5), pp. 1077–1086.
- [139] Ieracitano, C., Mammone, N., Bramanti, A., Hussain, A., and Morabito, F. C., 2019, “A Convolutional Neural Network Approach for Classification of Dementia Stages Based on 2D-Spectral Representation of EEG Recordings,” *Neurocomputing*, **323**, pp. 96–107.
- [140] Epley, C. C., Love, M. D., and Morris, A. J., 2017, “Characterizing Defects in a UiO-AZB Metal–Organic Framework.”
- [141] Elhajjar, R. F., Shams, S. S., Kemeny, G. J., and Stuessy, G., 2016, “A Hybrid Numerical and Imaging Approach for Characterizing Defects in Composite Structures,” *Compos. Part A Appl. Sci. Manuf.*, **81**, pp. 98–104.
- [142] Chollet, F., 2017, “Xception: Deep Learning with Depthwise Separable Convolutions,” *Proc. - 30th IEEE Conf. Comput. Vis. Pattern Recognition, CVPR 2017*, **2017-Janua**, pp. 1800–1807.
- [143] Feurer, M., Klein, A., Jost, K. E., Springenberg, T., Blum, M., and Hutter, F., “Efficient and Robust Automated Machine Learning,” *proceedings.neurips.cc*.
- [144] Kim, C., Chandrasekaran, A., Huan, T. D., Das, D., and Ramprasad, R., 2018, “Polymer Genome: A Data-Powered Polymer Informatics Platform for Property Predictions,” *J.*

- Phys. Chem. C, **122**(31), pp. 17575–17585.
- [145] Kirklin, S., Saal, J. E., Meredig, B., Thompson, A., Doak, J. W., Aykol, M., Rühl, S., and Wolverton, C., 2015, “The Open Quantum Materials Database (OQMD): Assessing the Accuracy of DFT Formation Energies,” *npj Comput. Mater.*, **1**(1), pp. 1–15.
- [146] Jain, A., Ong, S. P., Hautier, G., Chen, W., Richards, W. D., Dacek, S., Cholia, S., Gunter, D., Skinner, D., Ceder, G., and Persson, K. A., 2013, “Commentary: The Materials Project: A Materials Genome Approach to Accelerating Materials Innovation,” *APL Mater.*, **1**(1), p. 011002.
- [147] Campbell, C. E., Kattner, U. R., and Liu, Z. K., 2014, “The Development of Phase-Based Property Data Using the CALPHAD Method and Infrastructure Needs,” *Integr. Mater. Manuf. Innov.*, **3**(1), pp. 158–180.
- [148] Zhao, H., Li, X., Zhang, Y., Schadler, L. S., Chen, W., and Brinson, L. C., 2016, “Perspective: NanoMine: A Material Genome Approach for Polymer Nanocomposites Analysis and Design,” *APL Mater.*, **4**(5), p. 053204.
- [149] Otsu, and N., 1996, *A Threshold Selection Method from Gray-Level Histograms*.
- [150] Niblack, W., 1986, “An Introduction to Digital Image Processing,” *An Introd. to Digit. image Process.*
- [151] Xu, H., Li, Y., Brinson, C., and Chen, W., 2014, “A Descriptor-Based Design Methodology for Developing Heterogeneous Microstructural Materials System,” *J. Mech. Des. Trans. ASME*, **136**(5).

- [152] Moliton, A., and Nunzi, J. M., 2006, "How to Model the Behaviour of Organic Photovoltaic Cells," *Polym. Int.*, **55**(6), pp. 583–600.
- [153] Pandey, R., and Holmes, R. J., 2010, "Graded Donor-Acceptor Heterojunctions for Efficient Organic Photovoltaic Cells," *Adv. Mater.*, **22**(46), pp. 5301–5305.
- [154] Garner, L. E., Bera, A., Larson, B. W., Ostrowski, D. P., Pal, A. J., and Braunecker, W. A., 2017, "Promoting Morphology with a Favorable Density of States Using Diiodooctane to Improve Organic Photovoltaic Device Efficiency and Charge Carrier Lifetimes," *ACS Energy Lett.*, **2**(7), pp. 1556–1563.
- [155] Baniassadi, M., Garmestani, H., Li, D. S., Ahzi, S., Khaleel, M., and Sun, X., 2011, "Three-Phase Solid Oxide Fuel Cell Anode Microstructure Realization Using Two-Point Correlation Functions," *Acta Mater.*, **59**(1), pp. 30–43.
- [156] Fullwood, D. T., Kalidindi, S. R., Niezgod, S. R., Fast, A., and Hampson, N., 2008, "Gradient-Based Microstructure Reconstructions from Distributions Using Fast Fourier Transforms," *Mater. Sci. Eng. A*, **494**(1–2), pp. 68–72.